Universität Bremen

ALFRED-WEGENER-INSTITUT
HELMHOLTZ-ZENTRUM FÜR POLAR- UND MEERESFORSCHUNG

The role of sea ice in the surface freshwater flux of the southern Weddell Sea: Insights from sea ice–ice shelf–ocean model simulations

Dissertation submitted by

Lukrecia Štulić

in fulfilment of the requirements
for the degree of

Doctor of Natural Sciences (Dr. rer. nat.)

to

Faculty 1

Physics and Electrical Engineering

University of Bremen

2024

First reviewer:	Prof. Dr. Torsten Kanzow Alfred Wegener Institute Helmholtz Centre for Polar and Marine Research and University of Bremen
Second reviewer:	Prof. Dr. Christian Haas Alfred Wegener Institute Helmholtz Centre for Polar and Marine Research and University of Bremen
Doctoral colloquium:	October 15, 2024

Sun and water are questions endlessly worth answering.

Richard Powers, The Overstory

Abstract

Sea ice production dominates surface salt forcing in the southern Weddell Sea. The strongest sea ice growth rates are found in coastal polynyas, where steady offshore winds promote divergent ice movement during the freezing season. The strong sea ice production rates on the continental shelf lead to the densification of the near-surface waters, resulting in the formation of High Salinity Shelf Water (HSSW) that feeds the global overturning circulation and fuels the basal melt of vast Filchner-Ronne Ice Shelf (FRIS). In this thesis, I use the Finite Element Sea ice–ice shelf–Ocean Model (FESOM) forced by output from the regional atmospheric model COSMO-CLM (CCLM) with 14 km horizontal resolution to investigate the role of sea ice for the surface freshwater flux of the southern Weddell Sea (2002–2017), with a particular focus on coastal polynyas. The presence of stationary icescape features (i.e. fast-ice areas and grounded icebergs) can influence the formation of polynyas and, therefore, impact sea ice production. The representation of the icescape in the model is included by prescribing the position, shape, and temporal evolution of a largely immobile ice mélange that was forming between FRIS and the grounded iceberg A23-A based on satellite data. The results show that 70% of the ice produced on the continental shelf of the southern Weddell Sea is exported from the region. While coastal polynyas cover 2% of the continental shelf area, sea ice production within the coastal polynyas accounts for 17% of the overall annual sea ice production (1509 km^3). The largest contributions come from the Ronne Ice Shelf and Brunt Ice Shelf polynyas, and polynyas associated with the ice mélange. I investigate the sensitivity of the polynya-based ice production to the regional atmospheric forcing and representation of the icescape. Although large-scale atmospheric fields determine the sea ice production outside polynyas, both the regional

atmospheric forcing and the treatment of the icescape are important for the regional patterns of sea ice production in polynyas. Compared to using ERA-Interim reanalysis as an atmospheric forcing dataset, using CCLM output reduces polynya-based ice production over the eastern continental shelf due to weaker offshore winds, bringing results for those regions closer to the satellite-based estimates. The representation of the ice mélange is crucial for the simulation of polynyas westward/eastward of it, which are otherwise suppressed/overestimated. Furthermore, the improved fast ice representation and the optimization of sea ice parameters using Green's function approach reduce sea ice production in major polynyas, yielding a more realistic distribution of ice production within polynyas. The results of this thesis show that the location, rather than just the strength of the sea ice production in polynyas, is an important factor in determining the properties of the HSSW produced on the continental shelf, affecting in turn the basal melting of the Filchner-Ronne Ice Shelf.

Contents

1. Introduction

Antarctica's icescape encompasses a variety of dynamic and variable ice forms including land ice sheets, ice shelves, and sea ice. Sea ice, the frozen sea water encircling the continent, responds the fastest to the surface atmospheric forcing. It typically covers up to 60% of the Southern Ocean in winter, and in summer less than 10%. Sea ice plays a key role in the climate of Antarctica regulating the atmosphere-ocean energy and freshwater fluxes exchange (Dieckmann & Hellmer 2003). Satellites measured the lowest Antarctic sea ice extent (area with sea ice concentration >15%) on record in February 2023 (Fig. 1.1), followed by an exceptionally low autumn and winter sea ice advance (Purich & Doddridge 2023, Gilbert & Holmes 2024), possibly indicating a shift to the new sea ice state with less ice. The observed levels of sea ice extent anomalies are extremely unlikely to be simulated in the latest generation of climate models without accounting for effects of climate change (Diamond et al. 2024).

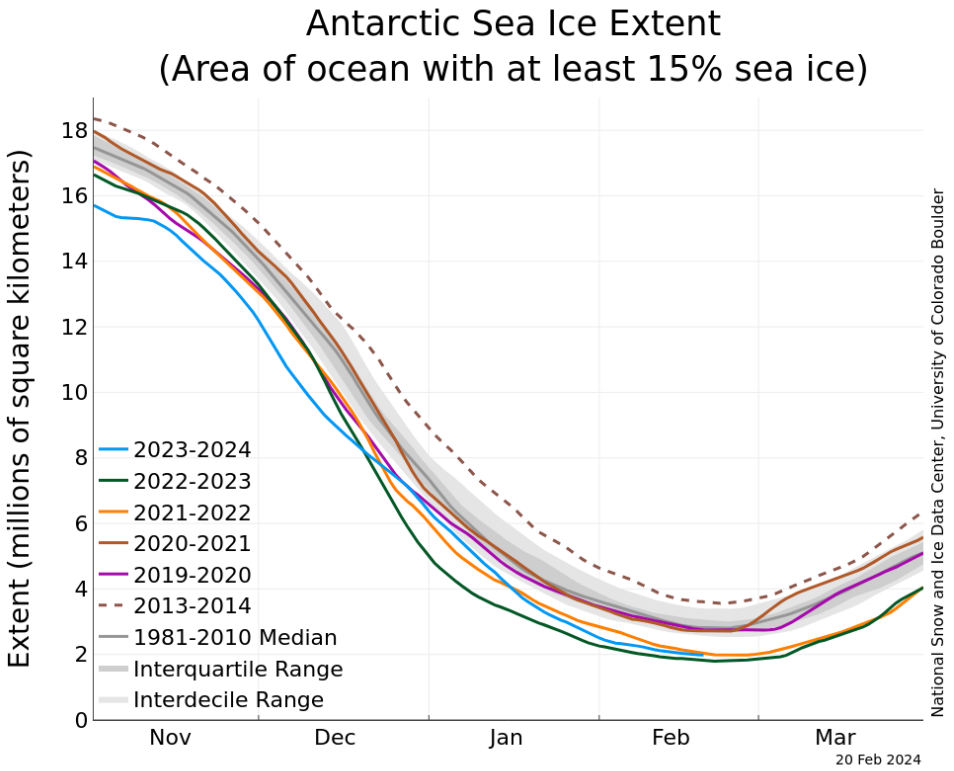

Figure 1.1: Antarctic sea ice extent as of February 20, 2024 along with daily ice extent data for four previous years and the record high year. 2023 to 2024 is shown in blue, 2022 to 2023 in green, 2021 to 2022 in orange, 2020 to 2021 in brown, 2019 to 2020 in magenta, and 2013 to 2014 in dashed brown. The 1981 to 2010 median is in dark gray. The gray areas around the median line show the interquartile and interdecile ranges of the data. This figure and the associated caption were taken from: Sea Ice Index data, National Snow and Ice Data Center (`https://nsidc.org/arcticseaicenews/2024/02/`, last access May 24, 2024)

The floating ice shelves have been protecting the Antarctic Ice Sheet, the largest freshwater reservoir on Earth, from releasing its contents into the ocean. Ice shelves in Antarctica are loosing mass rapidly over the last decades (Fig. 1.2) (Paolo et al. 2015) leading to a sea level rise of 14 mm since 1979 (Rignot et al. 2019). The majority of the ice loss comes from the ocean-induced melting of ice sheets and glaciers under the influence of warm ocean waters (Rignot et al. 2019). On the "warm" continental shelves of, for example, the Amundsen and Bellingshausen Seas, the seafloor is flushed by the waters of open ocean origin exceeding 0°C (Thompson et al. 2018).

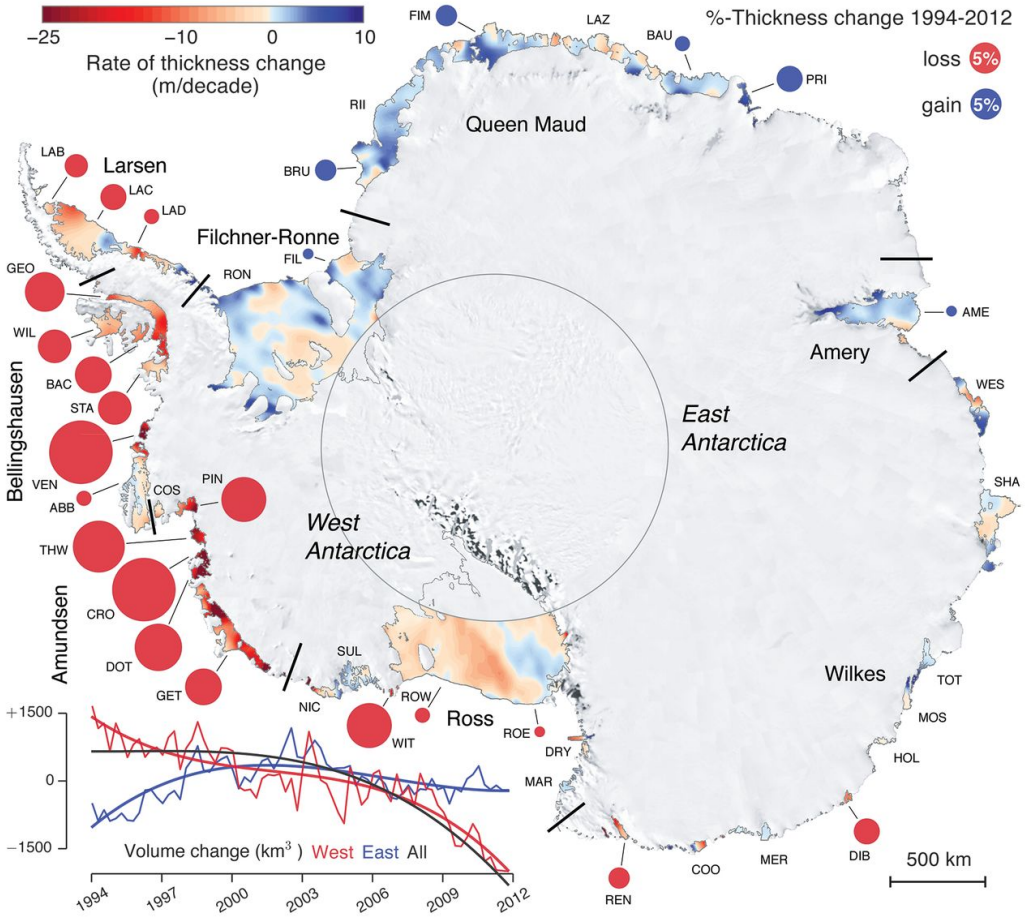

Figure 1.2: Figure and caption information are taken from Paolo et al. (2015) (their Fig.1). Eighteen years of change in thickness and volume of Antarctic ice shelves. Rates of thickness change (meters per decade) is color-coded from -25 (thinning) to +10 (thickening). Circles represent percentage of thickness lost (red) or gained (blue) in 18 years. Background is the Landsat Image Mosaic of Antarctica (LIMA).

Unlike the "warm" continental shelves, the "dense" continental shelf in the southern Weddell Sea is dominated by near-freezing ocean temperatures (Nicholls et al. 2009, Janout et al. 2021). Here, sea ice production dominates surface salt forcing (Timmermann et al. 2001, Haumann et al. 2016). Brine rejected in the process of sea ice production results in the production of High Salinity Shelf Water (HSSW; about -1.9 to -1.5 °C, S>34.6 psu) that feeds the global overturning circulation and fuels the basal melt of the adjacent Filchner-Ronne Ice Shelf (FRIS). However, because most of the water entering the FRIS cavity remains close to the freezing temperature, the melt rates of FRIS are currently moderate. (Rignot et al. 2019, Adusumilli et al. 2020).

The basal melt rates of FRIS might increase drastically under potential future climate shifts of the surface freshwater budget (Timmermann & Hellmer 2013, Naughten et al. 2021). Therefore, surface freshwater flux on the southern Weddell Sea continental shelf is not only an important driver of the lower branch of the global overturning circulation but also crucial for the stability of FRIS and, therefore, global sea level.

Due to the remoteness of the region and perennial ice cover, observations in the southern Weddell Sea are limited. Thus, modeling and remote sensing are necessary tools for investigating sea ice–ocean–ice shelf processes in the region. As will be detailed below, this thesis aims to solve some of the challenges in modeling the southern Weddell Sea surface freshwater flux so that it represents the key aspects of the observed system.

1.1 The southern Weddell Sea: sea ice and ocean circulation

The Weddell Sea contains the largest amount of Antarctic multiyear sea ice (Parkinson 2019, Turner et al. 2020). The monthly sea ice extent for the period investigated in this thesis (2002–2017) is shown in Fig. 1.3 c. Sea ice extent exhibits a prominent seasonal cycle and high interannual variability, making forecasting ice extent months in advance based on the current ice state difficult (Parkinson 2019). The ice extent reaches a minimum typically in February when ice is limited to the southwestern Weddell Sea (Fig. 1.3 a). A distinct pattern is visible in the mean (2002–2017) February ice concentration field, with low ice concentration to the west of the grounded iceberg A23-A and high ice concentration east of it (Fig. 1.3 a). The iceberg A23-A broke off from the Filchner Ice Shelf in 1986 and remained in the region until 2022 (iceberg locations from the Antarctic Iceberg Data (USNIC), `https://usicecenter.gov/Products/AntarcIcebergs`, last access August 15, 2023, and Antarctic Iceberg Tracking Database, `https://www.scp.byu.edu/data/iceberg/database1.html`, last access March 22, 2023, Budge & Long (2018)), blocking the prevailing westward ice drift. The higher ice concentration between the grounded iceberg and Berkner Island (Fig. 1.3 a) is indicative of the fast ice bridge formation.

At the maximum extent, typically in September, ice covers the whole Weddell Sea (Fig. 1.3 b). However, lower sea ice concentrations (<70%)

can be found along the Ronne and Brunt ice shelves, and in the region surrounding grounded iceberg A23-A. These are regions with the frequent development of coastal polynyas (Paul et al. 2015). While for 2002–2017 sea ice extent did not exhibit a significant trend, an increasing trend of 4×10^3 km^2 a^{-1} is reported based on a 40-year record (1979–2019) (Parkinson 2019). However, the low sea extent anomalies that have been persisting since summer 2017 indicate an unprecedented change in the state of the Weddell Sea sea ice (Parkinson 2019, Turner et al. 2020), likely as a result of multiple atmospheric and oceanic influences (Parkinson 2019).

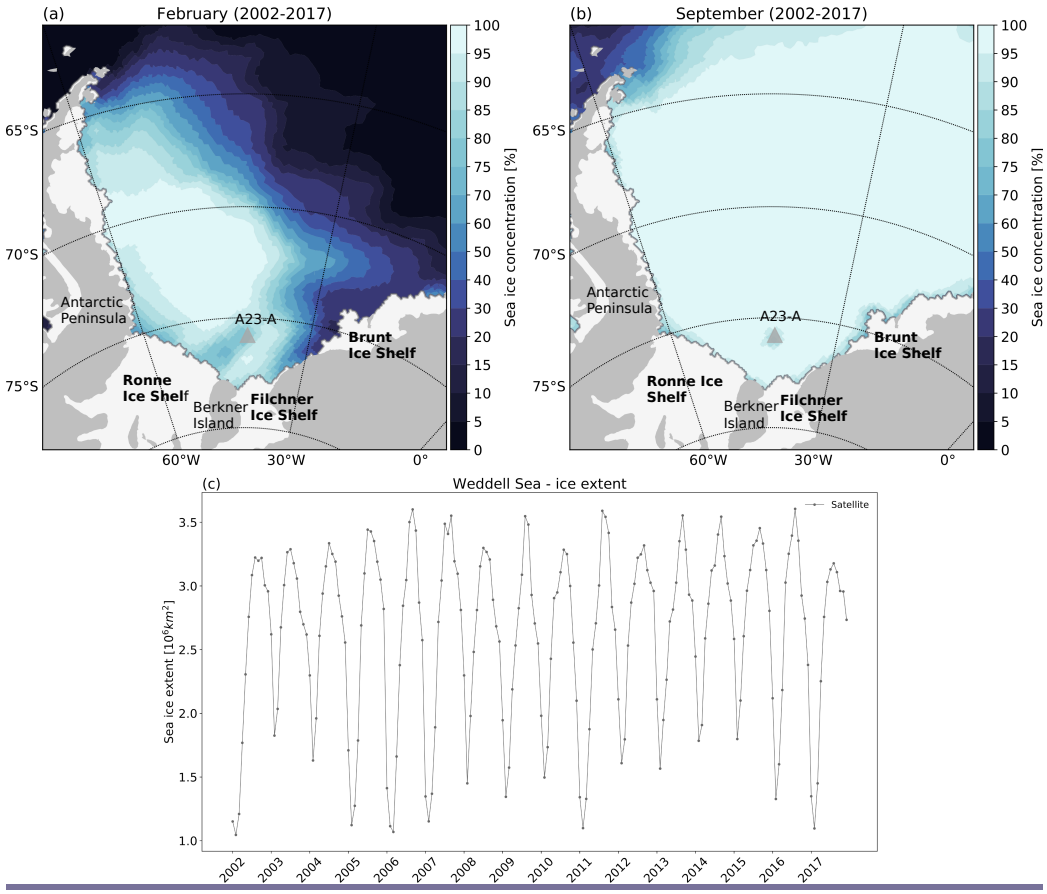

Figure 1.3: Mean (2002–2017) sea ice concentration for February (a) and September (b) over the Weddell Sea from satellite data (Peng et al. 2013). The solid gray line in all panels contours the ice shelf edge. The location of the grounded iceberg A23-A (2002–2017) is marked by a triangle. Note the higher ice concentration in (a) between Berkner Island and the grounded iceberg A23-A associated to the fast ice bridge. c) Time series of monthly sea ice extent (2002–2017) from satellite data (Peng et al. (2013), see Sect. 2.3.1).

While the north-western Weddell Sea is a region of net sea ice melt, the southern Weddell Sea is a region of net ice production (Timmermann et al.

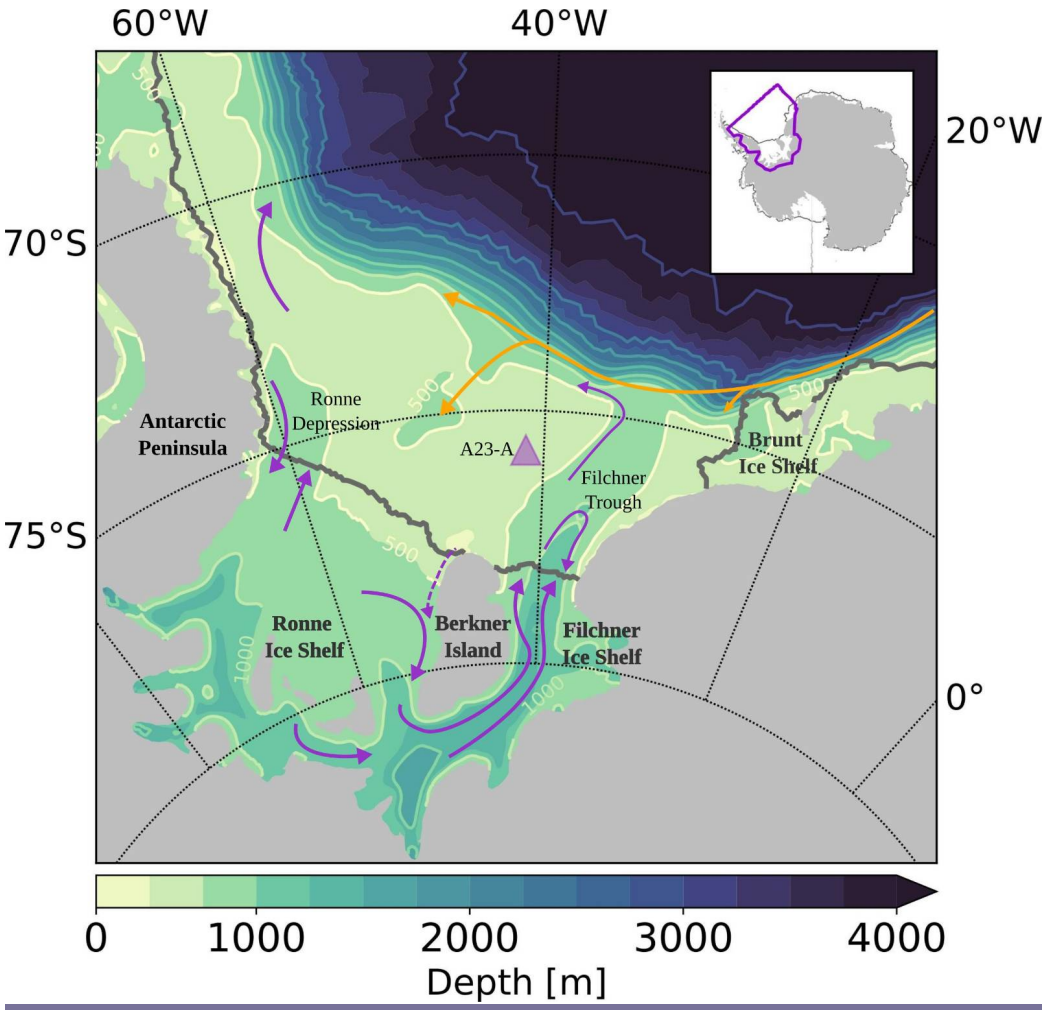

Figure 1.4: Map of the southern Weddell Sea. Bathymetry (Schaffer et al. 2016) is color shaded. The ice shelf edge is contoured in gray and the location of the grounded iceberg A23-A for 2002–2017 is marked by a triangle (data from the Antarctic Iceberg Tracking Database; https://www.scp.byu.edu/ data/iceberg/-database1.html, last access: 22 March 2023; (Budge & Long 2018). The main ocean circulation pathways after Janout et al. (2021) are indicated with arrows: the inflow of modified Warm Deep Water (orange) and High Salinity Shelf Water driven circulation (purple).

2001). The southern Weddell Sea continental shelf is dominated by HSSW formed as a result of sea ice production. Ice production is the strongest in coastal polynyas where steady offshore winds promote divergent ice movement during the freezing season (Haid et al. 2015). A portion of newly formed HSSW flows directly off the shelf and contributes to the formation of Weddell Sea Deep and Bottom Waters (Orsi et al. 1999), which are precursors of Antarctic Bottom Water (AABW) (Foster & Carmack 1976). Based on observations, Zhou et al. (2023) report 30% reduction in Weddell Sea Bot-

tom Water volume since 1992, probably linked to a multidecadal reduction in dense-water production in the continental shelf.

The sub-ice shelf circulation is driven by the density gradient between the denser water on the continental shelf and lighter water within the FRIS cavity (Nicholls & Østerhus 2004, Hattermann et al. 2021). HSSW produced off the Ronne Ice Shelf flows into the cavity mainly through the Ronne Depression (Fig. 1.4). Along the way through the cavity, HSSW melts the base of the ice shelf and entrains the meltwater. The end product of this process is the Ice Shelf Water (ISW), a colder and fresher watermass than HSSW, with temperatures below the surface freezing point. ISW exits the cavity through the Filchner Trough (Fig. 1.4) and may reach the continental shelf break and mix further with the warmer waters (Foldvik et al. 1985).

Based on the properties of the water masses in the Filchner cavity and at the Filchner Ice Shelf ice front, two modes have been observed. (Janout et al. 2021, Hattermann et al. 2021). In the Berkner mode, the local Berkner-HSSW dominates in the Filchner region and is able to enter the cavity through the northern part of the Filchner Ice Shelf front. In contrast, in the Ronne mode, Ronne-sourced ISW dominates conditions along the Filchner Ice Shelf front and in the Filchner Trough.

The intermediate layer of the Weddell Sea is dominated by Warm Deep Water which can mix with colder and fresher waters resulting in modified Warm Deep Water (mWDW, with typical temperatures of about -1 °C). The seasonal mWDW inflow towards the Filchner Trough (Fig. 1.4) is regulated by the Antarctic Slope Front (ASF) and exhibits high interannual variability (Ryan et al. 2020). However, mWDW has been observed reaching near the Filchner Ice Shelf (Darelius et al. 2016). Presently, the impact of mWDW on the southern Weddell Sea continental shelf is limited by the presence of dense waters in the Filchner Trough. Model studies suggest that freshening of the dense waters, due to changes in the future climate surface freshwater flux, could result in stronger mWDW inflow and, consequently, an increase in ice shelf melting (Hellmer et al. 2017, Naughten et al. 2021). The improved understanding of the processes linked to the changes in surface freshwater flux is, therefore, important for the robust future projections of the conditions on the southern Weddell Sea continental shelf.

1.1.1 The southern Weddell Sea surface freshwater flux

[1]

Sea ice production and melt drive the seasonal evolution of the surface freshwater flux in the southern Weddell Sea (Timmermann et al. 2001). When sea ice forms, salt is released, increasing the upper-ocean density and destabilizing the water column. Conversely, when sea ice melts, freshwater is released, increasing the near-surface stratification. Owing to the net export of sea ice from the southern Weddell Sea, the sea ice production on the continental shelf of the southern Weddell Sea exceeds the sea ice melt (Timmermann et al. 2001, Abernathey et al. 2016, Haumann et al. 2016). The strong sea ice production rates on the continental shelf lead to the densification of the near-surface waters, resulting in the formation of HSSW. The fraction of HSSW that flows into the ice-shelf cavity fuels the sub-ice shelf circulation of the vast Filchner-Ronne Ice Shelf (FRIS). Due to the decrease of the melting point of ice with depth, HSSW with temperatures close to the surface freezing point drives basal melting of the deepest parts of FRIS.

The highest sea ice production rates are maintained in coastal polynyas, areas of thin ice and low sea ice concentration. Driven by winds or ocean currents, coastal polynyas form along coastlines and ice fronts or in the lee of grounded icebergs and ice tongues (Massom et al. 1998, Maqueda et al. 2004, Nihashi & Ohshima 2015*a*). As a result of uncertainties in the observed sea ice thickness distribution and local heat fluxes, the contribution of coastal polynyas to the southern Weddell Sea freshwater budget is not well constrained (Haumann et al. 2016). However, coastal polynyas are broadly recognized as hot spots of HSSW formation. Although sea ice freshwater fluxes are found to be crucial for the water mass transformation on the southern Weddell Sea continental shelf (Abernathey et al. 2016, Pellichero et al. 2018), production rates of HSSW remain uncertain due to a lack of in-situ oceanic observations in polynyas and difficulties in representing the local sea ice–ice shelf–ocean interactions in numerical models.

Changes in large-scale atmospheric patterns can influence sea ice production in polynyas and affect interannual variability of the HSSW formation and sub-ice shelf circulation (Hattermann et al. 2021). Enhanced southerly

[1] This section is adapted from Stulic et al. (2023)

winds over the Ronne Ice Shelf, linked to displacement of the Amundsen Sea Low position, intensified sea ice formation in the Ronne polynya 2015–2018. This caused an intensification of the density-driven circulation under FRIS and a shift in the water mass properties in the Filchner cavity from the Berkner to the Ronne mode (Janout et al. 2021, Hattermann et al. 2021).

Sea ice production in the thin-ice areas (ice thickness 0–0.2 m) of coastal polynyas was estimated using heat flux calculations based on satellite microwave data (Tamura et al. 2008, Drucker et al. 2011, Nihashi & Ohshima 2015*a*) with spatial resolutions of 6.25–12.5 km. Higher-resolution data enables better discrimination between polynya areas and fast ice and reveals a more detailed spatial distribution of sea ice production, resulting in smaller sea-ice production estimates (Nihashi & Ohshima 2015*a*).

Another approach was taken by Paul et al. (2015), who employed thermal-infrared imagery from the Moderate-Resolution Imaging Spectroradiometer (MODIS) to calculate sea ice production. With a resolution of 2 km, even narrow polynyas along the southern Weddell Sea continental shelf were resolved on a daily basis for the winters 2002–2014, with the largest contributions to the polynya-based ice production being provided by the Ronne and Brunt Ice Shelf polynyas. Significant ice production was found in the polynyas developing in the lee of the ice bridge formed between the Filchner Ice Shelf and the grounded iceberg A23-A.

1.1.2 Modeling the southern Weddell Sea surface freshwater flux

As sea ice production estimates from satellite retrievals are limited to thin-ice areas in winter, numerical models that can simulate coastal polynya processes realistically are a valuable tool for investigating the role of polynyas in the surface freshwater flux of the southern Weddell Sea. High-resolution atmospheric forcing is needed to realistically simulate the effects of strong katabatic winds on the polynya development (Ebner et al. 2014), with consequences both for the dense water production (Mathiot et al. 2010, Haid et al. 2015) and basal melt (Dinniman et al. 2015). Nevertheless, only a few modeling studies focused on the southern Weddell Sea. Haid & Timmermann (2013) and Haid et al. (2015) investigated heat fluxes and sea ice production in the coastal polynyas of the southern Weddell Sea using a sea ice–ocean model. While the model represented well the major polynyas, a strong sensi-

tivity of the sea ice production and HSSW formation to atmospheric forcing was found.

Furthermore, these studies did not include the representation of the ice shelf, the influence of iceberg A23-A that was grounded in the region (Fig. 2.5), and the regular ice bridge formation between the Filchner Ice Shelf and the iceberg A23-A linked to high polynya occurrence (Paul et al. 2015). In a modeling study of the Filchner Ice Shelf system, Grosfeld et al. (2001) show that basal melt of the Filchner Ice Shelf decreases in the presence of grounded icebergs in front of it due to the weakened circulation within the ice shelf cavity. Studies in other regions have found that the representation of stationary features in the icescape (i.e., grounded icebergs, ice tongues, fast ice) can influence sea ice production and, consequently, ocean properties and basal melt. In a modeling study of the Amundsen continental shelf, Nakayama et al. (2014) found reduced sea ice export and sea ice formation in the Pine Island polynya in the presence of grounded icebergs west of it. Studies of the Mertz Glacier Tongue (MGT), East Antarctica, showed a drastic decrease in the sea ice production and dense water formation after a major calving event in 2010 (Kusahara et al. 2010, 2011), with consequences for the basal melt (Kusahara et al. 2017, Cougnon et al. 2017).

As mentioned above, the representation of regional offshore winds is essential for simulating sea ice production in polynyas on the southern Weddell Sea continental shelf. Additionally, research from other regions indicates that representing stationary sea ice features may be important for realistically simulating sea ice production and the ocean state. However, the quality of model simulations relative to the observed state also stems from the uncertainties inherent to the model parameterizations. Several studies have pointed that calibration of a small number of model parameters can lead to improved sea ice-ocean model estimates (e.g. Miller et al. (2006), Menemenlis et al. (2005), Nguyen et al. (2011)). Considering all these factors could lead to more realistic simulations of the surface freshwater flux in the southern Weddell Sea and improve our understanding of sea ice–ocean–ice shelf processes.

1.2 Objectives and structure of this thesis

This thesis makes use of a sea ice–ice shelf–ocean model to investigate the role of sea ice in the surface freshwater flux of the southern Weddell Sea with

the particular focus on the coastal polynyas. The aims (**O**) of this thesis are to asses impacts of the following factors on simulating the southern Weddell Sea surface freshwater flux in such a way that it matches the key aspects of the observed system:
O1: The impact of the regionally downscaled atmospheric forcing,
O2: The impact of the stationary icescape features, and
O3: The influence of sea ice parameterizations.

Furthermore, based on the different sensitivity experiments that are used to investigate the above factors, I asses how changes in the surface freshwater flux influence the production rate and properties of the HSSW formed on the continental shelf, and the basal melt of FRIS.

The thesis is structured as follows. In Chapter 2 the numerical model and data are introduced. The reference FESOM simulation is analyzed and compared to observations in Chapter 3. In Chapter 4, sensitivity of the surface freshwater flux to the atmospheric forcing (**O1**) and the impact of the icescape (**O2**) are investigated. In Chapter 5, I derive an optimized simulation based on the conclusions from the previous chapters while using a statistical approach to constrain the sea ice model parameters (**O3**). Finally, Chapter 6 summarizes the results of this thesis, gives a conclusion and provides an outlook.

Remark: Chapters 3 and 4 contain expanded version of the research presented in Stulic et al. (2023). I have set up the model, carried out the experiments, analyzed the results, produced all figures except Fig.2, and wrote the manuscript (Stulic et al. 2023) with contributions of all co-authors. Stephan Paul produced and visualized the MODIS fast-ice data in Fig. 2. of the paper (Fig. 2.5 in this thesis), as well as co-wrote the text that appears in section 2.3.2 of this thesis. Günther Heinemann and Ralph Timmermann helped to conceive the study and provided support with numerical simulations. Rolf Zentek performed atmospheric simulations and provided the atmospheric model data used in Stulic et al. (2023) and in this thesis.

2. Methods and data

This chapter introduces the unstructured multi-resolution global sea ice–ocean model with an ice shelf component and describes the various data sets I used to compare and/or constrain the model results.

2.1 Sea ice–ice shelf–ocean model FESOM

The model used in this thesis for investigation of the southern Weddell Sea surface freshwater flux is the global Finite Element Sea ice–ice shelf–Ocean Model (FESOM; Timmermann et al. 2012, Wang et al. 2014) developed at Alfred Wegener Institute, Helmholtz Centre for Polar and Marine Research (AWI). FESOM is the first global ocean general circulation model using unstructured meshes that was developed for climate research. Its multi-resolution capability makes it a great tool for simulation of the processes depending on the model resolution, such as eddies or coastal polynyas, as well as for a better representation of the particular regions of interest, such as certain ocean basins and ice cavities. FESOM has been found suitable for studies of the Arctic Ocean (e.g. Wekerle et al. (2013), Wang et al. (2018)) and the Southern Ocean ice–ocean–ice shelf systems (e.g. Timmermann et al. (2012), Timmermann & Hellmer (2013), Nakayama et al. (2014), Naughten et al. (2018)).

The Finite Element Method (FEM) is utilized to solve the governing equations of the sea ice–ocean–ice shelf system in FESOM. The hydrostatic primitive equations are solved by the ocean component of the model as described by Danilov et al. (2004), Timmermann et al. (2009), Wang et al. (2014). Details of the dynamic-thermodynamic sea ice component are described by Timmermann et al. (2009) and Danilov et al. (2015), while the ice-shelf component is described by Timmermann et al. (2012).

The governing equations are solved on a horizontal grid consisting of

triangular elements at the surface. In the vertical, the nodes are aligned below the surface nodes forming prisms which are cut creating the tetrahedral elements. The model can be used with z-level grids or hybrid grids that combine z-levels with the terrain-following (sigma) layers.

A version of FESOM (FESOM2, Scholz et al. 2019) that uses the finite volume method and significantly improves the computational efficiency of the model has been developed at AWI, and recently coupled to the ice-shelf model (Wekerle et al. 2024).

In the next section, I will revisit the main equations solved by FESOM that are relevant for this study.

2.1.1 Main equations

The hydrostatic primitive equations in spherical geometry are solved by the ocean model for horizontal ocean velocity $\mathbf{v}$ (vertical velocity w is calculated diagnostically), sea surface elevation η, salinity S and potential temperature θ. The momentum balance equation 2.1, the vertically-integrated continuity equation 2.2 and the hydrostatic balance equation 2.3 are solved in the dynamical part:

$$\partial_t \mathbf{v} + \mathbf{v} \cdot \nabla_3 \mathbf{v} + f\mathbf{k} \times \mathbf{v} + \frac{1}{\rho_0}\nabla p + g\nabla\eta = \nabla \cdot A_h \nabla \mathbf{v} + \partial_z A_v \partial_z \mathbf{v} \ , \tag{2.1}$$

$$\partial_t \eta + \nabla \cdot \left(\int_{z=-H}^{z=\eta} \mathbf{v} \ \mathrm{d}z \right) = 0 \ , \tag{2.2}$$

$$\partial_z p = -g\rho \ , \tag{2.3}$$

where g is the gravitational acceleration in the vertical direction z, ρ is the deviation from the mean density ρ_0, and H is the local ocean depth below $z = 0$. A_h and A_v are horizontal and vertical viscosity coefficients.

Tracer equations describe the evolution of the potential temperature θ and the salinity S:

$$\partial_t \theta + \mathbf{v} \cdot \nabla_3 \theta - \nabla \cdot K_h \nabla \theta - \partial_z K_v \partial_z \theta = 0 \tag{2.4}$$

$$\partial_t S + \mathbf{v} \cdot \nabla_3 S - \nabla \cdot K_h \nabla S - \partial_z K_v \partial_z S = 0 \ , \tag{2.5}$$

where K_h and K_v are horizontal and vertical diffusivites, respectively.

While no-slip boundary conditions are applied along the coast, the surface boundary conditions (surface stress, heat and salt fluxes) are derived from the ice-ocean coupling. To parameterize the effects of subgrid-scale processes on the horizontal tracer distribution, mixing along neutral density surfaces following Redi (1982) is applied on the z-levels. The additional velocity is added to the tracer equations to represent the effects of mesoscale eddies (GM; (Gent & Mcwilliams 1990, Gent et al. 1995)). On the sigma grid, the along-sigma diffusivity is used, as using neutral physics parameterization (GM/Redi) leads to numerical instabilities (Wang et al. 2014). The convective and wind-driven vertical mixing in the ocean surface boundary layer is parameterized using k-profile parameterization (KPP; Large et al. 1994), while salt plume parameterization (Nguyen et al. 2009) is used in addition to redistribute the salt flux within the mixed layer.

2.1.2 Sea ice model

The configuration of the sea ice component of the model (Finite-Element Sea Ice Model; Timmermann et al. (2009), Danilov et al. (2015)) applied in this study uses the zero-layer thermodynamical component and elastic-viscous-plastic rheology following Hunke & Dukowicz (1997) for computation of ice and snow drift. The sea ice concentration a, the ice mean thickness (sea ice volume per unit area) h_i, and snow mean thickness h_s are advected by the ice velocities and modified through thermodynamical forcing.

The dynamical part of the model solves the sea ice momentum equation:

$$m(\partial_t + \mathbf{f}\times)\mathbf{u} = a\boldsymbol{\tau} - c_{d,io}a\rho_w(\boldsymbol{u} - \boldsymbol{u_w})|\boldsymbol{u} - \boldsymbol{u_w}| + \boldsymbol{F} - mg\nabla\eta, \qquad (2.6)$$

where m is the ice plus snow mass per unit area, $c_{d,io}$ the ice-ocean drag coefficient, ρ_w the sea water density, $\boldsymbol{u} = (u, v)$ the ice velocities, and $\boldsymbol{u_w} = (u_w, v_w)$ ocean surface velocities, $\boldsymbol{\tau}$ the wind stress, η the sea surface height, and g the gravitational acceleration. The wind stress $\boldsymbol{\tau}$ is computed assuming that the ocean surface velocity is negligible compared to the 10-m wind velocity ($\boldsymbol{u_{10}}$):

$$\boldsymbol{\tau} = \rho_a c_{d,ai}|\boldsymbol{u_{10}}|\boldsymbol{u_{10}}, \qquad (2.7)$$

where $c_{d,ai}$ is the atmosphere-ice drag coefficient and ρ_a the air density.

$\boldsymbol{F} = \nabla\boldsymbol{\sigma}$ is the force from the internal ice stress which is computed using elastic–viscous–plastic (EVP) rheology. The formulation of the sea-ice strength P used in the EVP solver is following Hibler (1979):

$$P = P^* h_i e^{-C^*(1-a)}, \tag{2.8}$$

where P^* and C^* are empirical parameters (default values used in this study are $P^* = 15000$ Nm^{-2} and $C^* = 20$). Details of the dynamical part and the solver algorithms implemented in the model are described in Danilov et al. (2015).

The thermodynamical part is implemented following Parkinson & Washington (1979) and includes a prognostic snow layer (Owens & Lemke 1990) and effects of snow-ice conversion due to flooding. The heat flux components are calculated separately for the ice-covered and the ice-free part and weighted accordingly with a and $(1 - a)$. The atmospheric heat flux Q_a is calculated following Parkinson & Washington (1979) as combination of the shortwave radiative heat flux, the longwave radiative heat flux, the sensible and latent heat fluxes. After the ocean surface temperature reaches the freezing point, additional heat loss is converted into sea ice production. The open water heat flux (Q_{ow}) is a sum of the atmosphere-ocean heat flux (Q_{aw}) and the heat flux involved in the sea ice production:

$$Q_{ow} = Q_{aw} + \rho_i L_f (\frac{\partial h_i}{\partial t})_w, \tag{2.9}$$

where ρ_i is the sea ice density and L_f is the latent heat of fusion.

The total ocean surface heat flux Q_o is:

$$Q_o = Q_{ow}(1 - a) + Q_{oi}a, \tag{2.10}$$

where Q_{oi} is the heat flux from the ocean to the sea ice. Q_{oi} is parameterized as:

$$Q_{oi} = \rho_w c_p c_t \sqrt{c_d} |\boldsymbol{u} - \boldsymbol{u_w}| (T_o - T_f), \tag{2.11}$$

where c_p is the specific heat capacity of sea water at constant pressure, c_t the transfer coefficient, T_o surface ocean temperature and T_f the local freezing temperature.

The surface freshwater flux, which contributes to the surface boundary conditions for the ocean tracer equations, is described in more detail next.

Surface freshwater flux

As described by Timmermann et al. (2009), the net surface freshwater flux at the ocean surface in the model comprises of atmospheric fluxes (precipitation and evaporation), sea ice growth and melt, snow melt fluxes, as well as the melt flux from the ice-shelf base. While precipitation (P) and evaporation (E) are given by the atmospheric forcing, other fluxes are calculated by the sea ice and ice-shelf model.

The freshwater flux F_i due to freezing/melting of ice and melting of snow is calculated as:

$$F_i = \frac{(S_{ref} - S_i)}{S_{ref}} \frac{\rho_i}{\rho_w} \frac{\partial h_i}{\partial t} + \frac{\rho_s}{\rho_w} \frac{\partial h_s}{\partial t}, \tag{2.12}$$

where h_i and h_s are ice and snow thickness, respectively. The changes in sea ice and snow thickness, $\frac{\partial h_i}{\partial t}$ and $\frac{\partial h_s}{\partial t}$ are calculated following Parkinson & Washington (1979) thermodynamics by the sea ice model. Sea ice salinity S_i is taken to be 5 psu and salinity of snow S_s is assumed to be zero. The reference salinity S_{ref} used for conversion between the freshwater and salt fluxes is taken to be the local time-evolving ocean surface salinity. The density of sea ice is $\rho_i = 910$ kgm^{-3} and density of snow $\rho_s = 290$ kgm^{-3}.

The freshwater flux of the ocean covered part of the grid cell F_w depends on the air temperature (T_a) and percentage of the grid covered by ice (A) in the following way:

$$F_w = \begin{cases} P - E & T_a \geq 0°C \\ (1 - A)(P - E) & T_a < 0°C. \end{cases} \tag{2.13}$$

If the air temperature is above the freezing point of freshwater ($T_a \geq 0°C$), the net atmospheric flux $P - E$ is applied directly to the ocean. For the temperatures below freezing point ($T_a < 0°C$), only the fraction $1 - A$ of the net atmospheric flux is applied to the ocean, while the rest is accumulated as snow on the ice-covered part. The resulting freshwater flux calculated by

the sea ice model is a sum of Eq. 2.12 and Eq. 2.13:

$$F = F_i + F_w. \tag{2.14}$$

The impact of the freshwater flux F on the ocean salinity is parameterized using a virtual salt flux formulation:

$$F_{salt} = S_{ref} F. \tag{2.15}$$

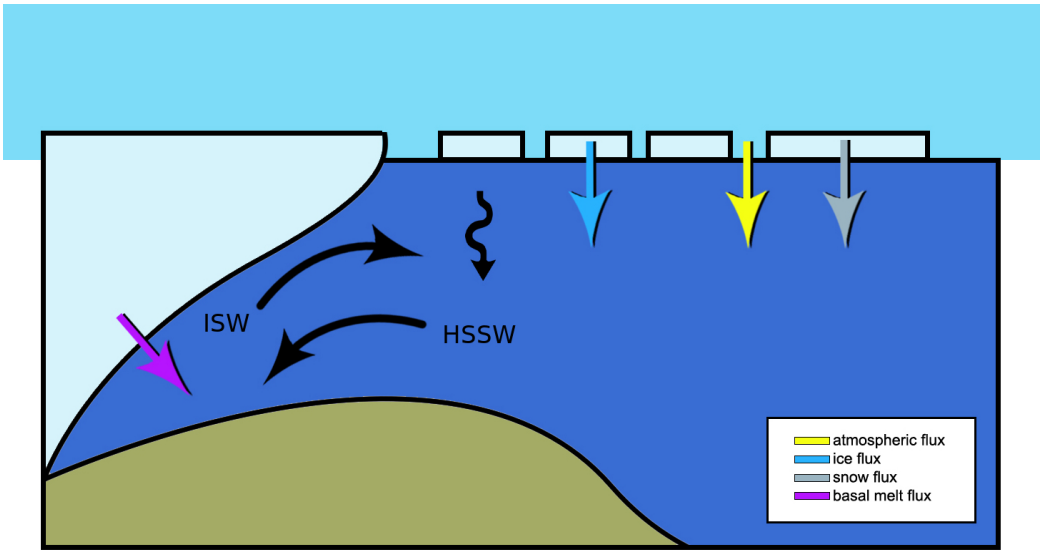

Figure 2.1: Schematic cross-section of the southern Weddell Sea continental shelf. Components of the surface freshwater are indicated by colored arrows: atmospheric flux, sea ice and snow related fluxes and basal melt. The idealized circulation of the watermasses participating in the sub ice-shelf circulation is indicated by black arrrows.

The resulting salt flux is then applied to the ocean model surface nodes and redistributed using a combination of KPP and salt plume parameterizations.

The melt rate at the ice-shelf base provides another source of freshwater and is calculated by the ice-shelf model.

2.1.3 Ice shelf model

The ice-shelf component of the model (Timmermann et al. 2012) solves the three-equation system to compute temperature and salinity in the boundary layer between ice and ocean and melt rate at the ice-shelf base following

Hellmer & Olbers (1989) and Holland & Jenkins (1999). The process of frazil ice growth in supercooled parts of the interior water column is not considered. The cavity is assumed to have a constant geometry, and turbulent fluxes are computed depending on the friction velocity (Jenkins 1991).

The model calculates the freezing point of sea water at the ice-ocean interface, and solves the salt and heat conservation during any phase changes at the interface. The divergence of the heat flux at the ice-ocean interface balances the latent heat flux caused by freezing or melting (Q_{lat}):

$$Q_i - Q_o = Q_{lat}\cdot, \tag{2.16}$$

where Q_i is the conductive heat flux through ice shelf and Q_o is the diffusive heat flux in the oceanic boundary layer. Q_i and Q_o are parameterized following Holland & Jenkins (1999). The latent heat term is given by:

$$Q_{lat} = -m_i L_f, \tag{2.17}$$

where m_i is the mass of ice being melted or frozen. Similarly, the salt flux divergence at the ice-ocean interface is balanced by sink or source of salt flux associated with melting or freezing (S_f):

$$S_i - S_o = S_f, \tag{2.18}$$

where diffusive salt flux through ice shelf (S_i) is zero, while diffusive salt flux in the oceanic boundary layer (S_o) is parameterized depending on the friction velocity (Holland & Jenkins 1999).

2.1.4 Experimental design

The FESOM equations are solved using an unstructured surface triangular grid such as the one shown in Fig. 2.2 which is used for all the simulations in this thesis. Due to the limited computational resources, the horizontal mesh resolution is kept coarse in large parts of the global ocean, and refined in the Weddell Sea region and particularly on the southern Weddell Sea continental shelf to resolve the processes relevant for this study, such as coastal polynyas. Horizontal grid resolution varies between 3 km under the Weddell Sea ice shelves and up to 25 km in the offshore Weddell Sea, and increases to the maximum of 250 km in the Atlantic and Pacific Oceans (Fig. 2.3).

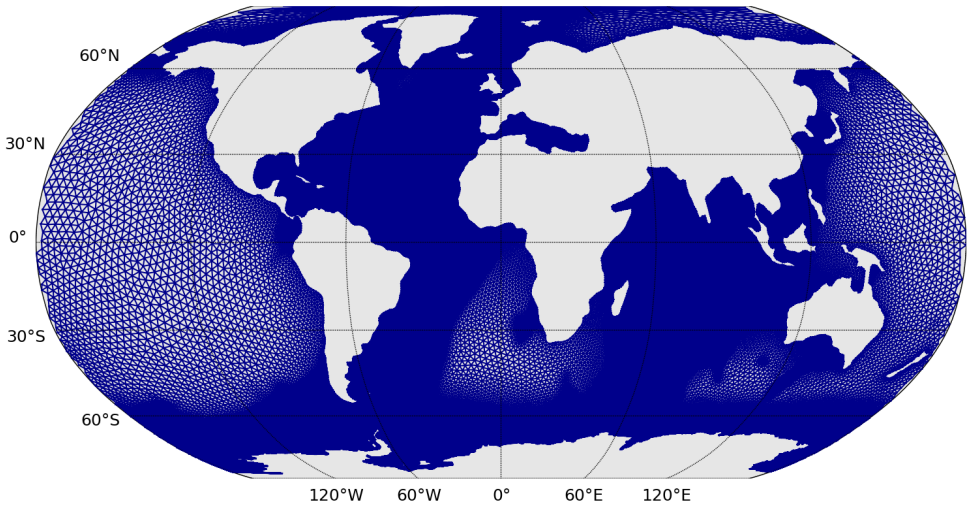

Figure 2.2: FESOM surface grid used for this study.

The terrain following sigma grids allow for a flexible vertical refinement and a better representation of the overflow processes across the steeply sloping topography (Wang & Meredith 2008), such as the Weddell Sea continental shelf. In the same time, they allow for a better representation of the ice shelf base and draft, continuous variation of top-layer thickness and better vertical resolution distribution in the ice shelf cavities. When using sigma grids, however, problems may arise from a spurious advection and diffusion induced along sigma layers (e.g. Mellor et al. (1994), Lemarié et al. (2012)). Here, a hybrid vertical coordinate system with 36 layers is used. Sigma coordinates are used for the depths shallower than 2500 m around Antarctica, in the rest of the ocean the z-level discretization is applied. Ice-shelf draft, cavity geometry, and global ocean bathymetry have been prepared from the 1-minute version of RTopo-2 (Schaffer et al. 2016).

The model was initialized in 1979 from temperature and salinity derived from the World Ocean Atlas data 2009 (Levitus et al. 2010), and run until the end of 2001 (lERA) using the atmospheric forcing from the ERA-Interim reanalysis (ERA, Dee et al. 2011). The experiments discussed in chapters 3 and 4 of this thesis (Table 2.1) are derived from the conditions at the end of this simulation in 2001.

The reference experiment (BRIDGE) discussed in Chapter 3 is extended until the end of 2017 using regionally downscaled forcing from the regional atmosphere model with 14 km horizontal resolution and, where available, incorporating effects of the grounded iceberg and the ice bridge as described

Experiment	BRIDGE	noBRIDGE	cATMO	statBRIDGE
Years	2002–2017	2002–2017	2002–2017	2015–2017
Atmospheric forcing	CCLM	CCLM	ERA	CCLM
Fast ice bridge	monthly variable	none	none	stationary

Table 2.1: Experiments analysed in chapters 3 and 4 of this thesis.

in section 2.3.2. To investigate the impact of the icescape, I conducted a sensitivity experiment without prescribing the blocking effect (i.e. blocking the movement of sea ice) of the varying icescape (noBRIDGE). An additional experiment (cATMO) without the blocking effect and using ERA as an atmospheric forcing everywhere was conducted to investigate the impact of the high-resolution atmospheric forcing used in the reference experiment. Both sensitivity experiments were initialized from the same conditions as BRIDGE and run for the same period, 2002–2017. Another 3-year simulation was extended from the conditions of the BRIDGE experiment at the end of 2014, with the same setup as BRIDGE except with the static fast-ice conditions (statBRIDGE). These experiments are analyzed in Chapter 4.

2.1.5 Transport estimates and watermass production

An analysis of sea ice and watermass transport is useful for the interpretation of the model results and for the comparison with observation-based estimates. Calculation of transports is not a part of the standard diagnostics in FESOM. Transports can be calculated subsequently from the model results, however interpolation of the model results horizontally and/or vertically on a defined section is required in the process.

Sea ice transport

For calculation of sea ice transport in this thesis, daily sea ice concentration, thickness and velocity from FESOM are first interpolated on a defined section using distance-weighted k-nearest neighbor (k=3) approach. The transport F of sea ice area or sea ice thickness is then calculated using a simple trapezoidal rule:

$$F = \sum_{i=1}^{i=n-1} (u_i + u_{i+1}) c_i \frac{\Delta d}{2}, \tag{2.19}$$

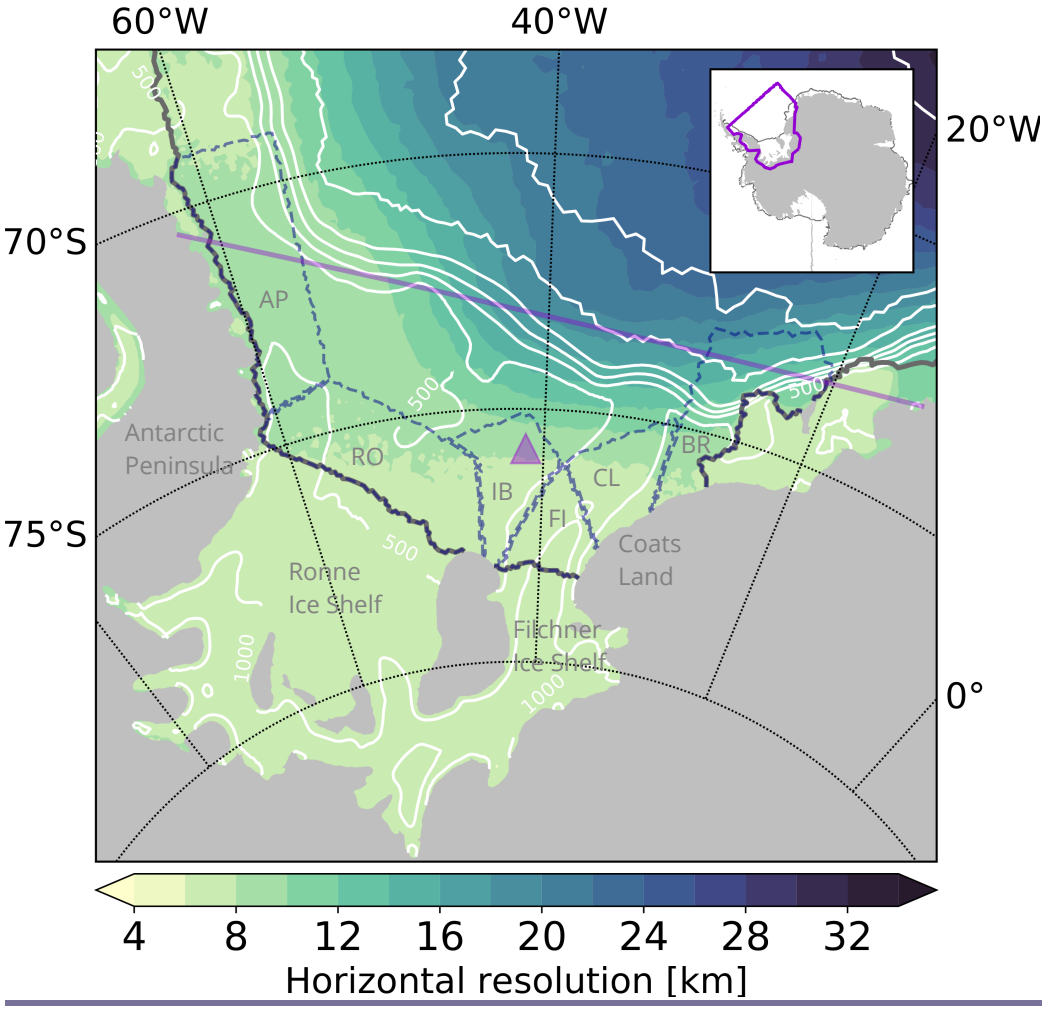

Figure 2.3: Horizontal resolution (km) over the Weddell Sea sector for the FESOM simulations. The ice shelf edge is contoured in gray, and isobaths are in white. The southern Weddell Sea control region is bounded to the north by the violet line following Drucker et al. (2011). The six sub-regions for comparison of polynya ice production (adapted from Paul et al. (2015)) are enclosed by dashed gray lines: Antarctic Peninsula (AP), Ronne Ice Shelf (RO), the area around the ice mélange (IB), Filchner Ice Shelf (FI), Coats Land (CL) and Brunt Ice Shelf (BR). The location of the grounded iceberg A23-A for 2002–2017 is marked by a triangle (data from the Antarctic Iceberg Tracking Database; https://www.scp.byu.edu/data/iceberg/database1.html, last access: 22 March 2023; (Budge & Long 2018).

where u is magnitude of velocity perpendicular to the section, c is sea ice variable in question, Δd is the distance between the points and n number of points on the section. The distance between the points on the section (Δd) is taken to be approximate to the average of model resolution at the nearest neighbor points used for the interpolation.

The export of sea ice from the southern Weddell Sea is calculated across

the gates enclosing the southern Weddell Sea continental shelf as shown in Fig. 2.3.

HSSW production

For the watermass transport, an interpolation of the ocean velocity, temperature, and salinity from sigma layers to the z-levels is required. The elements of the two-dimensional section across which the transport is calculated are taken to be the quadrilaterals.

To examine the production rate of HSSW on the southern Weddell Sea continental shelf, the volume budgets in the control volumes have been calculated in the potential temperature-salinity space. For the watermass with the potential temperature θ and salinity S, the daily production rate R for the control volume is calculated as:

$$R(\theta, S, t) = \frac{\partial V(\theta, S, t)}{\partial t} - \Delta\Psi(\theta, S, t), \tag{2.20}$$

where $\frac{\partial V(\theta,S,t)}{\partial t}$ is the change in volume of water of a given θ and S within the control volume, while $\Delta\Psi(\theta, S, t)$ is the net flux of the water with the same properties into the control volume. The annual production rate of HSSW is calculated from the daily data over temperature-salinity classes in the HSSW range (temperature -1.9 $< \theta <$ -1.5 °C; salinity S>34.6 psu, with intervals of 0.05 psu). Only positive values of the daily production rate R (i.e. the volume gain) are accounted for the annual watermass production estimates.

2.2 Atmospheric forcing

2.2.1 ERA-Interim reanalysis

The ERA-Interim reanalysis (ERA, Dee et al. 2011) product on a 75 km horizontal grid is used as atmospheric forcing for all of the experiments in this thesis, either alone (Chapter 4) or combined with the regional atmospheric model data (chapters 3, 4,and 5). The fields used as a forcing include 6-hourly air temperature and dew point temperature (both at 2 m altitude), and wind fields at 10 m altitude, as well as 12-hourly average shortwave and longwave radiation, precipitation and evaporation.

2.2.2 Regional atmospheric model COSMO-CLM

I use data from a regional atmospheric model to incorporate the impact of a regionally downscaled atmospheric forcing on the surface freshwater flux of the southern Weddell Sea. Atmospheric simulations over the Weddell Sea were performed using the non-hydrostatic atmospheric model COSMO-CLM (CCLM, Rockel et al. 2008, Steger & Bucchignani 2020) as described by Zentek & Heinemann (2020). CCLM was adapted for polar conditions using a thermodynamic sea ice module (Schröder et al. 2011, Heinemann et al. 2021) with snow cover and a temperature-dependent albedo scheme (Gutjahr et al. 2016). Topography was derived from RTopo-2 (Schaffer et al. 2016), while ERA-Interim data was used for the initial and boundary conditions. Daily sea-ice concentrations were taken from the satellite measurements (AMSR-E, SSMI/S, AMSR2, Spreen et al. 2008) to allow for a more realistic polynya representation. Here, daily simulations performed with a 6-hours spin-up time and 0.125° (13.9 km) resolution are used for the period 2002–2017. In the experiments BRIDGE (Chapter 3) and noBRIDGE (Chapter 4), CCLM is applid as a forcing over the Weddell Sea, whereas, consistent with the CCLM boundary conditions, ERA is used in other regions. In a zone surrounding the boundaries of the Weddell Sea and extending over 2°, the two forcings are combined using bilinear interpolation to ensure a smooth transition.

CCLM was validated with observations and compared to reanalyses by Zentek & Heinemann (2020). A comparison of CCLM for one year with measurements over the sea ice of the Weddell Sea shows small biases for temperature and wind speed (around ±1 °C and 1 m s^{-1}, respectively).

2.3 Data

While data from the passive microwave sensors can be used to give temporally and spatially continuous observations of the sea ice concentration, the observation-based estimates of sea ice thickness and snow thickness for the Weddell Sea over the period investigated in this thesis (2002–2017) are sparse, both in time and in space, and rely on methodologies that have high uncertainties. Furthermore, the perennial ice cover makes in-situ ocean observations in the southern Weddell Sea difficult and limited to summer months. The limitations that need to be taken into account when comparing the model to the available data, together with the details of each data set,

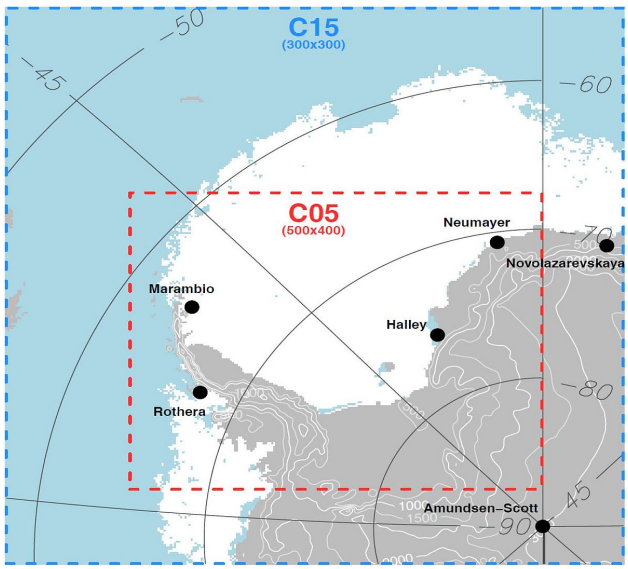

Figure 2.4: Overview of the CCLM simulations domain and locations of 6 surface stations (circles). The domain of the CCLM simulation used in this study (C15) is marked by the dashed blue line. Topography contours are plotted every 500 m and sea ice concentration higher than 70% for the 1 June 2015 is shown in white. Figure courtesy of Rolf Zentek.

will be discussed next.

2.3.1 Sea ice data

Sea ice concentration

Sea ice concentration (areal fraction of ice within a grid cell) can be estimated from combinations of passive microwave brightness temperatures at different frequencies and polarizations. A Climate Data Record (CDR) of sea ice concentration from passive microwave (SSM/I) data (Peng et al. 2013) combines estimates of ice concentration from the NASA Team algorithm (Cavalieri et al. 1984) and NASA Bootstrap algorithm (Comiso 1986). Daily and monthly sea ice concentrations (1978–2019) for the southern hemisphere are available on a 25 km x 25 km grid (Meier et al. 2017). The standard deviation of sea ice concentration is provided with the dataset. The data is most reliable for the consolidated ice pack during winter conditions (typical uncertainties being 5–10%), and less reliable during melting conditions at the ice edge (uncertainties up to 20%). This data set is used to asses variability of the simulated sea ice area in the Weddell Sea (Chapter 3), as well as to constrain the sea ice model parameters (Chapter 5).

Sea ice motion

Sea ice velocity data (Kwok et al. 2017) is available for March–November 2002–2014 on a 100 km horizontal grid. The sea ice motion estimates are

based on the ice drift derived from two satellite radiometer channels (37 GHz and 85GHz–91 GHz since 2009). The uncertainties of the daily sea ice motion data are estimated to be 3–4 km day^{-1}. The coarse resolution of the dataset is suitable to asses the simulated large scale sea ice velocity patterns in the Weddell Sea sector and is used to constrain the sea ice velocity patterns in Chapter 5. The sea ice export estimates based on this data-set are compared to FESOM results in Chapter 3.

2.3.2 MODIS ice bridge

[1]

A striking feature in the southern Weddell Sea icescape (2002–2017) has been the ice mélange forming between Berkner Island and the grounded iceberg A23-A (Fig. 2.5). The iceberg A23-A broke off from the Filchner Ice Shelf in 1986. It stayed grounded in the region since 1991 (Fig. 1.4). The iceberg started moving again in 2020, and ultimately, since the beginning of 2022, it has been moving out of the region (iceberg locations from the Antarctic Iceberg Data (USNIC), `https://usicecenter.gov/Products/AntarcIcebergs`, last access August 15, 2023, and Antarctic Iceberg Tracking Database, `https://www.scp.byu.edu/data/iceberg/database1.html`, last access March 22, 2023, Budge & Long (2018)). As shown in Fig. 2.5(a,b), higher temperatures associated with leads and polynya openings are detected in MODIS *ice-surface temperature* retrievals west of the iceberg A23-A and Berkner Island, and in front of the Filchner Ice Shelf. The persistent absence of cracks, leads, or polynyas in a well-defined area indicates stationary sea ice conditions between Berkner Island and iceberg A23-A in August 2009. In contrast, in August 2011, leads and polynyas can be found in the same area (Fig. 2.5, d, e). A similar pattern of leads forming with a high frequency west of Berkner Island and A23-A, and low frequency between the tip of the Berkner Island and A23-A has been reported from the long-term (2003–2019) data derived from the thermal infrared satellite measurements (Reiser et al. 2019). Smaller icebergs, bergy bits, and accumulation of platelet ice (Hoppmann et al. 2020) are possible processes responsible for the formation of the ice bridge. These processes are subject to variability and are not represented in the current sea ice–ocean models, including FESOM. With the use of MODIS ice-surface

[1] The content of this section appears in Stulic et al. (2023) and has been made with the contribution from Stephan Paul who produced and visualized the MODIS data in Fig. 2.5

temperature data (Hall & Riggs 2015), we are able to get information about the existence, location, and extent of the ice bridge. We use daily median ice-surface temperature from the cloud-corrected data (Paul et al. 2015) for April–September 2002–2017. We calculate daily temperature anomalies by subtracting the spatially averaged ice-surface temperature from each daily composite. Subsequently, for each month, the median of the ice-surface temperature anomaly is calculated per pixel from all daily anomalies. Under the assumption that persistent and immobile sea ice cover leads to lower-than-average monthly median temperature, negative values of anomalies exceeding amplitudes of 3 K are used to define the monthly fast-ice locations, meaning that e.g. in 2009 the ice bridge extended between A23-A and Berkner Island, whereas in 2011, the fast ice did not extend over the entire distance (Fig. 2.5, c, f). The fast-ice locations are mapped on the FESOM grid using the nearest-neighbor approach.

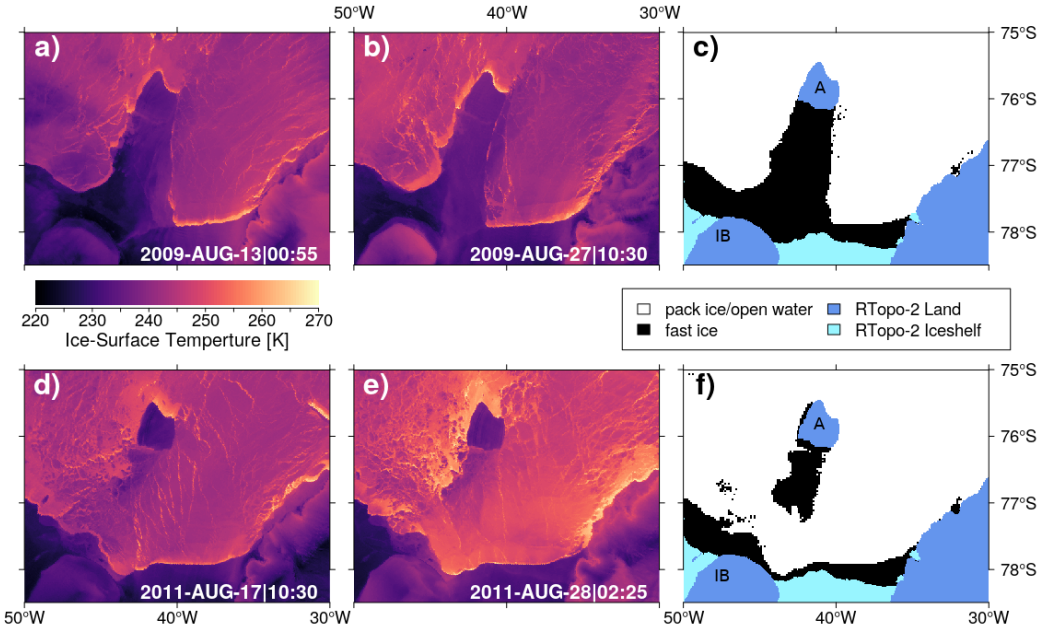

Figure 2.5: Comparison of the ice-surface temperatures from several single MODIS swaths from August 2009 (a, b) and August 2011 (d, e) and the derived fast-ice masks (c, f) with added marks for Berkner Island (IB) and grounded iceberg A23-A (A). Antarctic ice shelves and land configuration are based on RTopo-2 (Schaffer et al. 2016). Figure courtesy of Stephan Paul (Fig.2 from Stulic et al. (2023)).

2.3.3 Hydrographic profiles

Historical Conductivity–Temperature–Depth (CTD) measurements obtained between 1979 and 2017 south of 65°S are used to asses the simulated water-mass properties on the continental shelf of the southern Weddell Sea. Furthermore, temperature and salinity profiles obtained between 2002 and 2011 south of 65°S are used to evaluate the model-data differences and constrain the optimized solution in Chapter 5. For comparison with the model, the data are interpolated onto the model grid (horizontally and by depth). The measurement accuracy is 0.005°C for temperature and 0.005 psu for salinity.

2.4 Green's function method

With the aim to obtain an improved estimate of the southern Weddell Sea surface freshwater flux, in Chapter 5 I apply the Green's function method to constrain the sea ice model and reduce biases in the sea ice-ocean conditions on the southern Weddell Sea continental shelf. The Green's function approach provides a simple and effective method to study and quantify general circulation model (GCM) errors, calibrate model parameters and correct the model biases (Menemenlis et al. 2005). They have been applied to constrain the ocean parameterizations and improve the ocean state (Menemenlis et al. 2005), to constrain the sea ice parameters and improve the Arctic sea ice state (Zampieri et al. 2021), as well as to constrain both the sea ice and ocean parameterizations in an Arctic modeling study (Nguyen et al. 2011) and a study of the Amundsen Sea (Nakayama et al. 2017).

The Green's function approach involves the computation of GCM sensitivity experiments for each parameter considered for the optimization, followed by a recipe to construct the optimized solution and estimate the optimized model parameters. In the process, Green's functions are used to linearize the GCM around the particular model solution, and inverse method to estimate the optimal model parameters. While the approach is limited by the computational cost that increases linearly with the number of parameters, compared to the other state estimation methods (e.g. adjoint methods), the Green's function method is fairly simple to implement and provides effective way to correct model biases by optimizing the model parameters. The detailed mathematical description of the Green's function approach can be found in textbooks (e.g. Wunsch (2006)), here I provide a short description

following Menemenlis et al. (2005).

A GCM can be thought as a set of rules for evaluating the state vector $\boldsymbol{x}(t)$ in time:

$$\boldsymbol{x}(t + \Delta t) = M(\boldsymbol{x}(t), \boldsymbol{\eta}). \tag{2.21}$$

In case of the sea ice–ice shelf–ocean model used here, the state vector $\boldsymbol{x}(t)$ includes sea ice concentration, sea ice thickness and velocity, ocean temperature and salinity, etc. Accordingly, the operator M represents the known model time-stepping rules and depends on the choice of model parameters, such as initial and boundary conditions, albedos and drag coefficients. The uncertain model parameters that are to be optimized are represented by vector $\boldsymbol{\eta}$ with mean $\boldsymbol{\eta_0}$ and covariance $\boldsymbol{Q}$.

The relationship between state vector $\boldsymbol{x}$ and vector of observations $\boldsymbol{y}$ can be expressed as:

$$\boldsymbol{y} = H(\boldsymbol{x}) + \boldsymbol{\varepsilon}, \tag{2.22}$$

where operator H describes the measurement process (i.e. sampling the observations), while vector $\boldsymbol{\varepsilon}$ represents measurement errors and model errors that are not included in $\boldsymbol{\eta}$. Vector $\boldsymbol{\varepsilon}$ is assumed to have zero mean and covariance $\boldsymbol{R}$. By combining 2.21 and 2.22, observation vector $\boldsymbol{y}$ can be written as:

$$\boldsymbol{y} = G(\boldsymbol{\eta}) + \boldsymbol{\varepsilon}, \tag{2.23}$$

where operator G combines the integration of the model M with the measurement operator H.

The practical difficulty in solving 2.23 for $\boldsymbol{\eta}$ is that G is, in general, a highly non-linear operator. It is therefore assumed that G can be linearized about a baseline model integration $G(\boldsymbol{\eta_0})$ conducted with the best prior estimate of model paramteres $\boldsymbol{\eta_0}$, so 2.23 can be simplified to:

$$\boldsymbol{\Delta y} = \boldsymbol{y} - G(\boldsymbol{\eta_0}) = \boldsymbol{G}\boldsymbol{\Delta\eta} + \boldsymbol{\varepsilon}, \tag{2.24}$$

where $\boldsymbol{\Delta y}$ is the model-data difference, and $\boldsymbol{\Delta\eta}$ is the perturbation of model parameters around $\boldsymbol{\eta_0}$ ($\boldsymbol{\Delta\eta} = \boldsymbol{\eta} - \boldsymbol{\eta_0}$). The validity of the linearity assumption will be further discussed in Chapter 5. Columns of matrix $\boldsymbol{G}$ are

referred to as Green's functions of G, each being solution of a model sensitivity experiment with the perturbed value of a corresponding parameter from $\boldsymbol{\eta}$.

The parameters $\boldsymbol{\eta}$ can then be estimated by minimizing a weighted least-squares cost function that measures the model parameter perturbation and the model-data misfit:

$$J = \Delta\boldsymbol{\eta}^T \boldsymbol{Q}^{-1} \Delta\boldsymbol{\eta} + \boldsymbol{\varepsilon}^T \boldsymbol{R}^{-1} \boldsymbol{\varepsilon}. \tag{2.25}$$

The optimization using Green's function approach in this study is carried out for the nine sea ice model parameters using in total approximately 3×10^6 observations. In a case of an overdetermined problem such as here, that is, if the number of observations is much larger than the number of parameters, the specification of error covariance matrices $\boldsymbol{R}$ and $\boldsymbol{Q}$ is not expected to change a solution much since the small number of parameters limits the problem's degrees of freedom (Menemenlis et al. 2005).

If there is no prior information about the model parameters to be optimized ($\boldsymbol{Q}^{-1} = 0$), equation 2.25 can be simplified to:

$$J = \boldsymbol{\varepsilon}^T \boldsymbol{R}^{-1} \boldsymbol{\varepsilon}. \tag{2.26}$$

The error ε is model-data difference ($\varepsilon_i = y_i - x_i$) and $\boldsymbol{R}$ is assumed to be a diagonal matrix with elements $R_{ii} = \sigma_i^2$, where σ_i^2 is assumed data error variance of the i^{th} observation. Each element of $\boldsymbol{R}$ is further weighted so that each observation type employed for the calculation of cost function J in this study contributes equally.

Minimizing Eq. 2.26 given Eq. 2.24 yields:

$$\boldsymbol{\Delta\eta_{opt}} = (\boldsymbol{G}^T \boldsymbol{R}^{-1} \boldsymbol{G})^{-1} \boldsymbol{G}^T \boldsymbol{R}^{-1} \boldsymbol{\Delta y}. \tag{2.27}$$

From Eq. 2.27, an optimized set of parameters can be calculated as:

$$\boldsymbol{\eta_{opt}} = \boldsymbol{\eta_0} + \boldsymbol{\Delta\eta_{opt}}. \tag{2.28}$$

As has been demonstrated by e.g. Menemenlis et al. (2005) and Nguyen et al. (2011), the new model integration using optimized parameters $\boldsymbol{\eta_{opt}}$ can lead to a substantial cost reduction, even when only a small number of parameters is considered.

2.5 Cost function

In Chapter 5, I use a sequential approach to obtain an optimal solution for the simulated southern Weddell Sea surface freshwater flux. To quantitatively assess model results before and after each optimization step, I utilize a cost function that measures model-data misfit. The cost function is defined as:

$$J_d = \sum_{i=1}^{N_d} \frac{(y_i - x_i)^2}{N_d(y_i)\sigma_i^2} \tag{2.29}$$

where y_i is an observational data point with variance σ_i^2, x_i the corresponding model result, and N_d the number of data points in each data set used to construct the cost function. The cost function in Eq. 2.29 is similar to weighted least squared cost function used for the Green's function approach (Eq. 2.26), but it is calculated for each data type separately. I use sea ice concentration and sea ice motion data, as well as temperature and salinity from the CTD measurements over the southern Weddell Sea, described earlier in this chapter. Each data point in 2.29 is weighted by N_d, so that each data set contributes with equal weight. The coarse resolution of the sea ice motion data makes it suitable for comparing and constraining the large-scale sea ice drift patterns in the Weddell Sea (WS). Moreover, both sea ice data-sets are used to constrain the large-scale sea ice patterns as the higher resolution features, such as coastal polynyas, are not represented well in these products. To still have a constraint on the model performance on the southern Weddell Sea continental shelf, temperature and salinity data from CTDs is used. Due to the dominant effect of the sea ice fluxes on the surface freshwater flux, and water mass transformation in the region, it is expected that improvements in the sea ice state should be reflected in the ocean temperature and salinity cost.

Grounded icebergs and the presence of fast ice influence atmosphere-ocean heat fluxes and freshwater exchanges. Decreased sea ice concentration (Luckman et al. 2010) and thin ice (Paul et al. 2015) can be observed in the proximity of grounded icebergs in the western Weddell Sea. These icebergs are not represented in the model and do not affect simulated conditions on southern Weddell Sea continental shelf. Thus, conditions in areas affected by the icebergs are not realistically simulated in the model. This results in large

local discrepancies between the model and data, which can dominate the sea ice cost. Therefore, I do not take in account the sea ice data from locations in proximity of the icebergs or fast ice outside of my area of interest.

The cost function for all the available data (Eq. 2.26) and separately for each data set (Eq. 2.29) is calculated for the model results before and after each optimization step. The normalized change for each cost function is calculated as:

$$\Delta J = \frac{J_f - J_i}{Ji}, \tag{2.30}$$

where J_i is the cost function calculated from the results of the experiment conducted before, and J_f from the experiment results after the optimization step. ΔJ is used as a measure of improvement ($\Delta J < 0$) or degradation ($\Delta J > 0$) of simulated results in Chapter 5.

Data set	Description	Coverage	Accuracy
Sea ice concentration (sect. 2.3.1)	passive microwave	2002–2017, WS	5–20%
Sea ice velocity (sect. 2.3.1)	passive microwave	March–November 2002-2014, WS	3–4 kmday^{-1}
Ocean temperature (sect. 2.3.3)	CTD	2002–2017, southern WS	0.005 °C
Ocean salinity (sect. 2.3.3)	CTD	2002–2017, southern WS	0.005 psu

Table 2.2: Data sets used for the calculation of cost function.

3. The reference simulation

> The justification of such a mathematical construct [i.e. model] is solely and precisely that it is expected to work.
>
> John von Neumann

If a model represents well some features from the observable world, the mechanisms acting in the model can help to explain the processes acting in the real world. In this chapter, I will investigate the representation of the surface freshwater flux on the southern Weddell Sea continental shelf in a FESOM simulation with regionally downscaled atmospheric forcing and including effects of the ice mélange that was forming between FRIS and A23-A (BRIDGE, 2002–2017).

A longer simulation, initialized in 1979 and run until the end of 2001 (sect. 2.1.4) serves as a quasi spin-up for BRIDGE. The BRIDGE experiment was extended from these conditions until the end of 2017 using downscaled atmospheric forcing from a regional atmospheric model with 14 km horizontal resolution (sect. 2.2.2) and, where available, incorporating effects of the grounded iceberg and the ice bridge based on satellite data (sect. 2.3.2). The BRIDGE experiment serves as the reference for sensitivity experiments investigating impact of the atmospheric forcing and icescape in Chapter 4.

First, I will look into the sea ice concentration, area and thickness over the Weddell Sea from BRIDGE and compare it to the satellite-based estimates. Next, I will asses the simulated net surface freshwater flux and its components over the southern Weddell Sea. A special attention will be on the sea ice production and coastal polynas. At the end, I will examine representation of the watermasses on the southern Weddell Sea continental shelf. the production rate and properties of the HSSW formed on the continental shelf, and the basal melt of FRIS.

3.1 Sea ice concentration

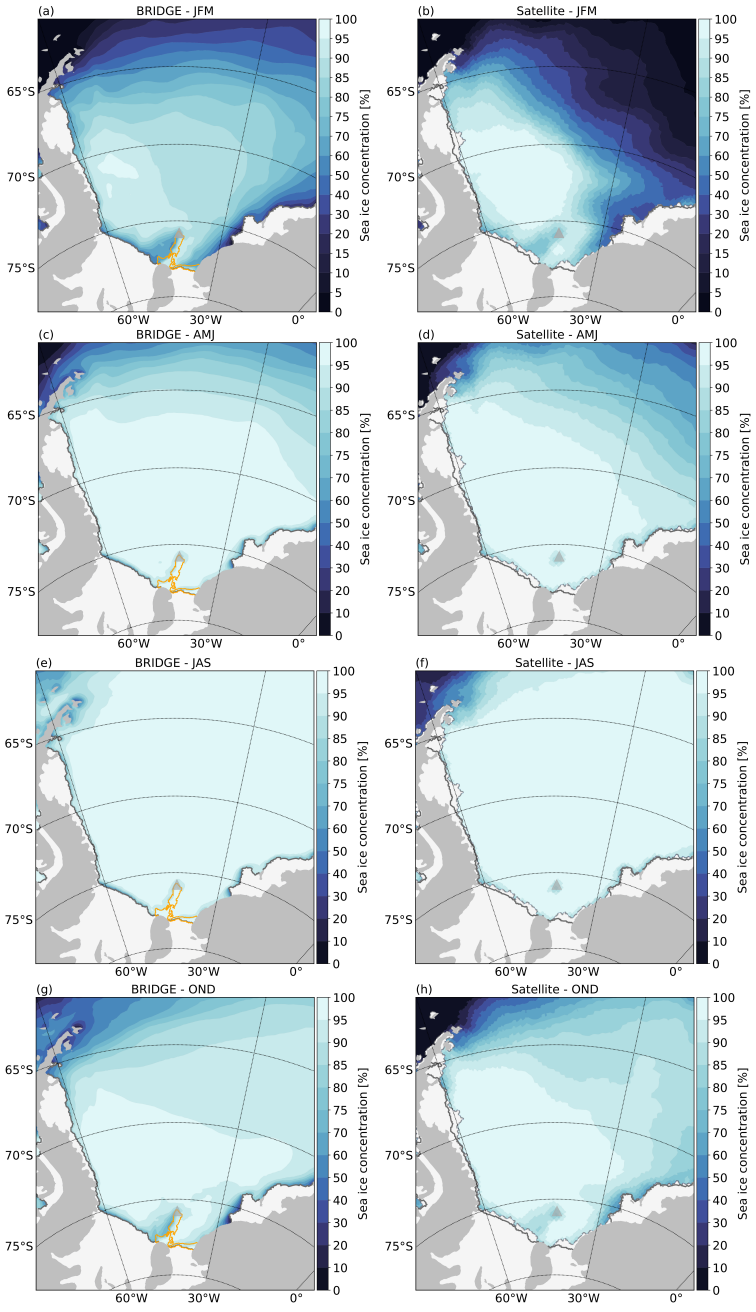

Figure 3.1: (a) Seasonal mean (2002–2017) sea ice concentration over the Weddell Sea from BRIDGE (a,c,e,g) and satellite data (Peng et al. 2013)(b,d,f,h). The 50% fast-ice occurrence contour is shown in orange in panels (a,c,e,g). The solid gray line in all panels and the dashed gray line in panels (b,d,f,h) contour the ice shelf edge from the model and the data, respectively. The location of the grounded iceberg A23-A (2002–2017) is marked by a triangle.

In the Weddell Sea, sea ice cover exhibits a prominent seasonal cycle (Parkinson 2019). The ice covered area reaches a minimum typically in February when it is limited to the southwestern Weddell Sea. In September, the sea ice covers the whole Weddell Sea and ice area reaches its maximum.

Simulated sea ice concentration (2002–2017) (Fig. 3.1) follows the seasonal pattern: high ice concentrations (>70%) are limited to the southwestern Weddell Sea in summer (JFM), while in winter (SON) they extend over the whole basin. In summer, substantially lower ice concentrations are found along coastlines and ice-shelf edge in the southern Weddell Sea, as well as west of the ice bridge forming between the FRIS and grounded iceberg A23-A. This pattern is prominent in the satellite data as well (Fig. 3.1b,f). In narrow belts along the ice fronts and ice bridge, sea ice concentrations in BRIDGE are lower than in the surrounding pack ice for April–September (AMJ and JAS)(Fig. 3.1,c–f). These regions are known as locations with the frequent development of coastal polynyas (Nihashi & Ohshima 2015*b*, Paul et al. 2015). While the resolution of sea ice concentration data (25 km) is not sufficient to resolve all the details of narrow polynyas, low sea ice concentrations can still be noticed throughout the year along the ice-shelf edge and ice bridge. Furthermore, the persistent low sea ice concentrations in the satellite data can be found in proximity of the grounded iceberg A23-A. The regional distribution and occurrence of coastal polynyas in the BRIDGE experiment are the main topics in section 3.3.

The simulated sea ice edge in summer is in a good agreement with the observations for the western part of the basin, while in the eastern part, the low ice concentrations extend further north compared to observations. In winter, sea ice extends up to 2° more northward than in the observations. The seasonal cycle of sea ice extent (area with sea ice concentration >15%) for the Weddell Sea from the BRIDGE experiment and satellite observations (2002–2017) are shown in Fig. 3.2. The model overall overestimates sea ice extent (area with sea ice concentration >15%) compared to observations, however, it captures well the range and seasonality in the sea ice extent. While the onset of the freezing season, the growth of the ice extent, and the timing of sea ice maximum match the observations, the sea ice minimum in reached one month later than in observations. The simulated minimum sea ice extent in March (2.46 km^2) is slightly smaller than the extent in February (2.56 km^2), and 32% larger than in the satellite data. The maximum in September is 7.56 km^2, 16% larger than in the satellite data. In general, the

Antarctic sea ice extent is a result of interactions between various factors, such as wind stress, atmospheric thermodynamic conditions, sea surface and sub-surface temperatures, and state of sea ice from the previous summer, while the ACC acts as a northern boundary of sea ice expansion, as surface temperature even in winter is higher than the seawater freezing point. Comparison of sea ice extent in BRIDGE and FESOM simulations with the different atmospheric forcing (ERA instead of CCLM, cATMO) and without the representation of the icescape (noBRIDGE) (see section 2.1.4 for more detail on different simulations) (Fig. 3.2), suggests that atmospheric forcing in the cATMO experiment helps to reduce the sea ice extent bias in summer. The winter bias is, however, very similar between the experiments. The reduced summer sea ice extent in cATMO (using ERA as the forcing), can be attributed to the warmer temperatures over the offshore Weddell Sea in ERA when compared to CCLM (more details in section 2.2). CCLM forcing used in the BRIDGE and noBRIDGE experiments improves the representation of atmospheric fields over the southern Weddell Sea continental shelf Zentek & Heinemann (2020) crucial for a realistic simulation of the surface freshwater flux. Moreover, the warm temperature bias in ERA has been reported in several other studies and is found to be the consequence of the missing snow layer in the ERA sea ice parameterization Batrak & Müller (2019), Heinemann et al. (2022). However, the standard tuning of FESOM parameterizations has been accomplished using ERA as the atmospheric forcing. The sea ice extent results indicate that FESOM parameter calibration better compensates for the forcing bias in summer for the cATMO experiment. The sensitivity to atmospheric forcing and consequences for the simulated surface freshwater flux are topic of Chapter 4. The choice of parameters in the sea-ice model parameterizations and the consequences for the simulated sea state will be explored further in Chapter 5.

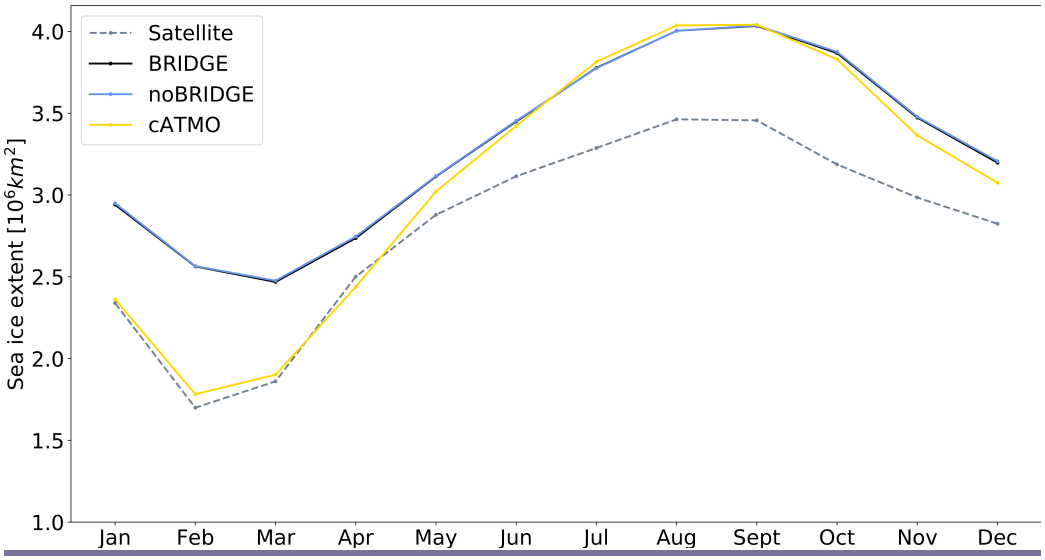

Figure 3.2: Monthly mean sea ice extent (2002–2017) for the Weddell Sea (between 60°W and 20°W) from the FESOM experiments and satellite data (Peng et al. 2013).

3.2 Surface freshwater flux

In the Weddell Sea, there is a clear separation between the negative and positive net surface freshwater flux regions, corresponding to areas where sea ice growth dominates melt and vice versa. Corresponding to freshwater removal by sea ice growth, a negative flux with values between -2 m a^{-1} and -1 m a^{-1} is found over most of the continental shelf (Fig. 3.3,a) In front of the Filchner Ice Shelf and in the region west of the ice mélange, surface freshwater flux reaches -5 m a^{-1}, while in a narrow band adjacent to the Ronne and Brunt ice shelves, it reaches -12 m a^{-1}. These are also the locations with the highest occurrence of polynyas, defined here as nodes with simulated ice growth for which ice concentration is smaller than 70% or ice thickness smaller than 20 cm. Given that the strong ocean-to-atmosphere heat fluxes in polynyas occur both over the open ocean and thin ice areas, these criteria have been widely used in other studies (e.g. Haid & Timmermann (2013), Haid et al. (2015) or Nihashi & Ohshima (2015*b*), Paul et al. (2015)). The geographical pattern of polynyas (Fig. 3.4,b) is overall similar to the one from Paul et al. (2015) (Fig. 3.4,a) and includes major polynyas detected in other satellite-based studies (e.g. Drucker et al. (2011), Nihashi & Ohshima (2015*b*)). The details of sea ice production within polynyas will be discussed in section 3.3. In the seasonally ice-covered zone, the positive freshwater

flux related to the sea ice melt is the strongest along the sea ice margins (up to 1.5 $\mathrm{m\,a^{-1}}$, not shown). Patterns of positive freshwater flux (up to 2 $\mathrm{m\,a^{-1}}$) can also be found at the continental shelf break, where the vertical entrainment of Warm Deep Water into the surface mixed layer drives melting at the sea ice base. Paul et al. (2015) noted the high occurrence of thin ice in this region, as one of the few regions where thin ice was detected out of the coastal polynyas.

Under the ice shelves, positive freshwater flux is due to basal melt, and negative due to freezing at the ice shelf base. The overall pattern of the basal melt under FRIS is similar to the satellite data (Rignot et al. 2013, Moholdt et al. 2014, Adusumilli et al. 2020). The freshwater input is strongest near the grounding lines (up to 3 $\mathrm{m\,a^{-1}}$), and more moderate at the ice fronts (Fig. 3.3,a). Moderate freezing (-1 $\mathrm{m\,a^{-1}}$) is found at the Ronne Ice Shelf center and along its western edge, as well as on the eastern side of Berkner Island and under the northeast Filchner Ice Shelf. The eastern edge of the Filchner Ice Shelf is dominated by basal melt similar as in Rignot et al. (2013). In the southern Filchner cavity, a band of basal melt rates reaching 2 $\mathrm{m\,a^{-1}}$ is found, which is missing in the satellite-based estimates (Rignot et al. 2013). Data from repeated radar measurements (Zeising et al. 2021) shows indeed locally enhanced basal melt in this region, albeit with a weaker amplitude (1.13 $\mathrm{m\,a^{-1}}$) than in BRIDGE. Compared to Adusumilli et al. (2020), a stronger melt and weaker freezing signal is found in BRIDGE in the northeast Filchner cavity. The difference could result from the too strong HSSW inflow in the Filchner cavity in BRIDGE. The strength of the melting and freezing maxima in BRIDGE is weaker than in the satellite-based estimates from Moholdt et al. (2014). The absence of tides in our model could be a possible explanation for this difference, as they enhance both the basal melt and refreezing due to the increased mixing (Hausmann et al. 2020). However, changes in the basal melt related to changes in the surface freshwater flux on the continental shelf are primarily density driven (Nicholls & Østerhus 2004, Hattermann et al. 2021). Therefore, the lack of tides in our model does not affect the conclusions of this study.

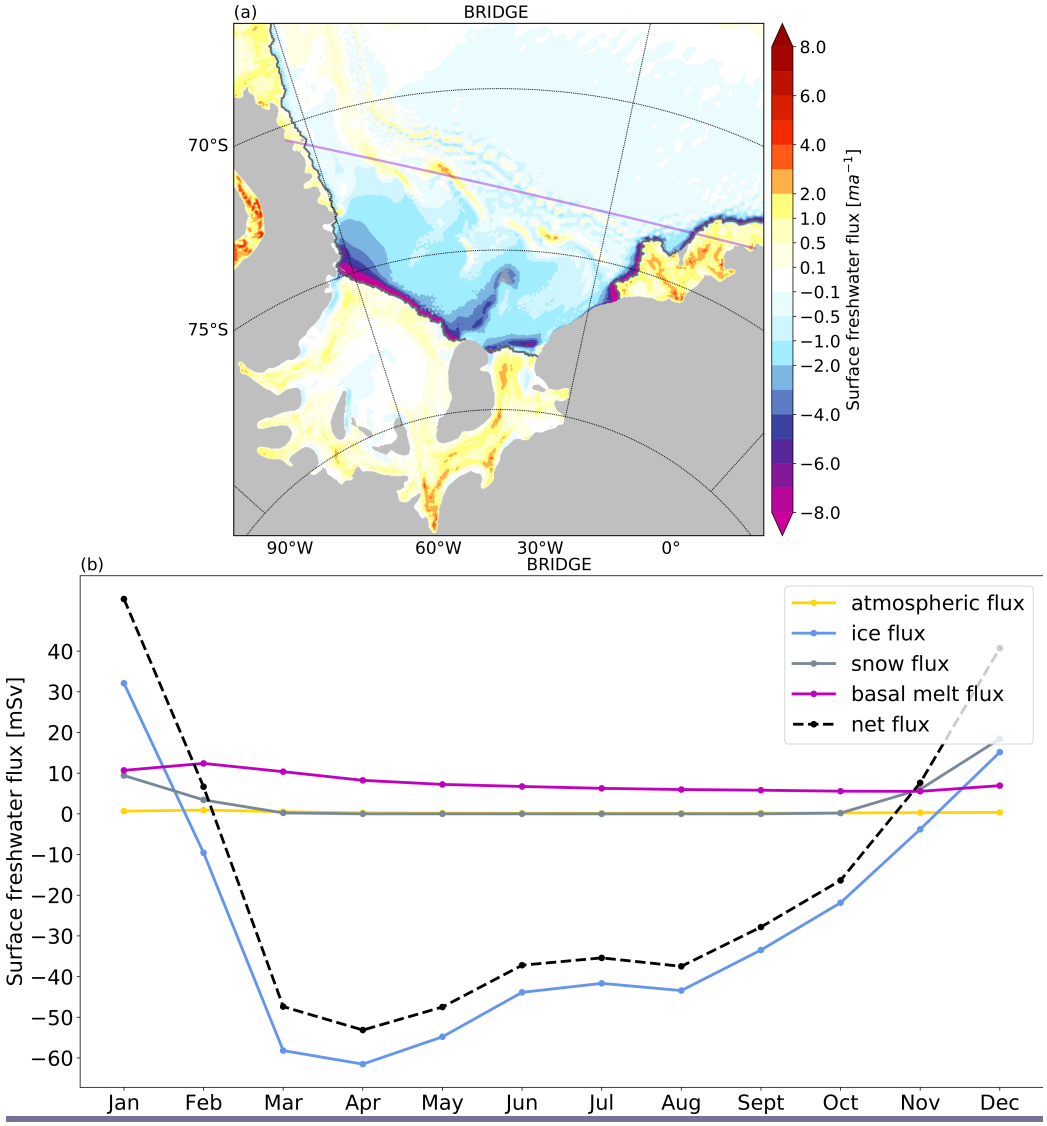

Figure 3.3: a) Annual mean net surface freshwater flux (2002–2017) from BRIDGE, with positive values corresponding to a flux in the ocean. Southern Weddell Sea control region is enclosed by the violet line. Note that the colormap does not linearly scale with the data. The location of the grounded iceberg A23-A (2002–2017) is marked by a triangle. b) Monthly mean surface freshwater fluxes (2002–2017) from BRIDGE for the southern Weddell Sea control region.

The seasonal evolution of the net surface freshwater flux and its components for the continental shelf of the southern Weddell Sea is shown in Fig. 3.3,b. The seasonal cycle of the net freshwater flux (2002–2017) is dominated by ice growth and melt fluxes: it is negative in March–October due to the effect of sea ice production, and positive in November–February due to the effect of the combined ice and snow melt. The annual mean net flux is -16.3 mSv (1 mSv=1000 $m^3 s^{-1}$), as the extraction of freshwater due to

ice production (-27.1 mSv) dominates the sum of fluxes. $P - E$ provides a mean freshwater input of 0.3 mSv and snow melt contributes 3.1 mSv. The ice shelf basal melt flux provides another 7.6 mSv, out of which 5.2 mSv originate from FRIS. Converted to a mass flux using ice density of 910 $\mathrm{kg\,m^{-3}}$, the FRIS basal melt corresponds to 150.9 $\mathrm{Gt\,a^{-1}}$, which falls in the range of the satellite-based estimates from Moholdt et al. (2014) (58 – 190 $\mathrm{Gt\,a^{-1}}$), Rignot et al. (2013) (110 – 200 $\mathrm{Gt\,a^{-1}}$), and Adusumilli et al. (2020) (81.4±122.9 $\mathrm{Gt\,a^{-1}}$).

The melting of icebergs can be another source of freshwater, however, this flux is not included in the simulation. Based on the iceberg melt climatology from Rackow et al. (2017), magnitudes of the iceberg melt rates on the southern Weddell Sea continental shelf are comparably low (around 0.3 $\mathrm{m\,a^{-1}}$) compared to the magnitudes of the sea ice fluxes. Freshwater flux from the iceberg melt, therefore, would have a relatively small impact on the surface freshwater flux in the region when compared to the dominant sea ice fluxes.

The sea ice export out of the southern Weddell Sea is the main reason for the imbalance between the ice production and melt fluxes. On average (2002–2017), 1509 $\mathrm{km^3\,a^{-1}}$ of ice is produced on the southern Weddell Sea continental shelf in BRIDGE. With the net sea ice export of 1041 $\mathrm{km^3\,a^{-1}}$, 70% of the produced ice is exported from the region. The mean net sea ice export across the 69.5°S latitude band (2002–2017) in BRIDGE is 1567 $\mathrm{km^3\,a^{-1}}$ (38 mSv). Across the same latitude, Haumann et al. (2016) estimated long-term annual freshwater flux due to the northward sea ice transport in the Weddell Sea sector to be 50±20 mSv. Based on passive microwave data, Drucker et al. (2011) calculated the net export of sea ice area out of the southern Weddell Sea (April–October 2003–2008) and found it to be 5.2×10^5 $\mathrm{km^2\,a^{-1}}$. The net sea ice area export, across approximately the same gates and for the same time, in BRIDGE is 5.1×10^5 $\mathrm{km^2\,a^{-1}}$, quite close to the observed estimates, with a corresponding net sea ice volume export of 814 $\mathrm{km^3\,a^{-1}}$.

3.3 Sea ice production

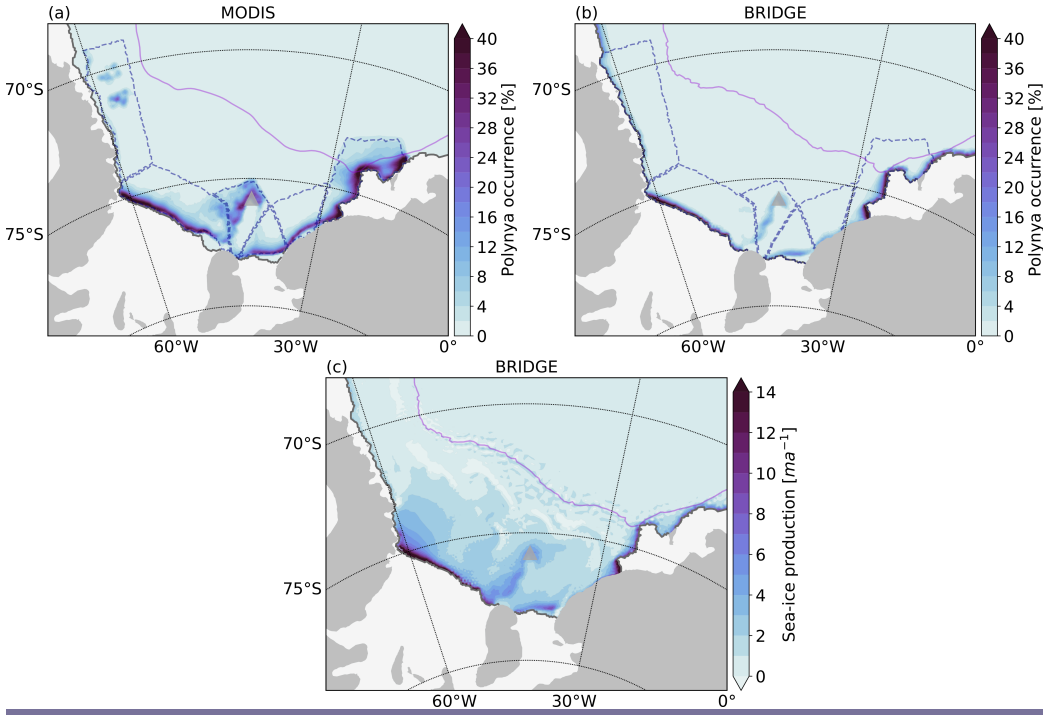

Figure 3.4: a) Polynya occurrence (April–September, 2002–2014) from MODIS data (Paul et al. 2015) calculated as percentage of days with ice thickness <20 cm (data is shown on the FESOM grid). b) Polynya occurence in BRIDGE (April–September, 2002–2014) calculated as a percentage of days with sea ice production occurring at nodes with ice concentration <70% or ice thickness <20 cm. c) Mean sea ice growth rates (2002–2017) from BRIDGE. The location of the grounded iceberg A23-A (2002–2017) is marked by a triangle and the 2500 m isobath is indicated by violet contour in all panels. The six sub-regions for comparison of polynya ice-production from Paul et al. (2015)) in (a) and adapted to the FESOM landmask in (b) are enclosed by dashed dark blue lines. They are from west to east: Antarctic Peninsula (AP), Ronne Ice Shelf (RO), the area around the ice mélange (IB), Filchner Ice Shelf (FI), Coats Land (CL), and Brunt Ice Shelf (BR). Note that in (a), thin ice signal in AP is associated to the icebergs that were present in the region (Paul et al. 2015).

The pattern of the negative surface freshwater flux in BRIDGE (Fig. 3.3,a) corresponds to the pattern of the annual mean sea ice production in Fig. 3.4,c. A belt of elevated sea ice production rates is found in the coastal polynyas along the ice-shelf fronts and coastlines, with the maximum values up to 15 m a^{-1} in the corner between the Antarctic Peninsula and the Ronne Ice Shelf, and west of the Brunt Ice Shelf. Strong sea ice production rates also occur west of the ice mélange associated with the grounded iceberg A23-A.

To estimate the role of polynyas in the surface freshwater flux of the southern Weddell Sea, I calculate cumulative annual ice production both within and outside polynyas from the daily model output (only positive growth rates are considered). The sea ice production occurring at the nodes where the sea ice concentration is smaller than 70% or thickness is smaller than 20 cm is counted as polynya-based ice production. Although such-defined polynyas cover only 2% of the southern Weddell Sea area, their higher average ice-growth rate (24 $\mathrm{m\,a^{-1}}$) compared to outside polynyas (4 $\mathrm{m\,a^{-1}}$) significantly contributes to the total ice production in the region.

For 2002–2017, 17% (260 $\mathrm{km^3\,a^{-1}}$) of the ice produced on the continental shelf of the southern Weddell Sea (1509 $\mathrm{km^3\,a^{-1}}$) comes from polynyas in BRIDGE. To investigate the regional distribution and compare the simulated polynya ice production with other studies, I divided the continental shelf into six sub-regions (Fig. 3.4,b) adapted from Paul et al. (2015) (Fig. 3.4,a) by extending them to the coastline in the model. The largest annual ice production in BRIDGE is found in the Ronne (RO, 123 $\mathrm{km^3\,a^{-1}}$) and Brunt (BR, 79 $\mathrm{km^3\,a^{-1}}$) ice shelves regions. At the same time, significant ice production can also be found in the region associated with the ice bridge (IB, 20 $\mathrm{km^3\,a^{-1}}$) and in front of the Filchner Ice Shelf (FI, 27 $\mathrm{km^3\,a^{-1}}$).

Comparing different estimates of the ice production within polynyas is difficult, as different methods (i.e. heat flux parameterizations and atmospheric forcing, treatment of fast ice), and differences in regional and seasonal coverage lead to a large spread between the studies. Since ice production in polynyas exhibits a large interannual variability and depends on the length of the season taken into account, I aim to match the sampling periods and areas from the other studies in the best possible way (Table 3.1). Drucker et al. (2011) report mean ice production of 99 $\mathrm{km^3\,a^{-1}}$ for the Ronne, and 112 $\mathrm{km^3\,a^{-1}}$ for the Brunt region (April–October 2003–2008). The corresponding values for similar regions from BRIDGE are smaller, and the Ronne (RO) ice production (85 $\mathrm{km^3\,a^{-1}}$) in our case is higher than the Brunt (BR) ice production (51 $\mathrm{km^3\,a^{-1}}$). They also report significant ice production (30 $\mathrm{km^3\,a^{-1}}$) in polynyas associated with the grounded iceberg A23-A. For the corresponding period, 18 $\mathrm{km^3\,a^{-1}}$ of ice is produced in polynyas forming west of the ice mélange between Berkner Island and A23-A in BRIDGE. For March–October 2003–2007, Nihashi & Ohshima (2015*b*) report 42 $\mathrm{km^3\,a^{-1}}$ of ice produced in the Ronne polynya. For the same period, and similar area (RO), we find polynya ice production in BRIDGE to be much larger,

87 $km^3\,a^{-1}$. In the narrow region along the Ronne Ice Shelf, where the ice growth rates in the model are particularly high, Nihashi & Ohshima (2015*b*) detected fast ice, not polynyas. They found that discrimination of fast-ice from the polynya areas in the satellite data reduces the sea ice production estimates. Based on the coarser data without the fast-ice mask, Tamura & Ohshima (2011) reported ice production of 71 $km^3\,a^{-1}$ for the Ronne region (for the corresponding period), which is much closer to our results. As the fast ice from this region is not included in our model, this likely contributes to the discrepancy between our results and Nihashi & Ohshima (2015*b*).

The most detailed estimates of the regional polynya ice production are found in Paul et al. (2015) (April–September 2002–2014). The regional distribution of the ice production in BRIDGE is very similar to the one found by Paul et al. (2015) (Table 3.1). Their estimates for RO (29 $km^3\,a^{-1}$), BR (30 $km^3\,a^{-1}$), and FI (9 $km^3\,a^{-1}$) are smaller than the corresponding results from BRIDGE (75 $km^3\,a^{-1}$, 47 $km^3\,a^{-1}$, and 14 $km^3\,a^{-1}$ respectively), while there is a good agreement with simulated ice production for another significant polynya ice production region, IB (11 $km^3\,a^{-1}$ compared to 15 $km^3\,a^{-1}$ in BRIDGE). The data from Paul et al. (2015) incorporates a different landmask than in our model, with differences being the largest for RO and FI. Integrating results from BRIDGE over the same area as in Paul et al. (2015) yields 52 $km^3\,a^{-1}$ for RO and 9 $km^3\,a^{-1}$ for FI. It should be noted that the warm bias of the ERA data used in the MODIS retrieval tends to reduce polynya area and ice production, possibly explaining the smaller values in Paul et al. (2015). Furthermore, we find that on average only 64% (167 $km^3\,a^{-1}$ out of 260 $km^3\,a^{-1}$) of ice in the southern Weddell Sea polynyas is being produced over the season covered by the satellite data (April–September), meaning that a non-negligible ice production is not covered by the satellite-based estimates.

In an earlier FESOM study, Haid & Timmermann (2013) found the contribution from Ronne to be 42 $km^3\,a^{-1}$, from Brunt 11 $km^3\,a^{-1}$, and 19 $km^3\,a^{-1}$ from the Antarctic Peninsula region (May–September, 2002–2009). We find 86 $km^3\,a^{-1}$ for Ronne (RO), 50 $km^3\,a^{-1}$ for Brunt (BR), and ice production of only 8 $km^3\,a^{-1}$ in the Antarctic Peninsula region (AP) for the corresponding period. Furthermore, the grounded iceberg A23-A and the associated ice bridge were not represented in Haid & Timmermann (2013), where we find non-negligible polynya ice production of 18 $km^3\,a^{-1}$ for 2002–2009. Except for the representation of the ice bridge, the differences between our stud-

ies are likely further influenced by the different atmospheric forcing used in Haid & Timmermann (2013). However, the two model configurations also differ in other aspects (e.g. the representation of the ice shelf, topography, resolution).

Overall, the regional pattern of polynya ice production is well represented in BRIDGE when compared to the satellite-based studies, with the largest contributions from the Ronne (RO) and Brunt (BR) polynyas, followed by Filchner (FI) polynya and polynyas associated to the ice bridge (IB). The strength of ice production in BRIDGE falls in the range of estimates from the satellite-based studies, albeit on the higher side. Differences in the landmasks and representation of the fast ice are the likely reason for some of these differences.

Study	RO	IB	BR
Drucker et al. (2011)	99 (85)	30 (18)	112 (51)
Nihashi & Ohshima (2015*b*) based on Tamura & Ohshima (2011)	71 (87)	– (17)	– (50)
Nihashi & Ohshima (2015*b*)	42 (87)	– (17)	– (50)
Paul et al. (2015)	29 (52)	11 (14)	30 (45)
Haid & Timmermann (2013)	41 (86)	– (14)	11 (50)

Table 3.1: Summary of cumulative polynya based ice-production [km^3] for the freezing season from various studies, with the corresponding values from BRIDGE in parenthesis.

3.4 Hydrography

> What's cooler than being cool? Brine-cold.
>
> Douglas Main

The brine rejected in the process of sea ice production leads to the densification of the near-surface waters on the continental shelf, resulting in the formation of HSSW (about -1.9 to -1.5°C, S > 34.6 psu) that dominates the southern Weddell Sea continental shelf (Nicholls et al. 2009, Janout et al. 2021). The fraction of HSSW that flows into the FRIS cavity is modified by the interaction with the ice shelf meltwater, forming ISW with temperatures below seawater surface freezing temperatures (<-1.9°C). These cold dense watermasses limit the inflow of warmer mWDW that seasonally reaches the continental shelf (Ryan et al. 2020) towards FRIS.

The historical observations (2.3.3) in the region are sparse and uncertain due to the large interannual variability. Only a few expeditions managed to collect temperature and salinity data across both eastern and western parts of the continental shelf (Janout et al. 2021). I compare the representation of watermasses against the historical temperature and salinity observations in the key regions on the southern Weddell Sea continental shelf. Since most of the hydrographic measurements have been collected in austral summer (JF), the mean (2002–2017) model values for the corresponding season are shown in Fig. 3.5. Overall, the simulated thermohaline features are similar to historical observations. HSSW dominates the hydrographic conditions on the continental shelf, with presence of ISW and mWDW inflow. The most dense watermasses can be found at the deepest parts of the southern Weddell Sea continental shelf both in the observations and in the model (Fig. 3.5a and b). The observed HSSW with the highest density, originating from the depths of Ronne Depression (Nicholls & Østerhus 2004, Janout et al. 2021), has salinities up to 34.9 psu (Fig. 3.5c). Simulated maximum salinities of Ronne (RO) originating HSSW are up to 0.1 psu higher (Fig. 3.5c). However, the corner between the Ronne Ice Shelf front and the Antarctic Peninsula where salinity is the highest in the model (Fig. 3.6) is not well covered with the observations (Fig. 3.5c, inset). The coldest observed ISW (temperatures <-2.2 °C) fills the Filchner Through (depths >1000m) and dominates the Filchner region (Fig. 3.5a and d). In the model, however, the Filchner region is dominated by the locally produced HSSW (Fig. 3.5d). Janout et al. (2021) found that conditions in the Filchner Trough vary interannaully between being dominated by Ronne HSSW-derived ISW (Ronne-mode) or locally derived Berkner-HSSW (Berkner-mode). For 2002–2017, the Filchner region in the model is more strongly influenced by the locally (Berkner) produced HSSW than Ronne originating ISW.

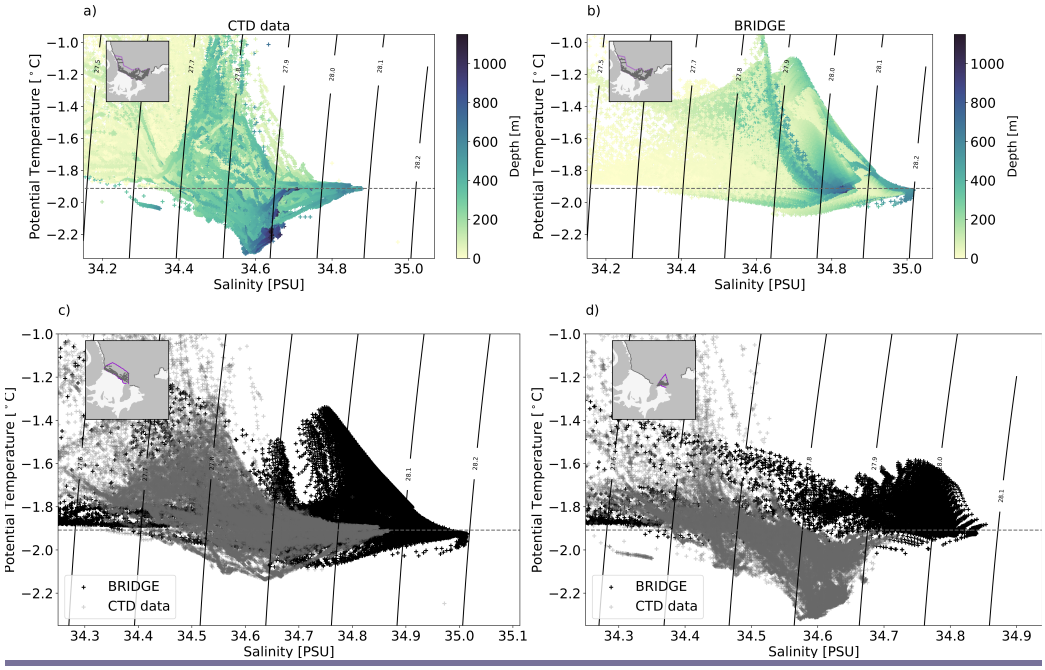

Figure 3.5: Temperature-salinity diagrams for the southern Weddell Sea continental shelf (south of the 1500 m isobath) from (a) the historical CTD measurements and (b) the BRIDGE experiment (2002–2017), and temperature-salinity diagrams from the historical CTD measurements and BRIDGE (2002–2017) for (c) the Ronne (RO), and (d) the Filchner (FI) regions. Maps in the insets (a–d) show corresponding regions and locations of the CTD data. Potential density ((1000-σ)kgm^{-3}) contours are shown in black lines and dashed gray line indicates the seawater freezing temperature.

With temperatures near the freezing point, the density of HSSW depends primarily on the salt content. The signature of the HSSW can be found in the simulated mean bottom salinity and field (2002–2017) along the southern Weddell Sea continental shelf, with the salinity increasing from the eastern to the western end of the shelf (Fig. 3.6). The salinity maximum in BRIDGE corresponds to the main observed HSSW production site (Nicholls et al. 2009), at the corner between the front of the Ronne Ice Shelf and the Antarctic Peninsula (around 35 psu). Another maximum is found north of the ice bridge/grounded iceberg (around 34.9 psu). The mean bottom salinities at the Ronne ice front (34.85 – 35 psu) are higher than in the CTD measurements from austral summer 2018 (around 34.8 psu; Janout et al. (2021)). Similarly, the salinity at the Filchner ice front (34.75 – 34.85 psu) is higher than in the latest observations (around 34.6 psu; Janout et al. (2021)). The simulated mean summer values are a bit smaller (34.85 – 34.9 psu) and closer to the observations at the Ronne ice front, while those at the Filchner

ice front are still by 0.1 – 0.15 psu saltier than the observations. In the summer 2018, the Filchner ice front was dominated by Ice Shelf Water (ISW) originating from the Ronne-sourced HSSW and modified in the interaction with the ice-shelf base, which leads to smaller bottom salinities than in the presence of the more locally produced Berkner-sourced HSSW found at the Filchner ice front in, e.g., 2017 (bottom salinities 34.70 – 34.75 psu) (Janout et al. 2021). With salinities in Filchner Trough being higher than in the observations, the model results indicate prevalence of the locally produced HSSW on the Filchner ice front 2002–2017.

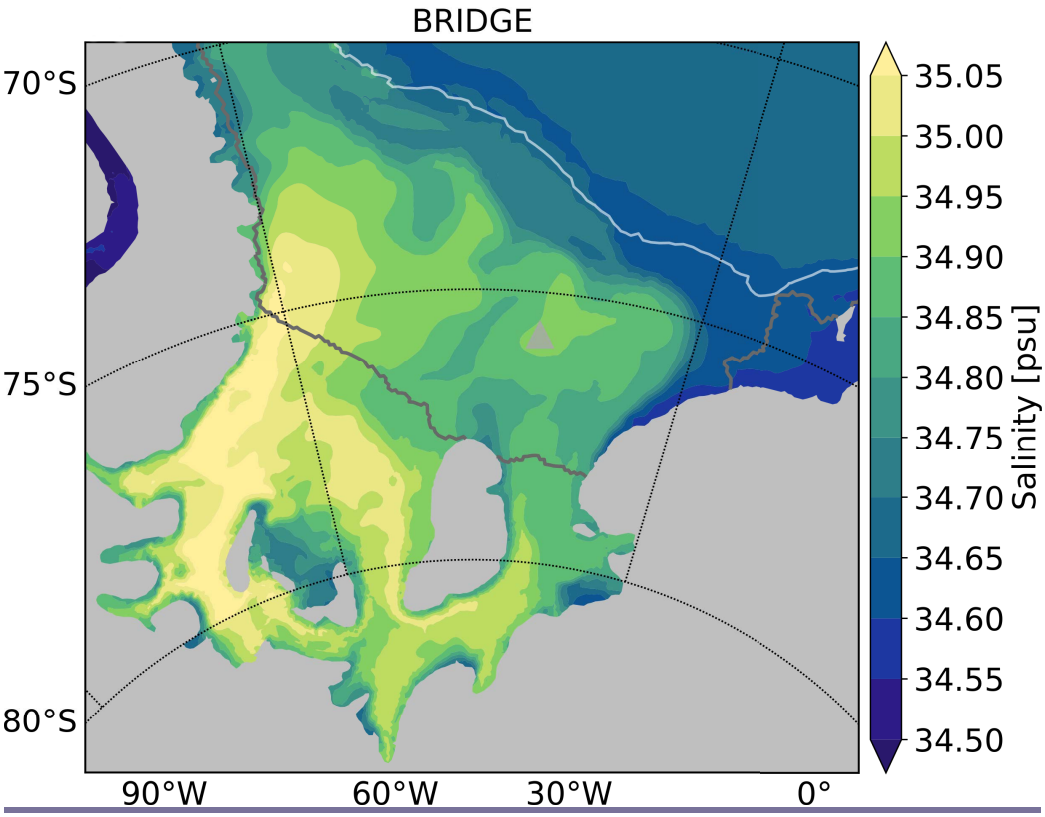

Figure 3.6: Mean (2002–2017) bottom salinity in BRIDGE. The ice shelf edge is indicated by a gray contour, and the 2500 m isobath is marked by a white contour. The location of the grounded iceberg A23-A (2002–2017) is marked by a triangle.

3.5 Summary of the Chapter

To gain confidence in the model's ability to represent realistically the surface freshwater flux in the southern Weddell Sea, I compared results from the reference experiment (BRIDGE) to observations and observation-based estimates.

Simulated sea ice concentration follows the observed seasonal pattern with high ice concentrations limited to the southwestern Weddell Sea in summer, and extending over the whole basin in winter. The model overall overestimates sea ice extent compared to observations, however, it captures well the range and seasonality in the sea ice extent. The low ice concentrations are found in locations of coastal polynyas along coastlines and ice-shelf edges, and west of the ice bridge forming between FRIS and grounded iceberg A23-A.

The model represents reasonably well the surface freshwater flux components and variability when compared to observation-based estimates. The flux in the region is dominated by the extraction of freshwater due to sea ice production, which is strongest in the coastal polynyas. It is found that 70 % of the ice produced on the continental shelf of the southern Weddell Sea is exported from the region. While coastal polynyas cover 2 % of the continental shelf area, sea ice production within the coastal polynyas accounts for 17 % of the overall annual sea ice production (1509 km^3). The largest contributions come from the Ronne Ice Shelf and Brunt Ice Shelf polynyas and polynyas associated with the ice bridge. The simulated distribution of watermasses on the continental shelf is similar to observations. Furthermore, the main observed HSSW production sites are well represented in the model. While being saltier than the observations, model results indicate prevalence of the locally produced HSSW on the Filchner ice front 2002–2017.

The impact of the atmospheric forcing and representation of the icescape on the surface freshwater flux will be in focus of the next chapter.

4. Impact of atmospheric forcing and icescape

In this chapter, I asses the impact of atmospheric forcing and icescape on the southern Weddell Sea surface freshwater flux. I conducted sensitivity experiments using a coarser reanalysis product as atmospheric forcing (cATMO) and an experiment without the representation of the stationary icescape features (noBRIDGE). Both sensitivity experiments were initialized from the same conditions as the reference experiment (BRIDGE) and run for the same period, 2002–2017. Another 3-year simulation was extended from the conditions of the BRIDGE experiment at the end of 2014, with the same setup as BRIDGE except with the fixed fast-ice conditions (statBRIDGE).

Based on these, I investigate changes in sea ice production, the production rate and properties of the HSSW formed on the continental shelf, and the basal melt of FRIS.

4.1 Impact of atmospheric forcing on sea ice production

In an earlier FESOM study, Haid et al. (2015) found the ice production (2007–2009) in the southern Weddell Sea polynyas to be sensitive to the atmospheric forcing, with the ice production increasing with increasing offshore winds. With the higher resolution of the CCLM forcing, topographically influenced winds and heat fluxes in polynyas are better resolved than in the case of ERA (see Heinemann & Zentek (2021)). Here, I examine the influence of the regional and large-scale atmospheric forcing on sea ice production by comparing results of cATMO (forced by ERA) to noBRIDGE (forced by CCLM over the Weddell Sea sector). To ensure consistency with the CCLM boundary conditions and to exclude effects of differences in the large-scale

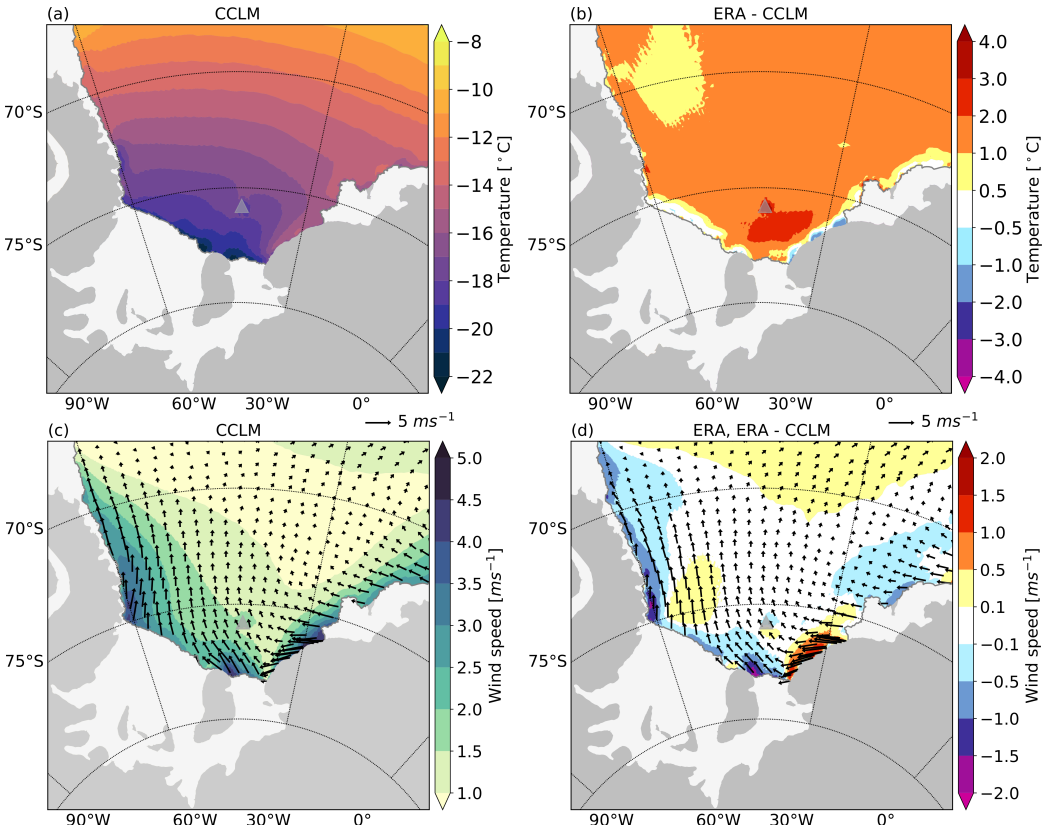

Figure 4.1: (a) Mean air temperature (2002–2017) from CCLM and (b) air temperature difference between ERA-Interim and CCLM. (c) Mean wind field (2002–2017) from CCLM (arrows and color shading) and (d) ERA-Interim (arrows), with wind speed difference between ERA-Interim and CCLM (color shading). Data are shown only over the ocean. The Antarctic continent is drawn in gray; ice shelves are marked in light gray. The location of the grounded iceberg A23-A (2002–2017) is marked by a triangle.

atmospheric influences between the two experiments, ERA was used as a forcing across the entire model domain in cATMO and outside of the Weddell Sea region in the noBRIDGE experiment.

With the higher resolution of the CCLM forcing, katabatic winds and heat fluxes in polynyas are potentially better resolved than in the case of the coarser reanalysis products. CCLM improves the representation of atmospheric features in topographically structured terrain (such as increased katabatic winds) when compared to ERA and has a more realistic thermal structure over coastal polynyas, which are not represented in ERA (Zentek & Heinemann 2020). ERA has 2 °C higher air temperatures over most of the Weddell Sea, while it is 0.5 °C colder in narrow regions along the FRIS calving front and 2 °C cooler along the eastern shelves (Fig. 4.1 b). The

higher temperatures in ERA, when compared to CCLM, are also found in the grounded iceberg A23-A area, as the grounded iceberg is treated as land ice in CCLM, i.e. with a surface temperature colder than for ocean or sea ice. A warm bias of ERA has been found in several other studies and it is caused by the missing snow layer in the ERA sea ice parameterization (Batrak & Müller 2019, Heinemann et al. 2022). Both ERA and CCLM exhibit wind maxima in the southwestern corner between the Antarctic Peninsula and Ronne Ice Shelf, and next to the Brunt Ice Shelf (Fig. 4.1 c and d). The latter is related to katabatic winds from Coats Land, while the former is associated with barrier winds along the Antarctic Peninsula (Heinemann & Zentek 2021). However, another maximum north of Berkner Island is present in the CCLM data, suggesting that the higher horizontal resolution of the CCLM model allows for a more realistic representation of the off-shore winds guided by topography along Berkner Island (see Heinemann & Zentek (2021)). The most pronounced differences between the wind fields are weaker winds over the eastern ice shelves and a stronger maximum off the Ronne Ice Shelf in CCLM (Fig. 4.1 d). Minor differences in the precipitation and evaporation between the two data sets are limited to the outer Weddell Sea (not shown).

As the local offshore winds play a key role in the development of polynyas, the differences in the wind fields between the atmospheric forcings used in noBRIDGE and cATMO are reflected in the ice production fields (Fig. 4.2). The most significant differences in the simulated polynya heat fluxes that determine the ice production are found for the sensible heat flux in locations with the strongest wind differences (not shown). The stronger winds from the Coats Land and along the Brunt Ice Shelf lead to stronger sea ice production rates in cATMO when compared to noBRIDGE. At the same time, in the Ronne corner and surrounding Berkner Island, where offshore winds are weaker in cATMO, sea ice-production rates are reduced.

The mean ice production on the continental shelf in cATMO is smaller (1470 ± 48 km^{3}a^{-1}) than in noBRIDGE (1535 ± 51 km^{3}a^{-1}), and polynyas in cATMO account for 19% of the total ice production. Compared to noBRIDGE, annual polynya ice production in the Ronne region is slightly decreased in cATMO (RO, from to 114 ± 8 km^{3}a^{-1} to 111 ± 7 km^{3}a^{-1}), while the most notable finding is increased polynya ice production for the Brunt region (BR, from 84 ± 4 km^{3}a^{-1} to 94 ± 4 km^{3}a^{-1}). The increase of ice production in cATMO over the eastern shelves (CL and BR) takes ice pro-

duction for those sub-regions (CL an BR) further from the estimates from Paul et al. (2015).

The interannual variability of the cumulative annual sea ice production for the southern Weddell Sea is shown in Fig. 4.4. In both the cATMO and noBRIDGE experiments, sea ice production exhibits large interannual variability. For 2002–2017, we find polynya ice production to be 276±53 km^3a^{-1} in cATMO, and similarly in noBRIDGE, 270±44 km^3a^{-1}. While the regional forcing does not impact significantly interannual variability of sea ice production outside polynyas, it modifies variability within the polynyas. In cATMO, annual polynya ice production and ice production outside polynyas (2002–2017) are highly correlated (r=0.85, p=0.001). In noBRIDGE, this correlation is somewhat weaker (r=0.74, p=0.003), indicating a stronger influence of the local rather than the large-scale forcing on the polynya-based ice production variability. The decreasing trend (2002–2017) in the polynya-based ice production in noBRIDGE (-1.4 km^3a^{-1}) is weaker than in cATMO (-3.3 km^3a^{-1}). However, both experiments show an increase in polynya ice production 2015–2017. This increase has as well been noted by Hattermann et al. (2021) based on the ERA-Interim data, and attributed to the intensification of the southerly winds under the influence of the large scale atmospheric circulation. As ERA is used as the atmospheric forcing in cATMO and as boundary conditions for CCLM that is used as a forcing in noBRIDGE and BRIDGE, these effects of the large-scale atmospheric forcing on sea ice production are also simulated in our experiments.

The multidecadal ice production decrease in the southern Weddell Sea, driven by northerly wind trend, has been reported by Zhou et al. (2023). They found a $> 40\%$ decline in the Ronne and Berkner Bank polynya ice-production rate (1992–2020), possibly driving a 30% reduction of Weddell Sea Bottom Water volume since 1992. Based on the combined results from the long ERA run (1979–2002) and cATMO (2002–2017), we find a decreasing trend of - 6.2 km^3a^{-1} (24 % reduction based on the linear trend estimate) for the total sea ice production (1992–2017) over the corresponding region (RO and IB) and -1.8 km^3a^{-1} (28 % reduction based on the linear trend estimate) for the polynya-only ice production. As the estimate of sea ice formation trend from Zhou et al. (2023) is predominately a function of the sea ice concentration data used for the calculation of the sea ice formation rate, the stronger decreasing trend in their study could be related to the relatively coarse sea ice concentration data (25 km gridded) that does not

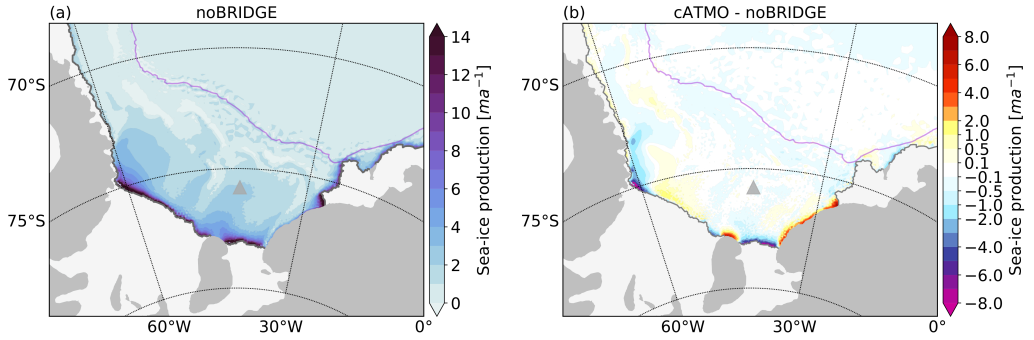

Figure 4.2: (a) Mean sea ice growth rates (2002–2017) from noBRIDGE and (b) difference between cATMO and noBRIDGE. The location of the grounded iceberg A23-A (2002–2017) is marked by a triangle. The 2500 m isobath is indicated by a violet contour. The color map does not linearly scale with the data in (b).

resolve polynyas well.

4.2 Impact of icescape on sea ice production

As described in section 2.3.2 and shown in Fig. 2.5, the variable ice mélange between the coast and iceberg A23-A influences the sea ice distribution. A study investigating the influence of the icebergs grounded north of Berkner Island on sea ice conditions (Markus 1996) reported significant ice concentration increase east of the grounded icebergs (in front of the Filchner Ice Shelf) due to their blocking of the clockwise sea ice drift. To mimic the blocking effect of the ice mélange on the sea ice drift, zero sea ice velocities in the areas identified by the MODIS data were prescribed in BRIDGE (Fig. 4.3 a and c). I investigate the influence of the ice mélange on ice production by comparing the results of noBRIDGE (without the blocking effect) to BRIDGE.

Sea ice velocity and ice thickness from BRIDGE and noBRIDGE for August 2009, when the ice bridge was fully formed (Fig. 2.5 c), are shown in Fig. 4.3 a and b. In BRIDGE, east of the ice bridge, the ice gets thicker compared to noBRIDGE, while thinner ice can be found west of the ice bridge. Due to the shifted polynya development in noBRIDGE, mean (2002–2017) net sea ice growth rates are decreased west of the ice bridge and increased east of it (Fig. 4.3 d). Accumulated ice production decreases most notably north of Berkner Island (IB) (from 20 km^3a^{-1} in BRIDGE to 5 km^3a^{-1} in noBRIDGE) and increases in front of Filchner Ice Shelf (FI) (from 27 km^3a^{-1} to 58 km^3a^{-1}), where much thinner ice is found in noBRIDGE (Table).

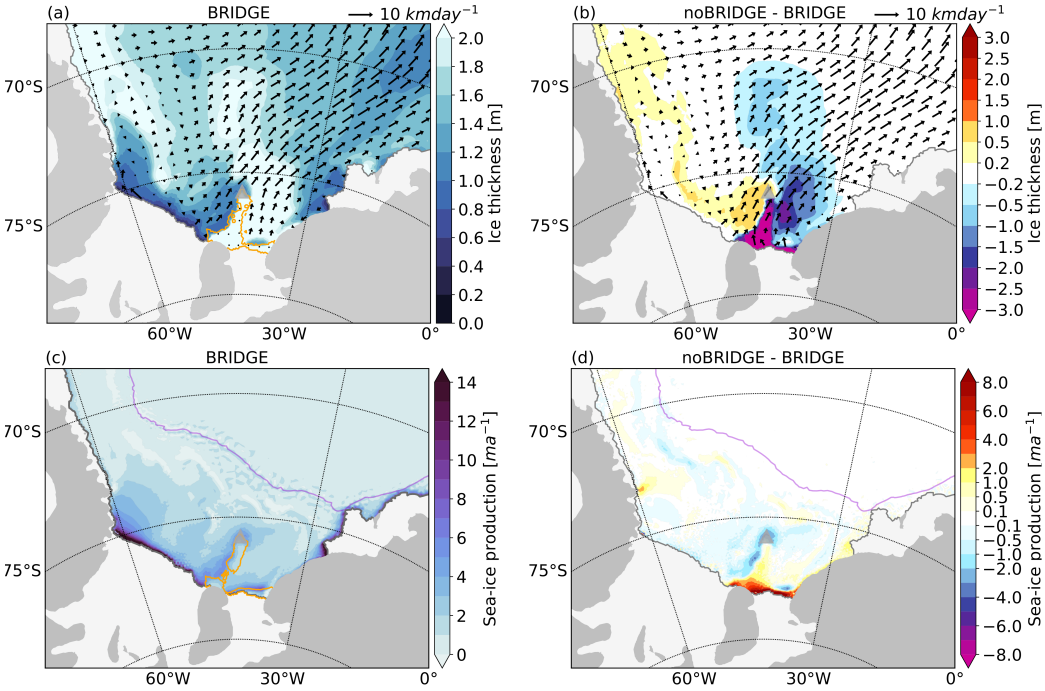

Figure 4.3: (a) Sea ice thickness and velocity from BRIDGE in August 2009, when the ice bridge was fully formed based on the monthly satellite data (Fig. 2.5c) and (b) thickness difference between noBRIDGE and BRIDGE, with the velocity from noBRIDGE in August 2009. (c) Mean sea ice growth rates (2002–2017) from BRIDGE and (d) difference between noBRIDGE and BRIDGE. The location of the grounded iceberg A23-A (2002–2017) is marked by a triangle. The area with 50% fast-ice frequency in (a) and (c) is indicated by an orange contour. The 2500 m isobath is indicated by a violet contour. Note that the color map does not linearly scale with the data in (b) and (d).

Leaving out the impact of the ice bridge on sea ice formation in our simulations, thus, pushes sea ice formation in those regions further from the satellite-based estimates (Paul et al. 2015).

Changes in the icescape also modify the interannual sea ice production variability (Fig. 4.4). The differences between BRIDGE and noBRIDGE are most pronounced in the years when the ice bridge is fully formed, i.e. the fast-ice area is close to its maximum (2002, 2005–2010, Fig. 4.4 d). Reduced ice bridge formation in 2015–2017 leads to a similar increase in sea ice production between the experiments, which can be attributed to the intensification of the southerly winds under the influence of the large-scale atmospheric forcing patterns (Hattermann et al. 2021). As the ice front position and landfast ice are strongly influenced by the offshore winds (Christie et al. 2022), episodic strengthening of southerly winds likely played a role in weakening the ice

bridge.

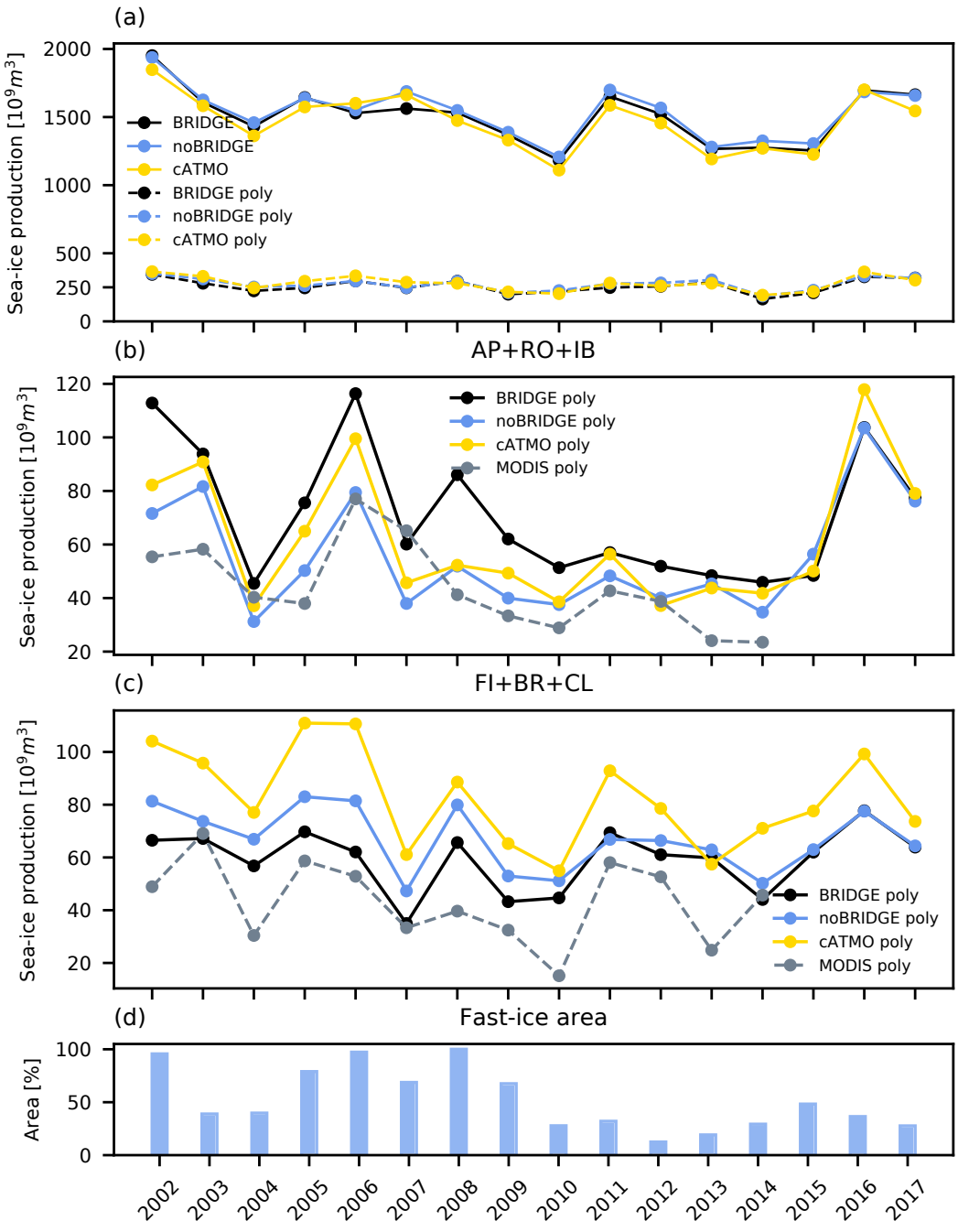

Figure 4.4: (a) Time series of the total and polynya-only annual cumulative ice production (2002–2017) in the southern Weddell Sea from FESOM experiments. (b) Time series of the April–September 2002–2017 polynya ice production from FESOM and the MODIS-based estimates for AP, RO and IB sub-regions from Paul et al. (2015). (c) Time series of the April–September 2002–2017 polynya ice production from FESOM and the MODIS-based estimates for FI, BR and CL sub-regions from Paul et al. (2015). (d) Time series (2002–2017) of the average annual fast-ice area in the BRIDGE experiment (as a percentage of the maximum in 2008).

Method	AP	RO	IB	FI	CL	BR	Sum
BRIDGE	3±2 (7±4)	52±18 (75±23)	15±7 (15±7)	9±6 (14±9)	3±1 (3±1)	45±9 (47±10)	127±31 (161±36)
noBRIDGE	3±2 (7±4)	44±15 (72±21)	2±1 (3±1)	15±5 (39±11)	3±1 (3±1)	48±10 (50±10)	114±26 (173±35)
cATMO	4±2 (10±6)	48±18 (73±25)	4±1 (5±1)	12±4 (28±8)	10±3 (11±3)	60±14 (62±14)	139±37 (189±47)
Paul et al. (2015)	4±3	29±12	11±5	9±7	4±3	30±11	87±26

Table 4.1: Cumulative polynya-based ice production (mean and standard deviation) [km^3] for April-September 2002-2014 from FESOM experiments and Paul et al. (2015), for six sub-regions defined in Paul et al. (2015). Values from the control regions shown in Fig. 2.3 for FESOM experiments are shown in parenthesis.

4.3 HSSW formation

Differences in the mean bottom salinity between the experiments (Fig. 4.5 b,c) correspond to the sea ice production differences (Fig. 4.2 b and 4.3 d).

Corresponding to the location of the weaker sea ice production in cATMO compared to noBRIDGE, fresher water can be found in the Ronne corner and traced along the western edge of the Ronne cavity. North of Berkner Island, salinity in cATMO is slightly increased when compared to noBRIDGE, and saltier waters can as well be found in a narrow band along the eastern ice shelves, following the sea ice production intensification in cATMO.

Without the presence of the ice bridge, saltier waters can be found north and northwest of Berkner Island, while less salty waters can be found north of the grounded iceberg. Among all of the experiments, the least salty waters north of Berkner Island and Filchner Ice Shelf are found in BRIDGE, with values closer to the observations.

The mean production rate of HSSW on the southern Weddell Sea continental shelf was calculated from the net volume flux of HSSW in the region (see Sect. 2.1.5). The annual net flux is calculated from the daily data (2002–2017) over the temperature-salinity classes in the HSSW range (temperature -1.9< θ <-1.5 °C, and salinity S>34.6 psu), with intervals of 0.05 psu for salinity and taking into account only the positive net values (the HSSW volume gain). It should be noted that the export of HSSW to the surrounding ice shelves beside FRIS is assumed to be negligible, while export of HSSW to the Ronne and Filchner cavity, as well as export across the northern bound of the region (Fig. 2.3) are accounted for. The mean production rate (2002–2017) in BRIDGE is 4.9 Sv, and slightly weaker in noBRIDGE (4.8 Sv), the strongest being in cATMO (5.0 Sv). Due to the too high salinity in our experiments, particularly on the eastern side of the continental shelf, our

estimate is likely an upper bound of the HSSW production magnitude. For comparison, Akhoudas et al. (2021) suggested 4.5±0.3 Sv of dense shelf water is produced on the southern Weddell Sea continental shelf (1973–2017), while Nicholls et al. (2009) estimated HSSW production to be 3 Sv. The mean HSSW production on the western continental shelf in BRIDGE is 3.2 Sv, while production rates in noBRIDGE and cATMO are weaker and similar (2.9 and 3.0 Sv). On the eastern shelf, the lowest production rate among the experiments is found in BRIDGE (1.7 Sv). The production rates from the sensitivity experiments without effects of the ice bridge are stronger and increase from noBRIDGE to cATMO (from 1.9 to 2 Sv). These results are consistent with the changes found in the hydrographic observations before and after the grounding of the icebergs in 1986. Changes in the icescape affected the local hydrography and caused the cessation of HSSW formation east of the grounded icebergs (Nøst & Østerhus 1985).

4.4 Sub-ice shelf circulation

HSSW flows into the cavity and impacts the sub-ice shelf circulation. The bottom salinity and velocity (Fig. 4.5 a) reveal the main pathways of the HSSW inflow in the cavity from the western continental shelf: along the western edge of the Ronne cavity through the Ronne Depression, along the western coast of Berkner Island, and then to the rest of the cavity, while HSSW produced on the eastern part of the continental shelf enters the cavity through the Filchner Trough. The velocity of the Ronne-sourced waters (S>34.95 psu) circulating south of Berkner Island and reaching under the Filchner Ice Shelf is intensified in BRIDGE when compared to the other two experiments (Fig. 4.5 b, c). While the inflow of HSSW into the cavity between noBRIDGE and cATMO is rather similar, the pronounced changes are noted in the cavity circulation in BRIDGE. Compared to noBRIDGE, the mean inflow (2002–2017) to Ronne intensifies in BRIDGE (from 0.7 Sv to 0.9 Sv), and the mean inflow to Filchner reduces (from 1.4 Sv to 1.1 Sv). The weaker circulation under the Filchner Ice Shelf in the presence of the grounded icebergs was also reported in a modeling study of the Filchner system (Grosfeld et al. 2001). Since HSSW provides heat supply for the basal melt, the resulting basal melt (Fig. 4.6) of the Filchner Ice Shelf in BRIDGE (66.8 Gta^{-1}) is closer to the satellite-based estimate from Adusumilli et al.

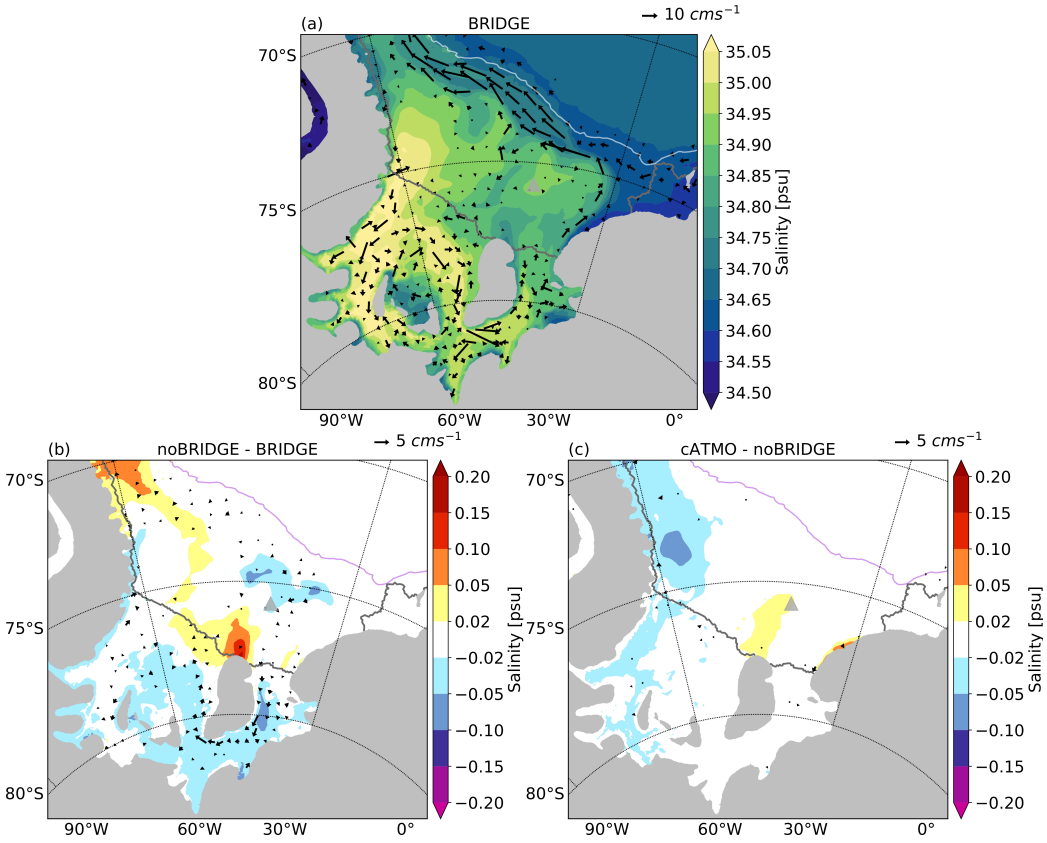

Figure 4.5: (a) Mean (2002–2017) bottom salinity and velocity from BRIDGE. The ice shelf edge is indicated by a gray contour, and the 2500 m isobath is marked by a white contour. Difference (2002–2017) in the mean bottom salinity and velocity between (b) noBRIDGE and BRIDGE and (c) cATMO and noBRIDGE (only mean velocities and velocity differences with magnitudes higher than 1 cms^{-1} are shown). The ice shelf edge is indicated by a gray contour, and the 2500 m isobath is marked by a violet contour. The location of the grounded iceberg A23-A (2002–2017) is marked by a triangle in all panels.

(2020) (34.2±29.6 Gta^{-1}) than noBRIDGE (80.3 Gta^{-1}) as a response to the weaker circulation under the Filchner Ice Shelf in BRIDGE.

Depending on the properties of the water masses in the Filchner cavity, two modes can be observed in the sub-ice shelf circulation variability (Janout et al. 2021): Ronne mode - dominated by the Ronne-sourced waters, or Berkner mode - dominated by the water produced at Berkner Bank. The transition from Berkner to Ronne mode observed from 2017 to 2018 was accompanied by the intensification of the circulation between the Ronne and Filchner cavities (Hattermann et al. 2021). An increase in the density of the water masses was observed in the southern Filchner cavity 2016–2018 due to the intensified propagation of saline Ronne HSSW (Hattermann et al. 2021).

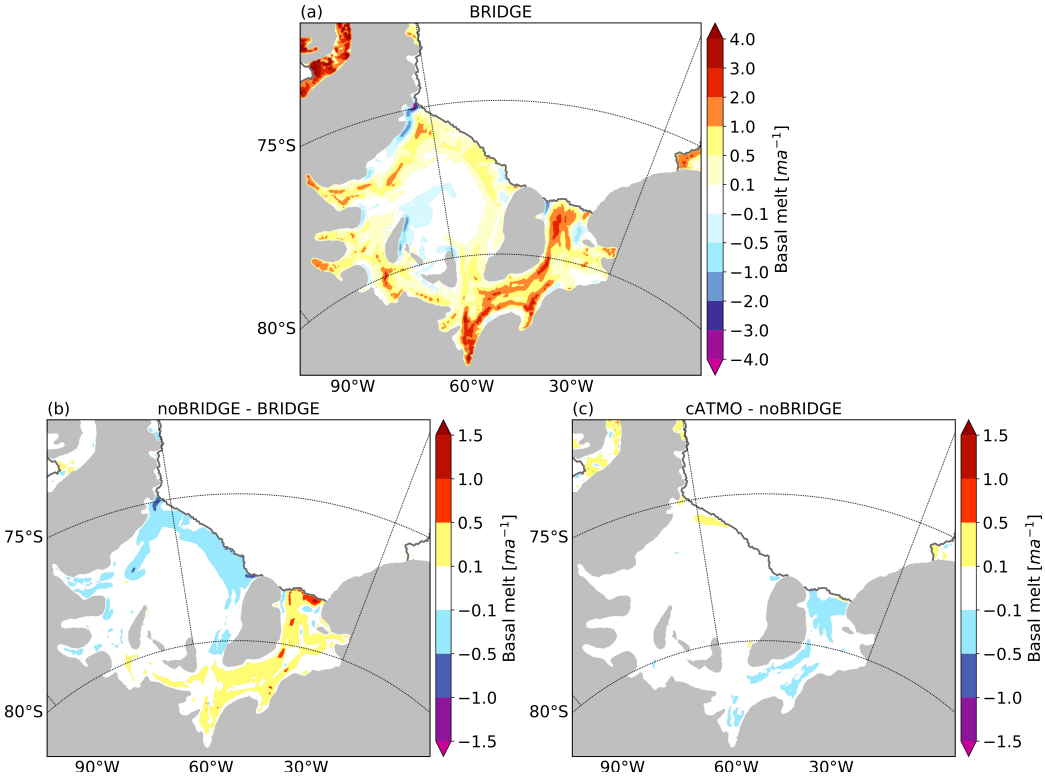

Figure 4.6: (a) Mean (2002–2017) basal melt in BRIDGE. Difference (2002–2017) in the mean basal melt between (b) noBRIDGE and BRIDGE and (c) cATMO and noBRIDGE. The ice shelf edge is indicated by a gray contour and location of the grounded iceberg A23-A (2002–2017) is marked by a triangle in all panels.

As an indicator of the interannual density variability, I follow the volume-averaged potential density in the southern Filchner cavity (south of 80.4°S) (Fig. 4.7 c). The annual volume-averaged density time series for BRIDGE shows phases with higher density (>1028 kg m^{-3}) during 2006–2010 and subtle variations around smaller values for 2012–2017. The former coincides with the phase of higher densities on the western continental shelf (averaged over sub-region RO from Fig. 2.3) 2006–2010 (Fig. 4.7 a), indicating a stronger influence of the Ronne-sourced HSSW. The latter agrees well with the observed Berkner mode in 2013, 2014, and 2017 (Janout et al. 2021, Hattermann et al. 2021). However, the density variations in the noBRIDGE experiment seem closely related to the density variations on the eastern continental shelf (averaged over sub-region FI from Fig. 2.3). They decrease 2003–2010, and increase 2011–2013, indicating a stronger influence of the Berkner-sourced HSSW on the interannual variability without the presence of the bridge.

Corresponding to the atmospheric-driven intensification of sea ice production, density on the western continental shelf increases in all the experiments from 2015, followed by an increase in density in the southern Filchner cavity in 2017. However, during this phase, the fast-ice bridge was not extending to the grounded iceberg (Fig. 4.4 d, fast-ice area $< 50\%$) as fast ice was limited to the areas along Berkner Island and the Filchner Ice Shelf. Consequently, its effects on the sea ice production and density on the continental shelf were weaker than when it was fully formed (e.g., 2005–2010, Fig. 4.4 and 4.7). Therefore, the question remains whether the presence of the fully formed ice bridge could have modified the density variations in the cavity. From conditions of the BRIDGE experiment at the end of 2014, I extend a 3-year simulation with the same setup as BRIDGE except that instead of a monthly variable fast-ice mask I prescribe a fixed fast-ice mask based on conditions from August 2009, when the ice bridge was fully formed (Fig. 2.5 c) (statBRIDGE). As shown in Fig. 4.7 c, results indicate that the presence of the fast-ice bridge leads to a faster and stronger density increase in 2017.

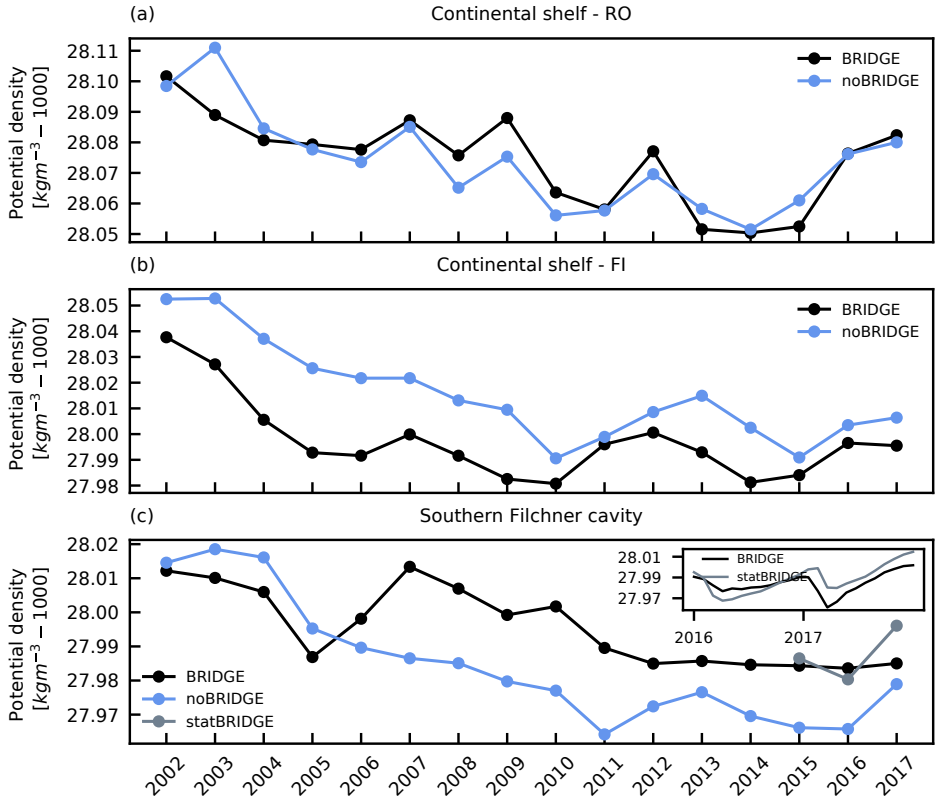

Figure 4.7: (a) Time series of the volume-averaged density on the (a) western (sub-region RO) and (b) eastern continental shelf (sub-region FI) and (c) within the southern Filchner cavity from the FESOM experiments.

4.5 Summary of the chapter

In this chapter, I investigated the impact of regional atmospheric forcing and the representation of the stationary icescape features on the surface freshwater flux in the southern Weddell Sea based on differences between the sensitivity experiments and reference simulation from Chapter 3.

I found that regional distribution and variability of sea ice production depend both on the regional atmospheric forcing and the representation of the icescape. Representing the variable ice bridge between Berkner Island and the grounded iceberg A23-A is important for a realistic simulation of polynyas that form west of it and suppresses the sea ice production eastward of it. Furthermore, using high-resolution regional atmospheric forcing leads to more realistic polynya ice production over the eastern continental shelves due to weaker offshore winds. Changes in the ice production are reflected in the HSSW production, which in turn produces noticeable changes in the circulation of the Filchner-Ronne system. Due to the weaker HSSW inflow under the Filchner Ice Shelf during the presence of the ice bridge, the basal melt under the Filchner Ice Shelf is reduced.

All simulations show a decrease in the southern Weddell Sea ice production for 2002–2017 with increase for 2015–2017 under the influence of the large-scale atmospheric forcing circulation. Decreasing decadal trend (24%, 1992–2017) in sea ice production is simulated using ERA-Interim reanalysis as a forcing, however using regional atmospheric forcing leads to a smaller decrease for 2002–2017 (7% compared to 16%). The model forced with regional atmospheric forcing and including representation of the fast-ice bridge captures well the important features of observed interannual variability in surface freshwater flux and oceanic circulation on the southern Weddell Sea continental shelf. The results further indicate that without the presence of the fast-ice bridge, simulated circulation under FRIS favors the Berkner mode and that the ice bridge can influence transitions between the sub-ice shelf circulation modes.

Influence of fast ice, initial conditions and sea-ice parameterizations on the southern Weddell Sea freshwater flux will be explored further in the next chapter.

5. Optimized simulation

As has been demonstrated in the previous chapters, the location and strength of sea ice production in coastal polynyas are improved by using the regional atmospheric forcing and including the representation of the stationary icescape features in the model.

In the following chapter, I combine this knowledge to produce the optimized solution of the southern Weddell Sea surface freshwater flux by i) deriving the new initial state based on a longer simulation including the representation of fast-ice climatology, ii) including representation of the variable ice bridge and fast-ice climatology, and as the last step, iii) using the Green's function method to optimize the sea ice parameters.

I discuss the role of each step for minimizing the model bias defined by the cost functions (Eq. 2.26 and Eq. 2.29) and identify the parameters crucial for a more realistic sea ice and ocean representation on the southern Weddell Sea continental shelf. Furthermore, I revisit the estimates of the southern Weddell Sea surface freshwater flux and discuss them in the context of the other experiments presented in this thesis and observation-based estimates. Finally, I suggest possible solutions to the unsolved problems encountered in my approach.

5.1 Initial conditions and icescape

The representation of the stationary icescape influences the location and strength of the simulated sea ice production in the southern Weddell Sea, as has been demonstrated in Chapter 4. With the help of MODIS data (sect. 2.3.2) with high temporal and spatial resolution, the monthly evolution of the dynamic ice bridge that was forming in front of Berkner Island 2002–2017 can be represented in the model. However, this data is available only from 2002 and is not suitable for the detection of the narrow fast ice extending along

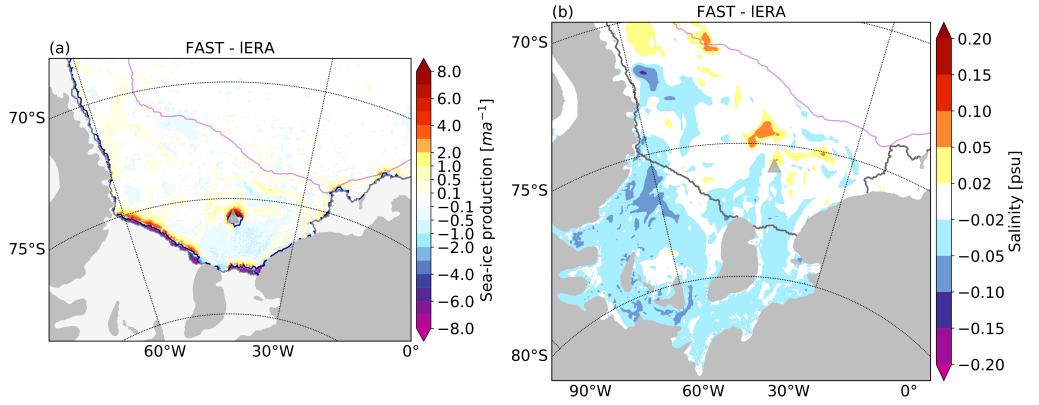

Figure 5.1: a) The mean sea ice growth rate difference (1992–2001) between simulations with and without fast ice (FAST and lERA). The fast ice (occurrence >90%) from (Nihashi & Ohshima 2015*b*) is contoured in blue. b) Difference in mean bottom salinity for 2001 between simulations with and without the representation of fast ice (FAST and lERA). The 2500 m isobath is indicated by violet contour in both panels. Note that the colormap does not linearly scale with the data.

the ice shelf. Based on passive microwave data, Nihashi & Ohshima (2015*b*) calculated the occurrence of fast ice for 2002–2011. Fast-ice occurrence higher than 90% can be found along FRIS, indicating that fast ice is a robust feature in these areas (Fig. 5.1).

Under the hypothesis that including the fast-ice climatology leads to a more realistic initial ocean state on the southern Weddell Sea continental shelf and within the FRIS cavity, I conduct the new experiment (FAST) that is used as a quasi spin-up for the sensitivity experiments in this chapter. The FAST experiment is initialized in 1979 from temperature and salinity derived from the World Ocean Atlas data 2009 (Levitus et al. 2010), and run until the end of 2001 using ERA as atmospheric forcing. In regions where fast-ice occurrence was high (> 90%) based on data from Nihashi & Ohshima (2015*b*), I prescribe the sea ice velocities to zero to represent the immobile fast ice. Except for the representation of fast ice, this experiment is otherwise identical to the long ERA run (lERA, sect. 2.1.4) used to derive the initial conditions for the experiments in chapters 3 and 4. Simulated sea ice growth rates in the fast-ice regions in FAST are reduced compared to the simulation without the fast ice (lERA) and increased adjacent to fast ice. The differences between the experiments are the strongest in front of the Ronne and Filchner ice shelves and north of the fast ice associated with the grounded iceberg A23-A (Fig. 5.1a). Consequently, the mean bottom salinity

at the end of the simulation in 2001 is reduced in front of FRIS and within the FRIS cavity, and increased north of the iceberg (Fig. 5.1b).

5.2 Sensitivity experiments

I apply a sequential approach to optimize the simulated Weddell Sea surface freshwater flux. The noBRIDGE experiment (2002–2017), using CCLM as atmospheric forcing and without the representation of the stationary icescape (sect. 2.1.4), is used as the baseline simulation for the sensitivity experiments and I refer to it from now on as S0 (Table 5.1). All sensitivity experiments (Table 5.1) started in 2002 from the initial conditions described below and run until the end of 2011 with CCLM as the atmospheric forcing (see sect. 2.2.2 for more detail).

First, I adapt the initial conditions (the S1 experiment, Table 5.1). Then, I include a representation of the stationary icescape (the S2 experiment, Table 5.1) similar to the reference experiment from Chapter 3. I use the cost functions J and J_d and normalized change in cost functions as defined in sect. 2.5 to measure the quality of the sensitivity experiments S1 and S2 relative to the baseline simulation S0 for 2002–2011 (Table 5.3). Finally, I estimate the optimal sea-ice model parameters using the Green's function approach described in sect. 2.4.

5.2.1 Sensitivity experiments S1 and S2

A sensitivity experiment (S1, Table 5.1) is derived from the conditions of FAST at the end of 2001. Except for the different initial conditions, the S1 experiment is identical to the S0 experiment. While sea ice motion cost in S1 does not change when compared to S0, the sea ice concentration cost decreases for -3% (Table 5.3). The total ocean cost in S1 reduces by -4.7%. The ocean temperature cost decreases for -7.6% and the salinity cost reduces by -1.7%. Comparison of simulated thermohaline properties between the experiments (Fig. 5.3b) shows this is mostly due to the improved properties of ISW (with temperatures below the freezing point) that can be found in the Filchner Trough.

In addition to the improved initial conditions, the S2 experiment (Table 5.1) includes the representation of the stationary icescape. The fast-ice climatology is used in the same way as in the FAST experiment, and the vari-

Experiment	Parameter	Baseline (S0)	Perturbation	OPTI
S1	Initial conditions	lERA	FAST	FAST
S2	Icescape	none	based on sat. data	based on sat. data
G1	Lead closing h_0 [m]	0.50	0.60	0.47
G2	Sea ice melt albedo	0.68	0.66	0.63
G3	Snow melt albedo	0.77	0.75	0.79
G4	Ice-atmosphere drag	0.0016	0.0015	0.0016
G5	Ice-ocean drag	0.0050	0.0045	0.0053
G6	Ice strength P^* [Nm^{-2}]	15000	16000	16001
G7	Salinity ice [psu]	5.0	4.0	5.5
G8	Sea ice albedo	0.75	0.74	0.76
G9	Snow albedo	0.85	0.84	0.86

Table 5.1: List of experiments in the optimization approach.

able ice bridge data is used as in the BRIDGE experiment from Chapter 3. This reduces slightly the sea motion cost (-0.5%), while the sea-ice concentration cost reduces by -7.3% mostly due to the improved summer sea ice concentration in the southern Weddell Sea in S2 (5.2 b). The representation of fast ice and ice bridge between Berkner Island and A23-A in S2 results in a more realistic sea ice concentration pattern with lower ice concentration west of the ice bridge, higher east of it and in the fast-ice areas. The net ocean cost decreases (-12.5%) as the temperature and salinity cost reduce by -12.5% and -12.7%, respectively. Fig. 5.3 shows improvement in properties of HSSW (lower salinities) and ISW (lower temperatures) in S2 compared to S1 and S0 in locations of the CTD measurements (2002-2011).

The change in cost function (ΔJ) for each data set between the experiments (Table 5.3) shows that the simulated results in S1 and S2 improve or do not degrade relative to the S0 experiment in all analyzed aspects. The changed initial conditions lead to the reduced total cost in S1 by -3%, while including representation of the stationary icescape in S2 reduces the cost further by -8.2% compared to S0. Improved initial conditions improve most significantly ocean temperature, while including the representation of fast-ice improves most significantly ocean salinity and summer sea ice concentration. Therefore, the initial conditions for the further sensitivity experiments (G1–G9, Table 5.1) in the optimization approach are derived from the conditions of the FAST experiment at the end of 2001, while representation of the icescape is included based on the satellite data as in S2.

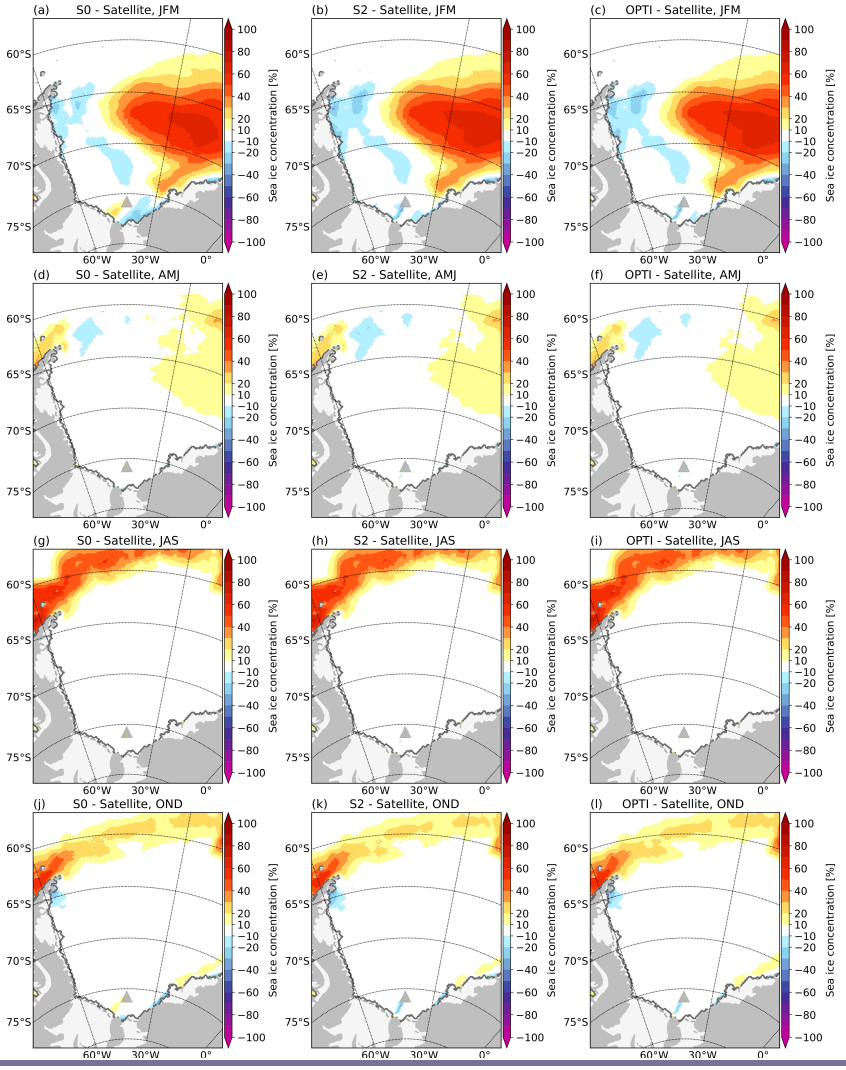

Figure 5.2: (a) Mean seasonal difference (2002–2011) between the simulated sea ice concentration (S0,S1,OPTI) and satellite data over the Weddell Sea. The solid gray line and the dashed gray line contour the ice shelf edge from the data and the model, respectively. The location of the grounded iceberg A23-A (2002–2017) is marked by a triangle.

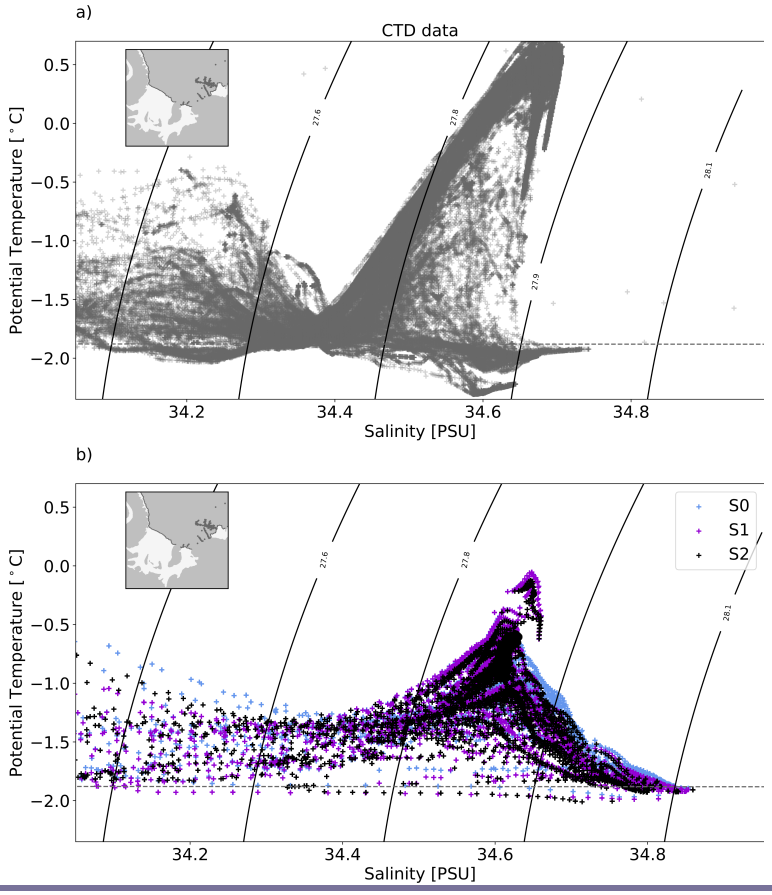

Figure 5.3: Temperature-salinity diagrams from (a) the CTD measurements (2002–2011) and (b) the sensitivity experiments S0, S1 and S2 (2002–2011). Model results are sampled at the locations of the CTD data. Maps in the insets show locations of the CTD data. Potential density ((1000-σ)kgm^{-3}) contours are shown in black lines and dashed gray line indicates the seawater freezing temperature.

5.2.2 Sea ice parameters

In this section, I assess the impact of the perturbed sea-ice model parameters on the simulated southern Weddell Sea surface freshwater flux. I conduct one model integration for each perturbed parameter leading to nine sensitivity experiments (G1–G9) all started from the same conditions as the S2 experiment, run for the period 2002–2011 using the CCLM data as the atmospheric forcing, and including the icescape representation as in S2 (Table 5.1). The selected parameters have been previously used in the sea-ice model sensitivity studies (e.g. Miller et al. (2006), Nguyen et al. (2009)) and influence the sea ice state through different sea ice parameterizations (i.e. thermodynamics, dynamics).

The lead closing parameter ($h0$), sea ice and snow albedos, drag coeffi-

cients and ice strength parameter (P^*) have been commonly recognized as most influential on the sea ice state. Due to its effect on the surface freshwater flux (sect. 2.1), I also perturb the value of sea ice salinity.

Due to the dominant influence of sea ice on the simulated surface ocean freshwater flux in the southern Weddell Sea (see Chapter 3), modifications in the sea ice parameters also influence the ocean fields on the southern Weddell Sea continental shelf. I assess the effects of the sea-ice model parameter perturbations on the sea ice production and ocean fields in the southern Weddell Sea by comparing the difference between each sensitivity experiment and S2. Furthermore, I use the Green's function (GF) approach (sect. 2.4) to estimate the optimal values of nine sea ice model parameters based on the experiments G1–G9 (Table 5.1).

The lead closing parameter

The lead closing parameter (h_0) controls the closing rate of sea ice leads and affects the thickness of newly formed ice. The value of h_0 used in the previous modeling studies of sea ice in the Weddell Sea (Timmermann et al. 2009) is 1.0 m, while here the reference value is 0.5 m (Table 5.1).

Increasing the value of h_0 (by +20% of the default value) (G1, Table 5.1) increases the sea ice production (by 1 $\mathrm{m\,a^{-1}}$) in coastal polynya regions as the ice grows thicker during the ice growth season (Fig. 5.4b). Consequently, the melting increases during the melt season (Fig. 5.5b). Due to the higher sea ice production in coastal polynyas with increased h_0, the bottom salinity increases in the HSSW production locations (Fig. 5.6b). The higher bottom salinity can also be traced through the Ronne and Filchner cavities.

The sea ice and snow albedos

The albedos of ice and snow control the amount of reflected shortwave radiation and therefore the surface heat budget. They are adjusted to make up for the errors related to the atmospheric forcing. The measurements of sea ice in East Antarctica (Massom et al. 2001) show ice albedos vary with sea ice thickness. Albedos of snow-free ice or ice with a thin layer of snow (snow thickness<0.3m) range from 0.42–0.72 for the ice thickness between 0.3–0.7m, to 0.49–0.81 for the ice thickness>0.7m. In the model, the default albedo value for the frozen ice (without snow cover) is 0.75, while for melting ice, the default value is 0.68. In previous Weddell Sea modeling studies

(Timmermann 2000, Timmermann et al. 2009), the values used were 0.75 and 0.66, respectively. The measured Antarctic snow-covered surface albedo (Massom et al. 2001) varies with snow thickness, with values for thick snow (snow thickness>0.3m) between 0.77–0.85. Timmermann (2000), Timmermann et al. (2009) used albedo values of 0.85 for the frozen snow and 0.75 for the melting snow, while the default snow albedo values in this study are 0.85 and 0.77, respectively.

Perturbing the sea ice and snow melt albedo parameters affects the sea ice fields in the summer (melt) season. Decreasing the ice melt albedo (to 0.66) and snow melt albedo (to 0.75) (G3 and G4, Table 5.1) increases the effects of the shortwave radiation forcing on the surface heat budget, and in the southern Weddell Sea a stronger sea ice melt is found on average in G3 and G4 (Fig.5.5c,d). Perturbation of these parameters has a stronger effect in the marginal ice zone in summer where it leads to the stronger melt and ice concentration decrease (Fig. A.2)d,e). The decrease of dry ice albedo (to 0.74) and dry snow albedo (to 0.84) reduces the melt of fast ice and thick ice east of the ice bridge forming between Berkner Island and A23-A (Fig. 5.5i,j). Since perturbations of albedo values do not modify significantly sea ice growth (Fig. 5.4 c,d,i,j)), influence on salinity fields is not detected in these experiments (Fig. 5.6 c,d,i,j).

The ice drag coefficients and ice strength parameter

The ice-atmoshphere and ice-ocean drag coefficients and ice strength parameter (P^*) (sect. 2.1) are important for sea ice dynamical processes and affect the sea ice motion. Adjusting these parameters leads to more realistic sea ice velocities (Nguyen et al. 2011). The drag coefficients control the horizontal momentum exchange between atmosphere/ice and ocean/ice (Eq. 2.6 and 2.7) and are used in parameterisation of sensible heat fluxes. P^* denotes the compressive ice strength (Eq. 2.8) that determines the internal ice stress at which ice deformation is permitted, and therefore affects the mechanical redistribution of ice. In an earlier FESOM study, Timmermann et al. (2009) used a value of 20000 $\mathrm{N\,m^{-2}}$ for ice strength, 0.00132 for ice-atmosphere drag, and 0.003 for ice-ocean drag. The default values used in this study are 15000 $\mathrm{N\,m^{-2}}$, 0.0016, and 0.0050, respectively. The perturbation of P^* value (to 16000 $\mathrm{N\,m^{-2}}$, G6, Table 5.1) modifies ice melt (Fig. 5.5) in the region east of the ice bridge where the ice bridge blocks the movement of ice and ice is get-

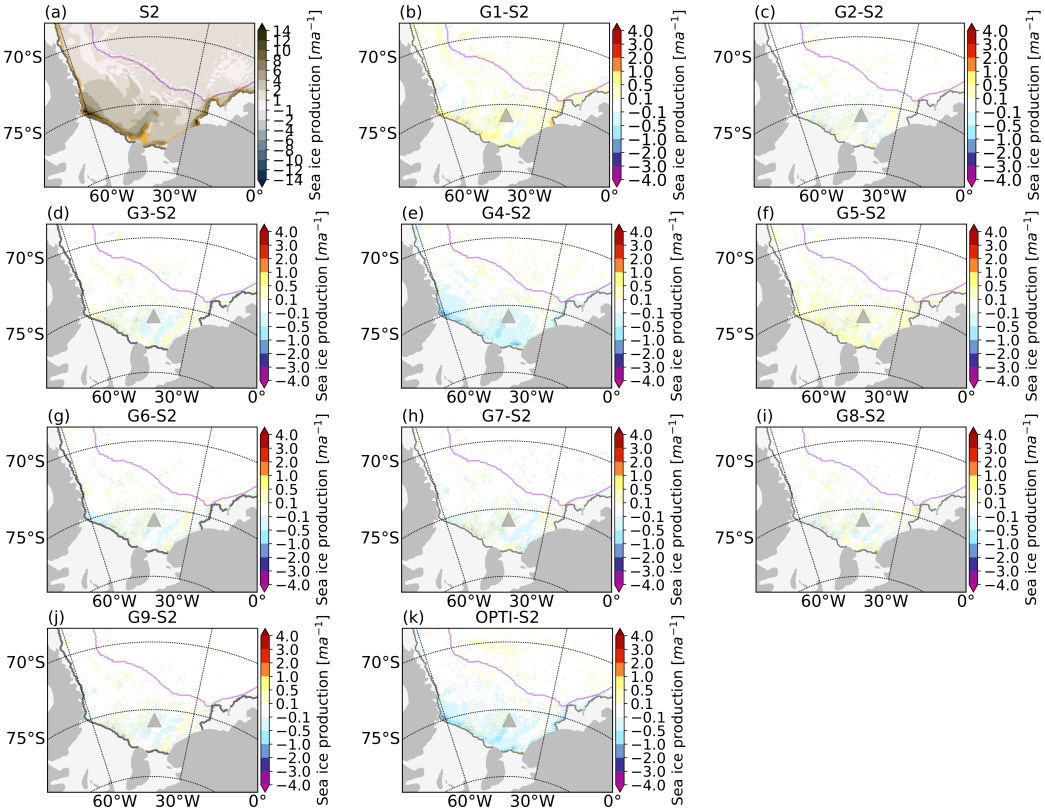

Figure 5.4: Sea ice production rate for months with the dominant sea ice growth (F–N, 2002–2011) on the southern Wedell Sea continental shelf from S2 (a), difference between G1–9 and difference between S2 (b–j) and OPTI and S2 (k). The average fast ice area in (a) is indicated by an orange contour. The location of the grounded iceberg A23-A (2002–2011) is marked by a triangle. The 2500 m isobath is indicated by a violet contour. The color map does not linearly scale with the data in (b–k).

ting dynamically deformed. Decreasing the ice-atmosphere drag coefficient (G4, Table 5.1), decreases the sea ice velocity and export of sea ice out of the southern Weddell Sea (Fig. A.4f). This leads to the decrease of sea ice production over the southern Weddell Sea continental shelf (Fig. 5.4e). Sea ice melt increases in regions of coastal polynyas and increases further offshore (Fig. 5.5e). As a consequence of decreased sea ice production, the salinity of dense water in front of the Ronne Ice shelf and Ronne cavity decreases (Fig. 5.6e). On the contrary, the decrease in the ice-ocean drag coefficient in the G5 experiment (Table 5.1) leads to an increase in sea ice production in coastal polynya regions (in front of the Ronne Ice Shelf, adjacent to the ice bridge, and west of the Brunt Ice Shelf). Consequently, bottom salinity increases in the corresponding regions and on the pathway of HSSW through

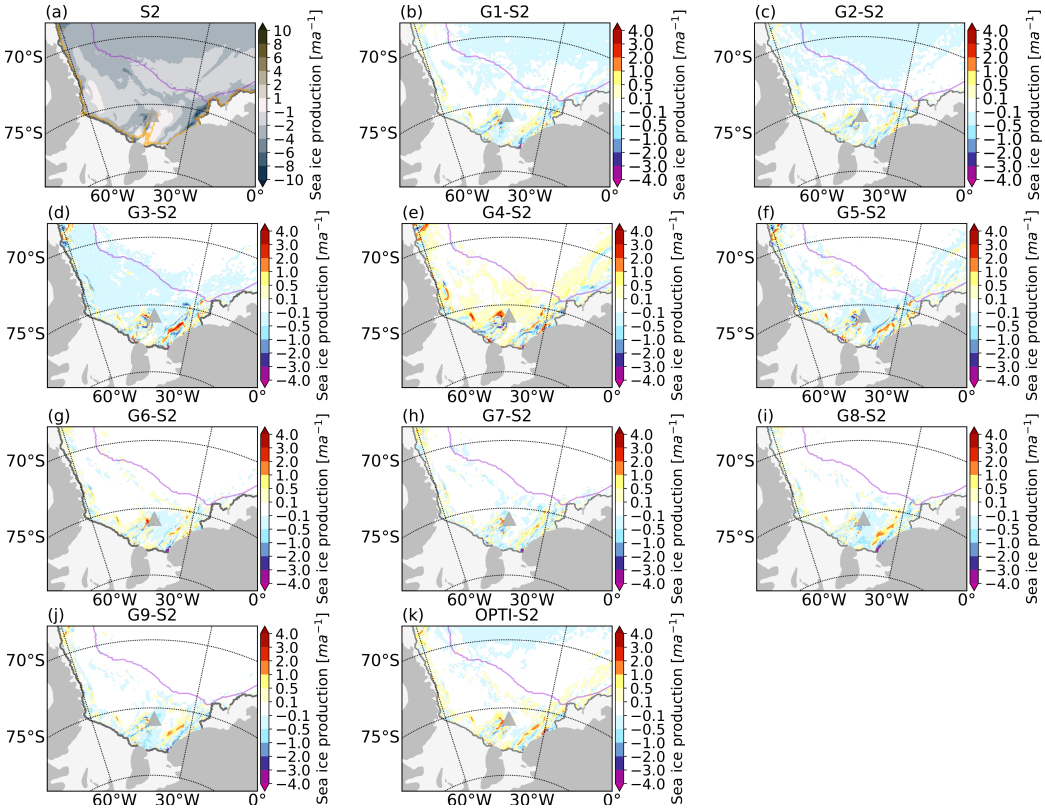

Figure 5.5: Mean sea ice production rate (negative values correspond to sea ice melt) for months with the dominant sea ice melt (J and D, 2002–2011) on the southern Wedell Sea continental shelf from S2 (a), difference between G1–9 and S2 (b–j), and difference between OPTI and S2 (k). The average fast ice area in (a) is indicated by an orange contour. The location of the grounded iceberg A23-A (2002–2011) is marked by a triangle. The 2500 m isobath is indicated by a violet contour. The color map does not linearly scale with the data in (b–k).

the ice shelf cavity (Fig. 5.6f).

Sea ice salinity

The smaller the sea ice salinity, the more salt is released to the ocean in the process of sea ice production, which affects the ocean stratification and in turn the ocean-ice heat flux. Timmermann et al. (2009) used a value of 5 psu for sea ice salinity, which is a default value in this study too. In the sensitivity experiment G7 (Table 5.1), the value of sea ice salinity is decreased to 4 psu. The resulting sea ice production increased (for 0.5 m a^{-1}) west of the ice bridge (in front of Ronne Ice Shelf) and west of the Brunt Ice Shelf (Fig. 5.4h). In locations with ice production increase in front of the Ronne Ice Shelf, bottom salinity increased (up to 0.05 psu) as well (Fig.5.6h).

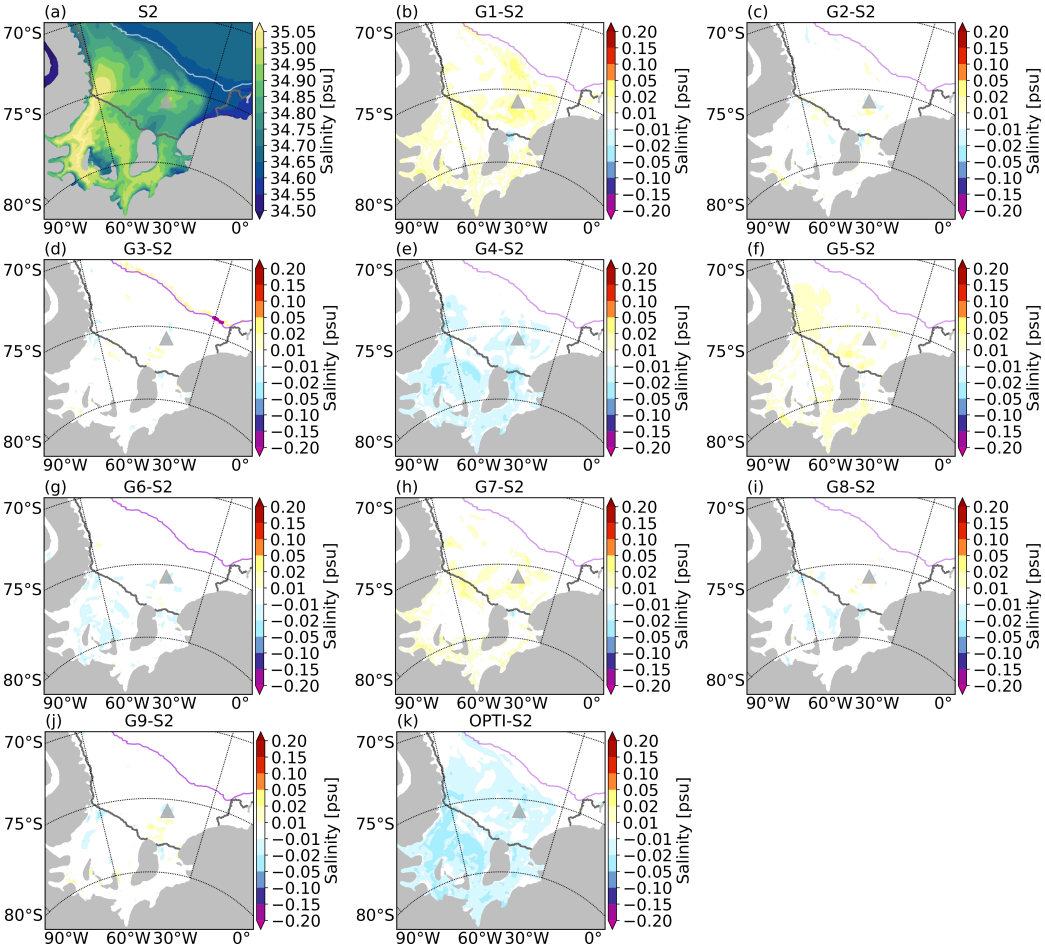

Figure 5.6: (a) Mean (2002–2011) bottom salinity from S2 (a). The ice shelf edge is indicated by a gray contour, and the 2500 m isobath is marked by a white contour. Difference (2002–2011) in the mean bottom salinity between G1–9 and S2 (b–j) and OPTI and S2 (k). The ice shelf edge is indicated by a gray contour, and the 2500 m isobath is marked by a violet contour. The location of the grounded iceberg A23-A (2002–2017) is marked by a triangle in all panels.

Optimized parameters

The values of parameters from the GF optimization are listed in Table 5.2. To infer the robustness of the parameter estimates under changes in the number of control parameters, I apply GF to each parameter one at a time and compare the estimates to those from the GF optimization of all nine parameters together (Table 5.2). The GF optimization of nine sea ice parameters yields 0.47m for the optimal value of h_0. Optimization of h_0 only, favors a slightly smaller value (0.46m). The optimization of nine sea ice parameters together yields a higher-than-default value of the sea ice albedo (0.76) and a

Parameter	h_0 [m]	Sea ice melt albedo	Snow melt albedo	Ice-atmosphere drag	Ice-ocean drag	P^* [Nm^{-2}]	Salinity ice [psu]	Sea ice albedo	Snow albedo
Default parameters	0.50	0.68	0.77	0.0016	0.0050	15000	5.0	0.75	0.85
Optimization all parameters	0.47	0.63	0.79	0.0016	0.0053	16001	5.5	0.76	0.86
Optimization one-at-a-time	0.46	0.68	0.77	0.0017	0.0051	14857	5.3	0.75	0.85
Timmermann et al. (2009)	1.00	0.66	0.75	0.00132	0.0030	20000	5.0	0.75	0.85

Table 5.2: Default parameters used in this study, optimized parameters from the GF approach, and values of parameters from Timmermann et al. (2009).

smaller-than-default value for the sea ice melt albedo (0.63). Optimization of each albedo parameter one at a time favors the default value for dry sea ice albedo (0.75) and the higher value for sea ice melt albedo (0.67) The higher values for both snow albedo parameters (0.86 and 0.79) result from GF optimization of all parameters. For comparison, optimization of each albedo parameter one at a time favors smaller values (0.84 and 0.77, respectively). The optimization of nine sea ice parameters yields values of 16001 Nm^{-2}, 0.0016, and 0.0053, for P^*, atmosphere-ice, and ocean-ice drag, respectively. Optimizing each parameter one at a time yields values of 14857 Nm^{-2} for P^*, 0.0017 for atmosphere/ice drag, and 0.0051 for ocean/ice drag coefficient. The GF optimization of all parameters favors the higher-than-default value for sea ice salinity (5.5psu), while the value from optimizing the sea ice salinity only is closer to the default value (5.1psu).

Because the parameter estimates are linearly dependent on each other, one-at-a-time estimates differ from the estimates from the optimization of all nine parameters together (Table 5.2). For example, the estimate of h_0 is limited between 0.46–0.47m, and therefore robust. However, the value of, for example, P^* (14857–16001 Nm^{-2}) or ice melt albedo (0.63–0.68) vary to a higher degree between the optimization cases and it can be inferred the estimate is not as robust under the increase in a number of control parameters.

A simulation carried out with the optimized set of parameters from the GF optimization of all nine parameters together is discussed in the next section.

5.3 Optimized simulation

In order to asses an overall improved skill of a model in representing the southern Weddell Sea surface freshwater flux, I conduct a new simulation

(OPTI, 2002–2017) using CCLM as atmospheric forcing and including (see also Table 5.1)): i) initial conditions from the FAST experiment, ii) including the representation of the variable ice bridge (2.3.2) and fast-ice climatology (Nihashi & Ohshima 2015*a*), iii) optimized sea ice parameters based on the GF approach (5.2).

As the optimization is limited to 2002–2011, the cost function for OPTI is evaluated for the same period. The cost reduction relative to the baseline simulation S0 (ΔJ from Eq. 2.30 evaluated for OPTI and S0) is -13.1%. Improvements for all the variables separately relative to S0 are listed in Table 5.3. To estimate improvements of the optimized simulation due to the GF optimization of sea ice parameters only, I evaluate the cost reduction relative to the S2 experiment as well (ΔJ from Eq. 2.30 evaluated for OPTI and S2). The expected cost reduction from the GF approach assuming linearity is -5.5%. The linearity assumption will be discussed later, however, the actual cost reduction of the optimal simulation due to the change in the sea ice parameters only is -5.1%. The optimization of sea ice parameters did not influence all the variables included in the cost evenly. The cost reduction of OPTI relative to S2 calculated for each data set separately yields a -2.5% reduction for sea ice concentration, -5.0% for sea ice motion, and -17.7% for ocean salinity. The ocean temperature cost, however, increased by +4% compared to S2. However, the temperature cost relative to S0 is still reduced (by -8.4%).

Experiment	S1	S2	OPTI
Net cost	-3.0%	-8.2%	-13.1%
Sea ice concentration cost	-3.0%	-7.3%	-9.6%
Sea ice motion cost	0.0%	-0.5%	-5.0%
Ocean temperature cost	-7.6%	-12.5%	-8.4%
Ocean salinity cost	-1.7%	-12.7%	-28.7%

Table 5.3: Cost reduction (ΔJ) from the S1, S2 and OPTI experiment relative to the S0 experiment.

The seasonal mean difference between the simulated sea ice concentration and satellite data (Fig. 5.2) shows reduced anomalies in OPTI when compared to S2 for the coastal polynya regions on the southern Weddell Sea continental shelf. The largest biases, found in the marginal ice zones and at the ice edge in summer (Fig. 5.2 a,b,c) and winter (Fig. 5.2 g,h,i), do not improve significantly in OPTI when compared to S2 or S0. The uncer-

tainty of the sea ice concentration data (Sect. 2.3.1) is higher closer to the ice edge. The contribution from those regions to the cost function is, therefore, weighted less than the contribution from regions with pack ice where model agrees better with the data. The choice of parameters for the GF optimization and its implications for the sea ice concentration cost will be discussed later on.

The modest reduction of the sea ice motion cost in OPTI when compared to S2 are mostly due to the lower average sea ice velocities in OPTI on the southern Weddell Sea continental shelf (Fig. A.4 b). The choice of the dynamic solver can have effects on the simulated sea ice velocity at least as large as the atmospheric forcing, ice rheology, and ice-ocean stress coupling (Losch et al. 2010), which can limit the improvements of sea ice velocity through the optimization of sea ice parameters (Zampieri et al. 2021). The impact of the EVP solver formulation on the simulated sea ice state was not investigated in this study and could be important for the improved simulation of sea ice velocity.

The comparison between the bottom salinity in S2 and OPTI reveals the shift towards smaller salinities on the southern Weddell Sea continental shelf in the OPTI experiment (by 0.02–0.05 psu) (Fig. 5.6k). The comparison with the CTD data from 2011 (Fig. 5.7a) shows a good agreement between the simulated salinity in OPTI and measurements for the eastern part of the continental shelf. The exception is the salinity in front of the Filchner Ice Shelf which is by 0.1 psu saltier than in the observations. The salinity in the same locations in S2 is even higher than in OPTI (by 0.05 psu) and thus showing a larger bias to the observed values. The observations indicate that the Filchner Trough was characterized by the colder Ronne-sourced-ISW in 2011 (Ronne mode) instead of the more locally produced water (Berkner mode) (Janout et al. 2021). The comparison of the simulated temperature with measurements in Fig. 5.8a shows that the coldest observed ISW in 2011 (temperature<-2.2 °C) is not present in OPTI, and similarly neither in the sensitivity experiments analyzed in this chapter (Fig. 5.3b and A.5). Another notable difference between OPTI and S2 in 2011 is a reduced inflow of the warmer mWDW on the eastern shelf towards the Filchner Ice Shelf front in OPTI (Fig. 5.8b). The seasonal mWDW inflow has been observed in recent moored temperature data and exhibits high interannual variability (Ryan et al. 2020). However, given that the presence of mWDW on the FRIS calving front has been observed only episodically in late summer and not in

2011 (Darelius et al. 2016), the inflow in S2 is likely too strong.

The agreement between the observations and simulated salinity and temperature in OPTI is generally good for 2013 (Fig.5.7c and 5.8c). The data from the year 2013 are not included in the calculation of the cost function (sect. 2.5), and therefore they are suitable to be used as an indication of model performance out of the optimization period (2002–2011). Furthermore, the year 2013 is representative of the observed Berkner mode (Janout et al. 2021). The observed salinities are maximally by 0.05 psu saltier in OPTI than in the observations. However, the FIS front is dominated by the locally produced dense water representative of the Berkner mode both in OPTI and the observations (Janout et al. 2021). Salinity in S2 over most of the continental shelf is higher (by 0.02–0.05 psu) than in OPTI, bringing the simulated values for 2013 in S2 further from the observations than OPTI. The simulated bottom temperatures in OPTI agree well with the observed near-bottom temperatures (Fig. 5.8c) and differences between the experiments in the locations of observations are not significant (<0.01 °C), suggesting overall good representation of conditions in the Berkner mode.

5.3.1 Surface freshwater flux

In this section, I asses the simulated surface freshwater flux for 2002–2017 in the optimized experiment. I also compare the coastal polynya representation and sea ice production estimates with those from the reference experiment (BRIDGE, Table 2.1) from Chapter 3. Furthermore, I asses differences in the HSSW representation and basal melt between the experiments. Both OPTI and BRIDGE use CCLM as the atmospheric forcing and include a representation of the variable ice bridge that was forming between Berkner Island and the grounded iceberg A23-A (sect. 2.3.2). However, as described earlier in this chapter, OPTI is started from different initial conditions, includes the representation of fast ice climatology in addition to the ice bridge, and is run with the optimized sea ice parameters (Table 5.2).

The average annual net surface freshwater flux for the southern Weddell Sea (Fig. 5.9a) in OPTI (-14.5 mSv, 1 mSv=1000 $m^3 s^{-1}$) is dominated by the freshwater removal from the sea ice production (-25.5 mSv). The melting of snow provides the average freshwater flux of 3.1 mSv, and the ice shelf basal melt flux provides 7.4 mSv. The relative contribution of the freshwater fluxes in OPTI is overall similar to the flux estimates from the

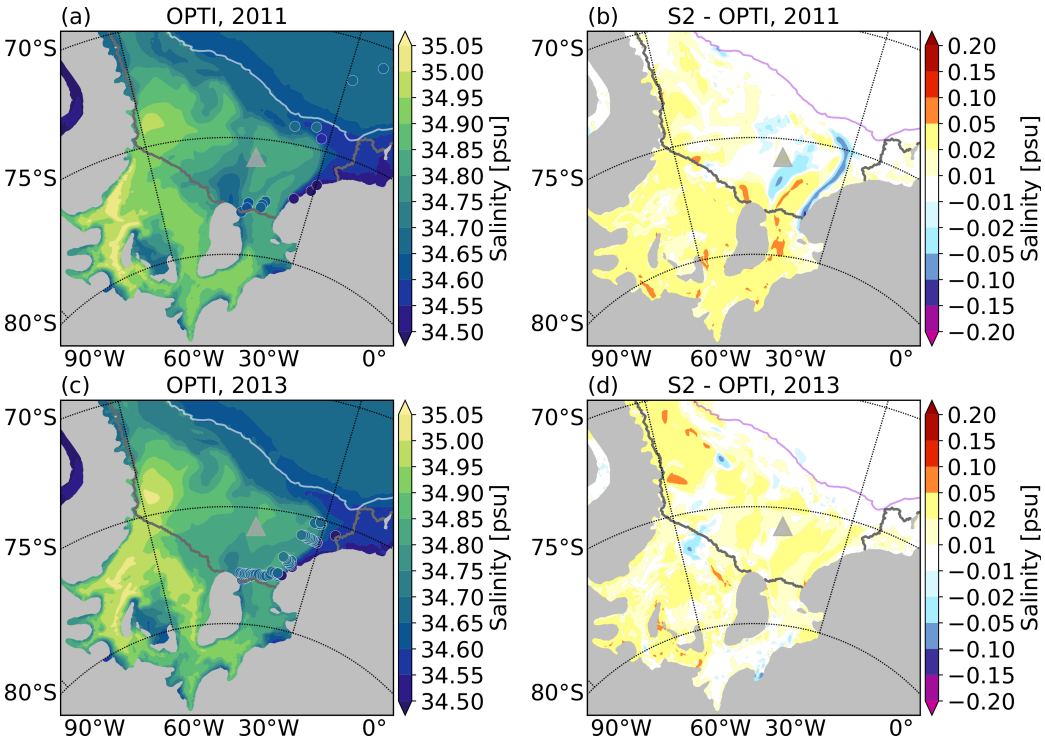

Figure 5.7: Mean bottom salinity for austral summer (JF), 2011 and 2013 from OPTI (a,c), and difference between S2 and OPTI (b,d). The circles in (a) and (c) mark the values of near-bottom salinity from the CTD measurements (2011 and 2013). The ice shelf edge is indicated by a gray contour. The 2500 m isobath is marked by a white contour in (a,c) and by a violet contour in (b,d). The location of the grounded iceberg A23-A (2002–2017) is marked by a triangle.

BRIDGE experiment in Chapter 3. However, both the average freshwater removal by the sea ice flux and the basal melt flux are stronger in BRIDGE (-27.1 mSv and 7.6 mSv, respectively).

Sea ice production

Including the representation of the stationary icescape based on the fast ice climatology (Nihashi & Ohshima 2015*a*) and variable ice bridge data (2.3.2) shifts the locations of the maximum ice production (Fig. 5.1a) and acts to reduce the polynya area. Furthermore, the optimized sea ice parameters reduce the mean sea ice growth rates (Fig. 5.4k). Similarly to the BRIDGE experiment, the strongest sea ice production rates in OPTI are found in the coastal polynyas along the ice-shelf fronts and coastlines. The maximum values are found in the corner between the Antarctic Peninsula and the Ronne Ice Shelf. However, due to the presence of fast ice along the Ronne Ice Shelf

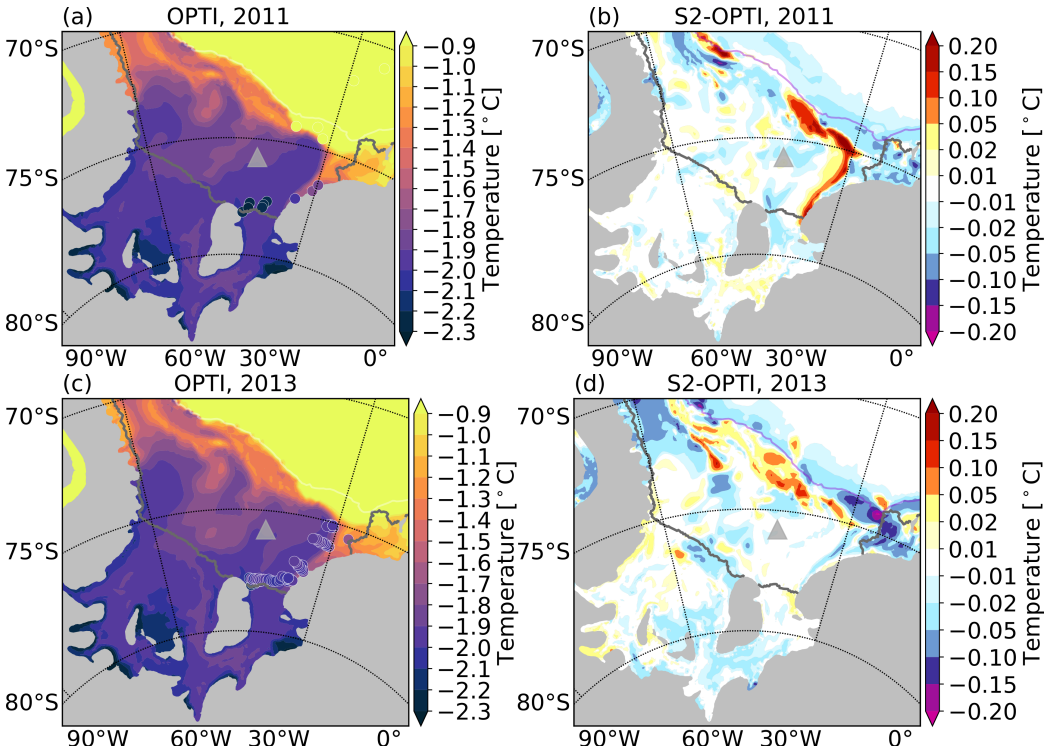

Figure 5.8: Mean bottom temperature (θ) for austral summer (JF) 2011 and 2013 from OPTI (a,c) and difference between S2 and OPTI (b,d). The circles in (a) and (c) mark the values of near-bottom temperature from the CTD measurements (2011 and 2013). The ice shelf edge is indicated by a gray contour. The 2500 m isobath is marked by a white contour in (a,c) and by a violet contour in (b,d). The location of the grounded iceberg A23-A (2002–2017) is marked by a triangle.

in OPTI, the maximum is weaker (by 2 m a^{-1}) and shifted north of the fast ice. The strong sea ice production rates are found also west of the Brunt Ice Shelf and west of the ice mélange associated to the grounded iceberg A23-A. The mean ice production in those locations is stronger in BRIDGE (by 1 m a^{-1}) than OPTI. The representation of the iceberg A23-A in the fast-ice data used in OPTI (Fig. 5.9a) leads to the shift of the strong ice production north of the iceberg in OPTI.

From the daily model output, I calculate the cumulative annual ice production within and outside polynyas. If the sea ice production is occurring at the nodes with a sea ice concentration smaller than 70% or thickness smaller than 20cm, it is counted as polynya ice production. Similarly to the BRIDGE experiment, in OPTI polynyas cover only 2% of the southern Weddell Sea area, yet contribute significantly to the regional ice production due to their higher average growth rates (21.0 m a^{-1} within the polynyas compared to 3.5

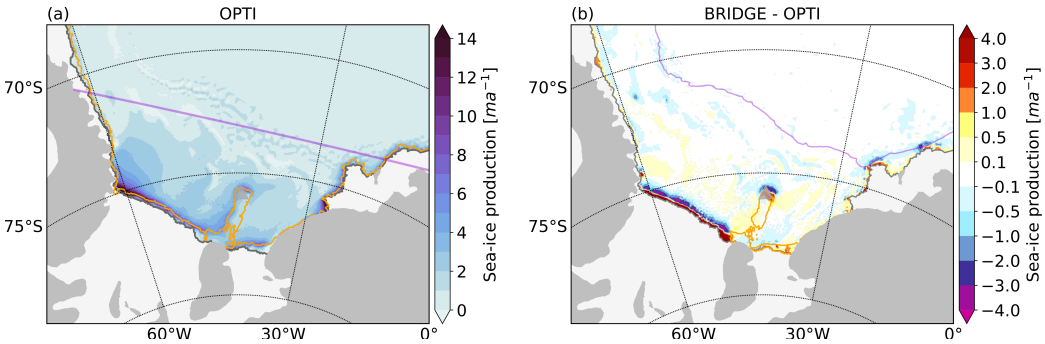

Figure 5.9: (a) Mean sea ice growth rates (2002–2017) from OPTI and (b) difference between BRIDGE and OPTI. The location of the grounded iceberg A23-A (2002–2017) is marked by a triangle. The area with 50% fast-ice frequency in both panels is indicated by an orange contour. Southern Weddell Sea control region is enclosed by the violet line in (a). Note that the color map does not linearly scale with the data in (b).

m a^{-1} outside polynyas). In OPTI, polynya sea ice production contributes 15% (212 $km^3\,a^{-1}$) to the total annual sea ice production (1451 $km^3\,a^{-1}$). The annual polynya ice production estimates for the six sub-regions adapted from Paul et al. (2015) (Fig. 2.3) are shown in Fig. 5.10. The largest mean annual ice production in OPTI is found in the Ronne (RO, 98 $km^3\,a^{-1}$), Brunt (BR, 68 $km^3\,a^{-1}$), and the region associated to the ice bridge (IB, 21 $km^3\,a^{-1}$). The mean annual ice production in OPTI for the Ronne region is by 21% smaller, and the mean ice production for the Brunt region is by 14% smaller than in BRIDGE (the values from the BRIDGE experiment 123 $km^3\,a^{-1}$ and 79 $km^3\,a^{-1}$, respectively).

Comparison of regional distribution and ice production estimates with FESOM simulations and satellite-based estimates from Paul et al. (2015) for April–September 2014 is shown in Table. 5.4. The optimized simulation (OPTI) yields the lowest estimates between the experiments. The largest reduction of ice production compared to the BRIDGE experiment is found for the Ronne (RO) and Brunt polynya (BR). The data from Paul et al. (2015) included a different landmask than the model, with the differences between the areas of integration for sea ice production being the largest for RO and FI. When integrating the model results over the extended areas defined in this thesis (Fig. 2.3), the differences between the simulated results and the satellite-based estimates for RO and FI reduce in OPTI when compared to BRIDGE (Table 5.4) due to the better representation of fast ice in OPTI. Similar to Paul et al. (2015), the largest contributions in OPTI come from

the Ronne (RO) and Brunt (BR) polynyas, and polynyas associated to the ice bridge (IB). The optimization brings the simulated regional distribution and polynya ice production estimates closer to the satellite-based estimates.

Method	AP	RO	IB	FI	CL	BR	Sum
S0 (noBRIDGE)	3±2 (7±4)	44±15 (72±21)	2±1 (3±1)	15±5 (39±11)	3±1 (3±1)	48±10 (50±10)	114±26 (173±35)
BRIDGE	3±2 (7±4)	52±18 (75±23)	15±7 (15±7)	9±6 (14±9)	3±1 (3±1)	45±9 (47±10)	127±31 (161±36)
OPTI	3±2 (5±4)	49±19 (55±20)	13±6 (13±6)	8±5 (11±7)	2±1 (2±1)	38±9 (39±9)	113±31 (126±33)
Paul et al. (2015)	4±3	29±12	11±5	9±7	4±3	30±11	87±26

Table 5.4: Cumulative polynya-based ice production (mean and standard deviation) [km^3] for April-September 2002–2014 from the the S0 experiment (noBRIDGE from Chapter 4), the BRIDGE experiment (Chapter 3), the OPTI experiment, and Paul et al. (2015), for six sub-regions defined in Paul et al. (2015). Values from the control regions shown in Fig. 2.3 for FESOM experiments are shown in parenthesis.

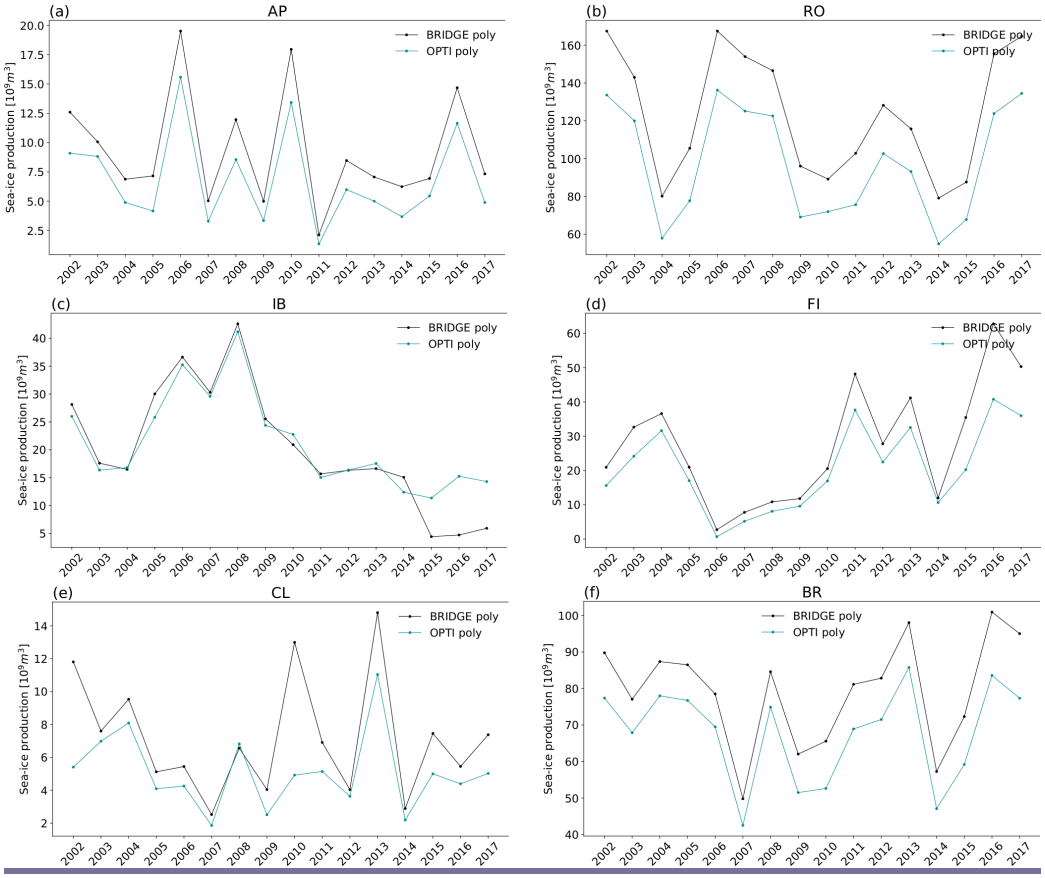

Figure 5.10: Time-series of the cumulative polynya ice-production (2002–2017) in the southern Weddell Sea from OPTI and BRIDGE for the six sub-regions shown in Fig. 2.3.

HSSW and basal melt

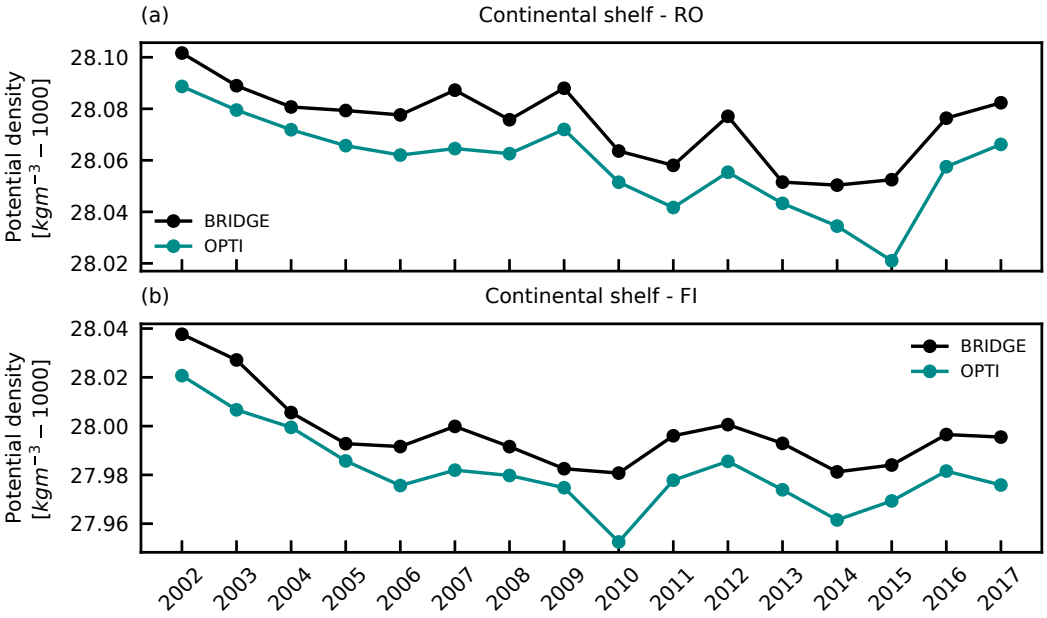

Figure 5.11: (a) Time series of the volume-averaged density on the (a) western (sub-region RO, Fig. 2.3) and (b) eastern continental shelf (sub-region FI, Fig. 2.3) from OPTI and BRIDGE.

To asses the HSSW density variability in OPTI and compare it with BRIDGE, I follow the volume-averaged density for the continental shelf for 2002–2017 (Fig. 5.11). The differences in the sea ice production between OPTI and BRIDGE are reflected in the properties of the dense HSSW. Corresponding to the lower sea ice production in OPTI when compared to BRIDGE (Fig. 5.10) are the lower average densities on both the western (averaged over sub-region RO from Fig. 2.3) and eastern continental shelf (averaged over sub-region FI from Fig. 2.3). Similarly to the ice production rates (Fig. 5.10), the variability of the volume-averaged density is very similar between the OPTI and BRIDGE experiment (see Chapter 4, Sect. 4.4 for more details about the density variability in BRIDGE). The difference in the density gradients between the continental shelf and the cavity leads to the stronger HSSW inflow to the cavity in BRIDGE than in OPTI (not shown), leading to the stronger basal melt rates at the Ronne Ice Shelf Ice front and within the Filchner cavity (up to 0.5 $\mathrm{m\,a^{-1}}$).

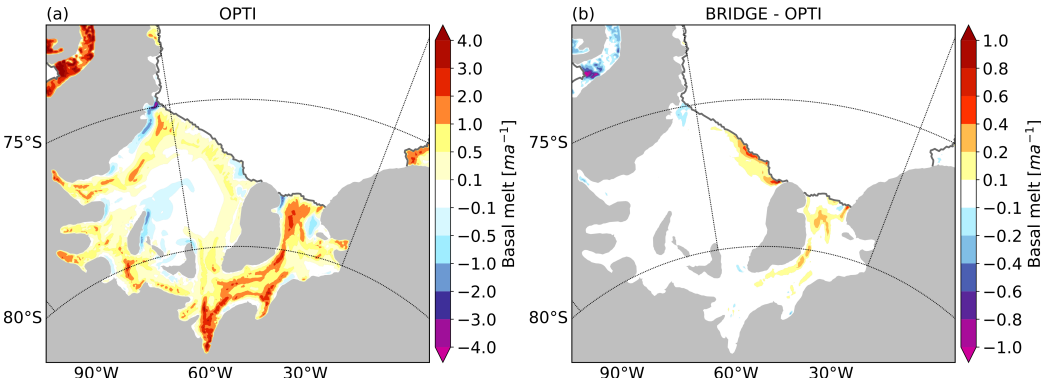

Figure 5.12: (a) Mean (2002–2017) basal melt from OPTI. (b) Difference in the mean (2002–2017) basal melt between BRIDGE and OPTI.

5.4 Discussion

5.4.1 Linearisation

As has been demonstrated by Menemenlis et al. (2005), the exact linearity is not required for the GF approach to work and the optimization of a small number of chosen parameters can have a positive impact on the model solution. The linearity assumption of the GF method holds if the following condition (Menemenlis et al. 2005) is satisfied:

$$abs[G(\boldsymbol{\eta_{opt}}) - G(\boldsymbol{\eta_0}) - \boldsymbol{G\eta_{opt}}] \ll diag(\boldsymbol{R}^{1/2}), \tag{5.1}$$

where operator abs() returns a vector that contains the absolute values of the input vector elements and operator diag() returns a vector that contains the diagonal elements of the input matrix. If the condition is not satisfied, it may be possible to further reduce the cost function by applying another iteration of the optimization and relinearising the model around the parameters from the first iteration. Based on the results from OPTI, the right-hand side of Eq. 5.1 is approximately 3 times larger than the left-hand side. Therefore the errors due to nonlinearity are approximately 33% of the assumed errors in the model and the data. Since the linear approximation is roughly satisfied based on criteria from Eq. 5.1, further iterations to optimize the selected nine parameters are not expected to lead to a major change in the results.

However, the results from the last optimization step indicate that some

biases, such as the sea ice concentration bias in the marginal sea ice zone or properties of ISW that can be found on the continental shelf, are not improved by the optimization approach presented here. The reasons for this might lie in the composition of the cost function that does not constrain well all the processes relevant for the sea ice and ocean conditions in the southern Weddell Sea. The ocean cost was limited to the sparse ocean data for the southern Weddell Sea. The data was available only for the eastern part of the continental shelf for summer months in 2003, 2005, 2009, and 2011 (Fig. 5.3 inset). The sea ice budget could be better constrained by including the sea ice and snow thickness data that become available in the future. Moreover, limitations of the improvements from the optimization approach in this study also arise from the choice of parameters used for the optimization which is discussed next in more detail.

5.4.2 Remaining issues

The results from the sensitivity experiments and optimized simulation (Table 5.1) suggest that the magnitude of surface freshwater flux and contribution of polynya sea ice production to the surface freshwater flux are sensitive to the choice of sea ice parameters. The optimization procedure leads to improvements of sea ice and ocean state on the southern Weddell Sea continental shelf. Furthermore, the resulting sea ice production estimates are closer to the observation-based estimates. However, the sea concentration in the marginal ice zones does not improve with the optimization. The hypothesis that including additional sea ice model parameters to the GF optimization procedure, such as the ocean to ice heat transfer coefficients, or various parameters controlling the sea ice dynamics, could improve the sea ice concentration bias has been rejected based on short (1–3 years) sensitivity experiments (not shown). The realistic simulation of the Southern Ocean sea ice extent and its trends is challenging, and realistic sea ice extent simulations do not guarantee the realistic sea ice budget representation as a too-strong sea ice production can be balanced by the extensive ice drift and too strong melt (Uotila et al. 2014). The representation of ocean fluxes has been found crucial for the correct representation of the Southern Ocean sea ice extent in both a sea ice-ocean model (Su 2017) and a coupled atmosphere–sea ice–ocean model (Rackow et al. 2017) studies.

The horizontal (ocean) diffusivity parameter (K_h, Eq. 2.5) plays a role in

eddy parameterization and for cross-isopycnal mixing and is therefore important for the representation of oceanic fluxes. The value of K_h in the model is set constant and scaled down with a finer resolution based on a scaling function (Wang et al. 2014). The default value of K_h used in this study is 600 $m^2\,s^{-1}$. For comparison, in another FESOM study Wang et al. (2014) used value of 1500 $m^2\,s^{-1}$. The results of the additional sensitivity experiment (Sdiff) conducted with a higher value of K_h (900 $m^2\,s^{-1}$) show the reduced sea ice concentration bias in the marginal ice zones (Fig. 5.13a and b). However, using the higher value of the horizontal diffusivity parameter produces a non-linear response and undesired effects on the continental shelf. Due to the too-strong mixing acting along isopycnals, more warm water (mWDW) intrudes on the shelf, and flows into the Filchner cavity (Fig. 5.13c). This tipping point behavior has been observed in studies of FRIS under the future climate (Hellmer et al. 2017, Naughten et al. 2021), and has been attributed to the decreased southern Weddell continental shelf salinity under future changes in the surface freshwater fluxes. Idealised model studies have produced this regime shift through a decrease in the meridional winds (Hazel & Stewart 2020) or a freshening of the dense shelf water and relaxing the ASF (Daae et al. 2020).

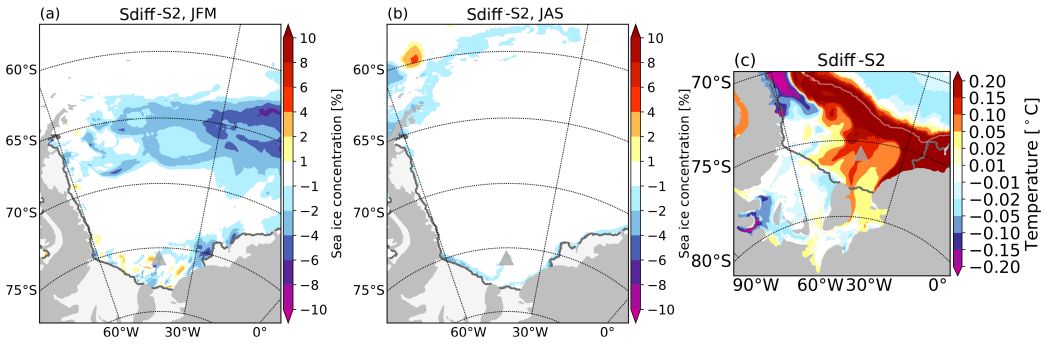

Figure 5.13: Mean difference in sea ice concentration between Sdiff and S2 for (a) summer (JFM) 2002–2011 and (b) winter (JAS) 2002–2011. (c) Mean difference in summer bottom temperature (θ) between Sdiff and S2 (JFM, 2002–2011).

In the FESOM version used in this study, along-sigma diffusion paremeterization is used on sigma grid, as using neutral physics parametrization (GM/Redi, see Sect. 2.1.4) leads to numerical instabilities (Wang et al. 2014). The too-strong warm water inflow with the higher K_h could be related to the too-strong mixing related to the horizontal advection term on sigma layers (Mellor et al. 1994, Lemarié et al. 2012). Some solutions at hand that can

help to balance the extensive mixing on the continental shelf in the case with the higher value of horizontal diffusivity discussed here, namely, modifying the scaling with the resolution factor and gamma coefficient used in GM parameterization, did not produce strong enough effects on the warm water inflow (not shown). The obvious solution to the problems that arise from using the sigma coordinates is using the z-level grid instead. Still, the benefits of sigma grid make it a desirable feature for representing the processes on the sharp slopes of the Weddell Sea continental shelf break and within the ice shelf cavity.

There are other possibilities that could be implemented in future work on the subject. Implementing an alternative vertical coordinate system such as a "vanishing quasi sigma grid" (as suggested by Sergey Danilov, personal communication) can keep the benefits of using the terrain following component and allow for more flexibility in the transition to the z-levels. This would require implementing a new method for mesh generation and (probably) minor changes to the existing parameterization. A new horizontal advection scheme that would not introduce along-sigma mixing could potentially help with similar problems and would be beneficial in case of hybrid grids. Furthermore, representing the mesoscale eddies that drive the warm water across the continental slope requires higher horizontal resolution than used in this study (Sect. 2.1.4 and Fig. 2.3) due to the small deformation radius at high latitudes (2–4 km on the continental shelf and 1 km in the ice cavity, Ryan (2018)). In a recent idealized modeling study, Dettling et al. (2023) found that the heat flux related to the mWDW inflow on the continental shelf can be successfully simulated using GM/Redi scheme, however only when it is implemented using the slope-aware eddy parameterization.

Another issue to discuss is the representation of the ISW in the Filchner Trough (Fig. 5.8a). The temperature and salinity properties in the optimized simulation agree favorably with the observations for the period with the observed Berkner mode. However, in the case when observations suggest that conditions in the Filchner Trough corresponded to the Ronne mode, in the simulated results the locally produced dense shelf water dominates the Filchner Ice Shelf front instead of the Ronne-sourced ISW. The lack of the colder ISW could be related to the too-weak transport of the Ronne-sourced ISW from the Ronne cavity to the Filchner cavity, and then further onto the continental shelf through the Filchner Trough.

5.5 Summary of the chapter

I used fast ice, sea ice and hydrographic data from the southern Weddell Sea continental shelf to constrain the model and produce an optimal simulation with i) improved initial conditions, ii) representation of fast ice and variable ice bridge, and iii) optimized sea ice parameters based on the Green's function approach.

The adapted initial conditions helped to improve the ocean conditions on the southern Weddell Sea continental shelf. The representation of fast ice is important for the realistic simulations of the sea ice concentration and ocean salinity on the southern Weddell Sea continental shelf, while optimization of nine sea ice parameters leads to the further improvements. Modest improvements have been noted for sea ice motion with the optimized sea ice parameters. The missing sea ice thickness constrain and adapting the EVP solver could help to produce better improvements in the future. The remaining sea ice concentration bias in the marginal ice zones points to the limitation of the optimization procedure including Green's function with the limited sea ice and ocean data for this particular model configuration. Using higher-than-default value of the horizontal diffusivity parameter may help to minimize the large-scale sea ice concentration bias, however the perturbation can lead to the non-linear response in the ocean circulation of the FRIS system. While the features of the Berkner mode are represented well in the optimized simulation, the presence of the coldest ISW in the Filchner Trough representative of the Ronne mode remains a caveat. The issue could be linked to the transport of water masses within the cavity.

The surface freshwater flux is sensitive to the perturbations of sea ice model parameters. The sea ice production in the optimized simulation preserves the important advantages of the reference experiment from Chapter 3 regarding the regional distribution of ice production in coastal polynyas when compared to the sensitivity experiments from Chapter 4. Both the fast ice representation and the optimization of sea ice parameters act to reduce the accumulated sea ice production estimates. The optimization brings the regional sea ice production distribution and magnitude closer to the satellite-based estimates. While it does not affect the variability of sea ice production, it leads to the lowest sea ice production estimates when compared to other experiments in this thesis leading to the reduced HSSW density.

6. Conclusions and outlook

In this thesis, I used a sea ice–ice shelf–ocean model based on the finite-element method to investigate the role of sea ice in the southern Weddell Sea surface freshwater flux (2002–2017) with a special focus on coastal polynyas. I assessed the impact of the regionally downscaled atmospheric forcing (**O1**), the stationary icescape features (**O2**) and the influence of sea ice parameterizations (**O3**) on the simulated southern Weddell Sea surface freshwater flux. I estimated the contribution of coastal polynyas to the southern Weddell Sea surface freshwater flux and investigated how changes in the regional surface freshwater flux influence the representation of HSSW on the southern Weddell Sea continental shelf and basal melt of FRIS.

In the following, I summarize the results of this thesis and point to the findings relevant for each objective (**O**) defined in Chapter 1. After the overall conclusions, I discuss some open questions that are left and provide an outlook on possible future work based on the results from this thesis.

6.1 Summary and conclusions

The results from the reference FESOM simulation (2002-2017) (Chapter 3) based on the regionally downscaled atmospheric forcing, while including as well the effects of the ice bridge that had been forming between FRIS and grounded iceberg A23-A (2002–2017), show that the model represents reasonably well the surface freshwater flux components and variability when compared to observation-based estimates. The flux in the region is dominated by the extraction of freshwater due to sea ice production, which is strongest in the coastal polynyas. The sea ice growth rates within polynyas are on average 5 times stronger than the growth rates outside polynyas. Therefore, sea ice production within polynyas contributes 17% of the overall regional sea ice production even though coastal polynyas cover only 2% of

the continental shelf area. The largest contributions come from the Ronne Ice Shelf, Brunt Ice Shelf polynyas, and polynyas in front of the Filchner Ice Shelf, followed by the polynyas associated with the ice bridge. The strength of the simulated ice production estimates within the polynyas is in the range of the satellite-based estimates, albeit on the higher side. The most notable differences between the simulated and satellite-based estimates are found for the Ronne and Brunt polynya regions. Differences in the landmasks between the model and satellite data as well as the representation of fast ice in the model are the likely reasons for some of these differences. Both the observed distribution of watermasses and the main observed HSSW production sites are well represented in the reference simulation. However, the simulated watermasses are saltier than the observations. Furthermore, the results indicate the prevalence of the locally produced HSSW over Ronne-sourced ISW on the Filchner ice front between 2002–2017.

In Chapter 4, I investigated the impact both of the regionally downscaled atmospheric forcing (**O1**) and the stationary icescape features (**O2**) on the surface freshwater flux in the southern Weddell Sea by conducting a sensitivity experiment using a coarser reanalysis product as atmospheric forcing and an experiment without the representation of the variable ice bridge.

I found that the regional distribution and variability of sea ice production depend both on the regional atmospheric forcing and on the representation of the stationary icescape features. Representation of the variable ice bridge between Berkner Island and the grounded iceberg A23-A is important for a realistic simulation of polynyas that form west of it and suppresses the sea ice production eastward of it. Furthermore, using high-resolution regional atmospheric forcing leads to more realistic polynya ice production over the eastern continental shelves due to weaker offshore winds. Changes in the ice production are reflected in the HSSW production, which in turn drives noticeable changes in the sub-ice shelf circulation of the Filchner-Ronne system as follows. The density and HSSW production on the eastern part of the continental shelf reduce in the presence of the ice bridge. Due to the weaker HSSW inflow under the Filchner Ice Shelf, the basal melt under the Filchner Ice Shelf is reduced. The model simulation forced with the regional atmospheric forcing and including representation of the icescape represents well the important features of observed interannual variability in surface freshwater flux and oceanic circulation on the southern Weddell Sea continental shelf. This includes the observed increase in sea ice production between

2015 and 2017, which was followed by the intensification of sub-ice shelf cavity circulation. The results further indicate that without the presence of the fast-ice bridge, the simulated circulation under FRIS favors the Berkner mode and the ice bridge can influence transitions between the Ronne and Berkner sub-ice shelf circulation modes.

Furthermore, I used fast ice, sea ice, and hydrographic data from the southern Weddell Sea continental shelf to constrain the model and produce an optimal simulation in Chapter 5. The adapted initial conditions improved the ocean conditions by reducing the temperature-salinity bias on the continental shelf. The representation of the fast ice climatology and the variable ice bridge between Berkner Island and the grounded iceberg A23-A are important for the realistic simulations of the sea ice concentration and ocean salinity on the southern Weddell Sea continental shelf. The nine sea ice model parameters were constrained using Green's functions approach which resulted in further improvements of ice and ocean states in the southern Weddell Sea (**O3**). The sea ice production in the optimized simulation represents all the key advantages of the reference experiment from Chapter 3 when it comes to the regional distribution of ice production in coastal polynyas compared to the sensitivity experiments from Chapter 4. However, both the improved fast ice representation and the optimization of sea ice parameters act to reduce the sea ice production estimates when compared to the reference simulation. While optimization does not affect significantly the variability of sea ice production, it brings the regional sea ice production distribution and strength closer to the satellite-based estimates. This results in the lower densities of the HSSW produced on the southern Weddell Sea continental shelf with the properties closer to observations.

The surface freshwater flux in the southern Weddell Sea is sensitive to perturbations of sea ice model parameters and sensitivity experiments discussed in this thesis can offer guidance for model tuning in future studies. The results show that the optimization of a small number of chosen sea ice model parameters can yield an improved southern Weddell Sea surface freshwater estimates. However, the modest achieved improvements of large-scale sea ice features point to the limitations of the optimization approach in this thesis. Future attempts to optimize Weddell Sea simulations could benefit from a further investigation of model sensitivity to the ocean parameters, such as the horizontal diffusivity parameter which is identified in this study as important for setting the sea ice edge.

To conclude, although large-scale atmospheric fields determine the sea ice production outside polynyas, the treatment of the stationary icescape and the regional atmospheric forcing are important for the regional patterns of sea ice production in polynyas. The representation of the ice bridge is crucial for the simulation of polynyas westward/eastward of it, which are otherwise suppressed/overestimated. Compared to using ERA-Interim reanalysis as an atmospheric forcing dataset, using CCLM output reduces polynya-based ice production over the eastern continental shelf due to weaker offshore winds, bringing results closer to the satellite-based estimates. The improved fast ice representation and the optimization of sea ice parameters reduce further the sea ice production in major polynya, yielding a more realistic representation of ice production within polynyas. Furthermore, based on the results from this thesis, it can be concluded that the location, and not just the strength of the sea ice production in polynyas, is a relevant parameter in setting the properties of the HSSW produced on the continental shelf, which in turn affects the basal melting of the Filchner-Ronne Ice Shelf.

6.2 Outlook

The presence of the coldest ISW representative of the Ronne mode in the hydrographic conditions on the Filchner Ice Shelf ice front remains a caveat in this study. The issue could be linked to the processes in the cavity and transport of water masses within the cavity and should be explored more by investigating the sensitivities of the ice shelf model. The changes in the basal melt related to changes in the surface freshwater flux on the continental shelf are primarily density driven (Nicholls & Østerhus 2004, Hattermann et al. 2021). Therefore, the lack of tides in the model does not affect the conclusions of this study. However, including tides in the model affects the mixing processes (Hausmann et al. 2020) and has a potential to yield the more realistic basal melt rates as well.

The findings of this thesis show that the properties of dense shelf water, which sources Weddell Sea Deep Water and has an impact on modified Warm Deep Water, are influenced by changes in the surface freshwater flux resulting from modifications in the representation of stationary ice cover and sea ice model parameters. However, the settings of the experiments analyzed in this study (e.g. horizontal and vertical resolution, duration of the

experiment) were not constructed to follow the influence of the dense shelf water on the water masses outside of the continental shelf. Therefore, the ability to assess the effects of the changes in the surface freshwater flux on the large-scale Weddell Sea circulation and bottom water production in this study was limited. Future studies that will be able to adequately represent these processes while also realistically representing the surface freshwater flux on the southern Weddell Sea continental shelf will have an opportunity to tackle this question.

More significant calving off the Filchner Ice Shelf in the future might lead to a more permanent ice bridge. In contrast, the recent calving from the Brunt and Ronne ice shelves (Christie et al. 2022), as well as the recent movement of the iceberg A23-A exposed new areas to polynya development. The results from this thesis emphasize the importance of representing the relevant properties of the dynamic icescape for realistic simulations of the sea ice–ocean–ice shelf system in the region. Seasonally and interannually varying fast-ice data along the whole southern Weddell Sea coastline would be beneficial to future studies of ice production within polynyas.

A. Complementary Figures

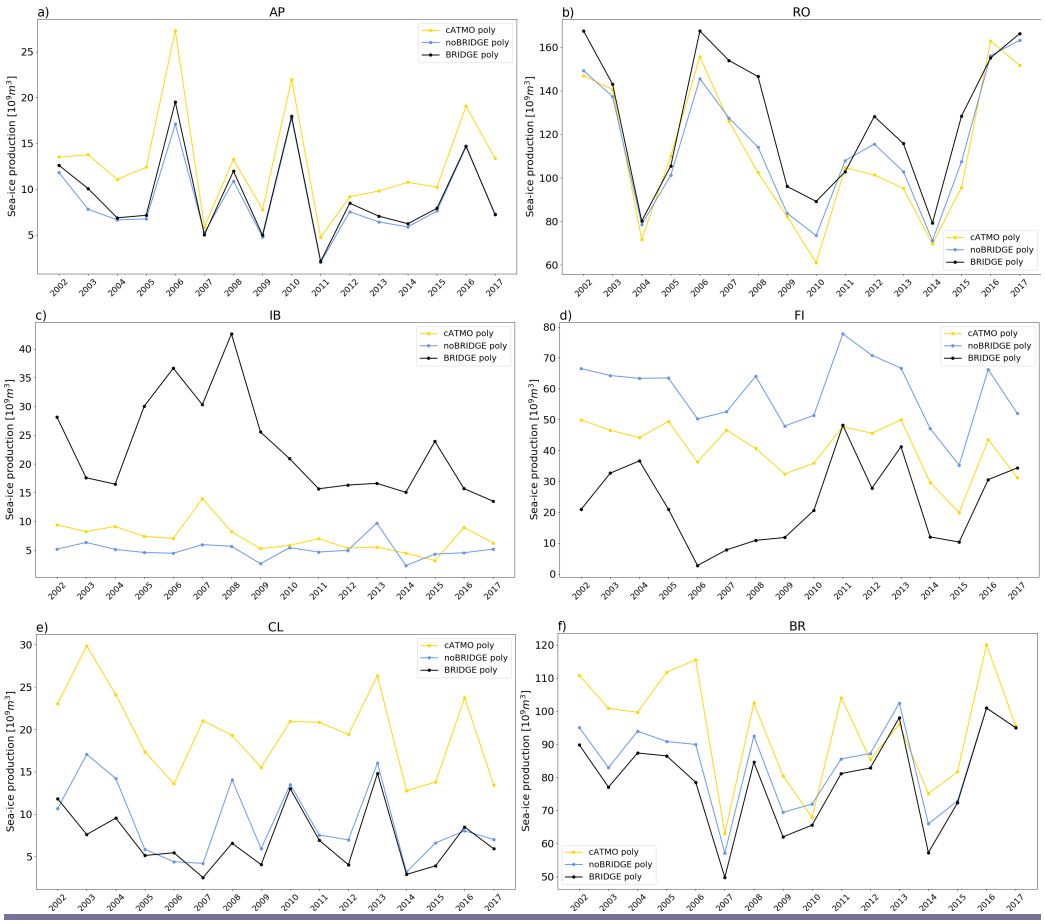

Figure A.1: Time-series of the cumulative polynya ice-production (2002–2017) in the southern Weddell Sea from the FESOM experiments for the six sub-regions shown in Fig. 2.3.

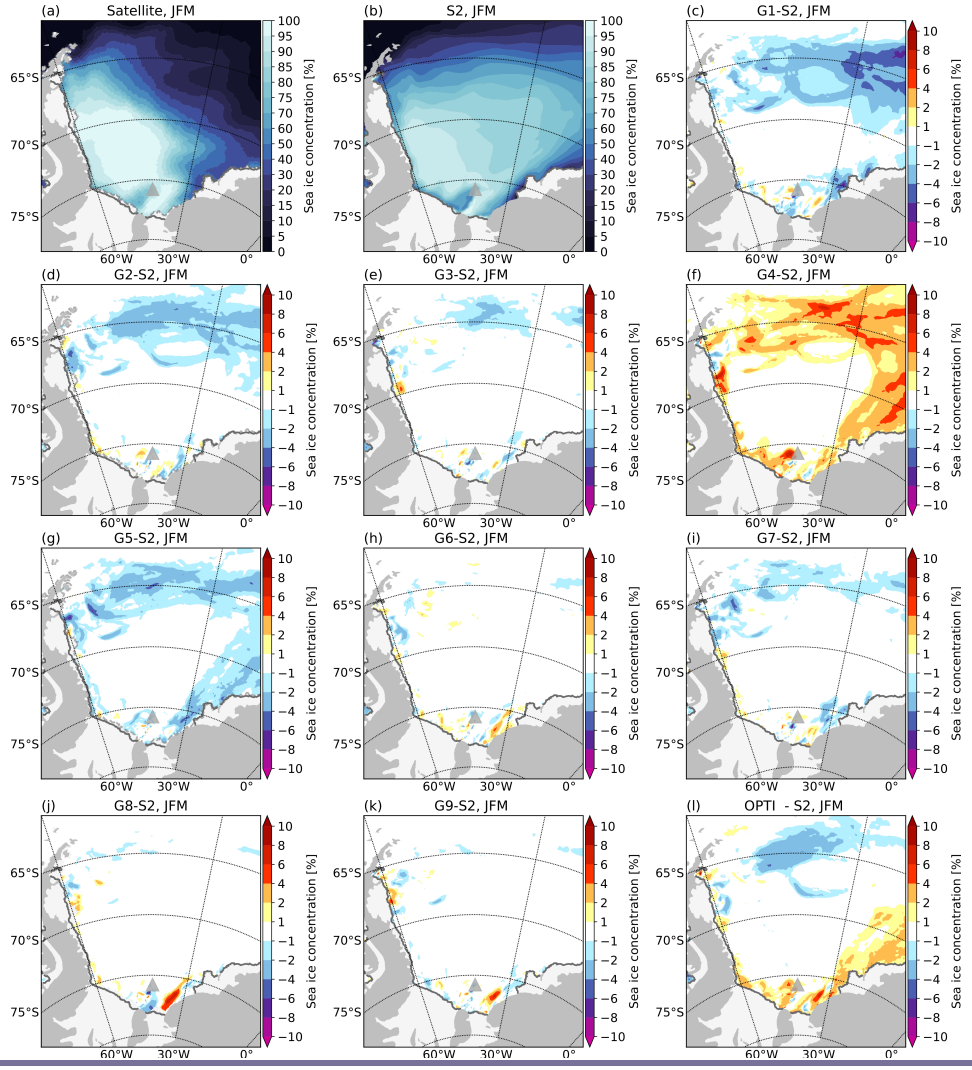

Figure A.2: (a) Summer mean (JFM, 2002–2011) sea ice concentration over the Weddell Sea from the satellite data (a), the experiment S2 (b), difference in sea ice concentration between G1–G9 and S2 (c–k), and difference between OPTI and S2(l). The solid gray line in all panels and the dashed gray line in panel (a) contour the ice shelf edge from the model and the data, respectively. The location of the grounded iceberg A23-A (2002–2011) is marked by a triangle.

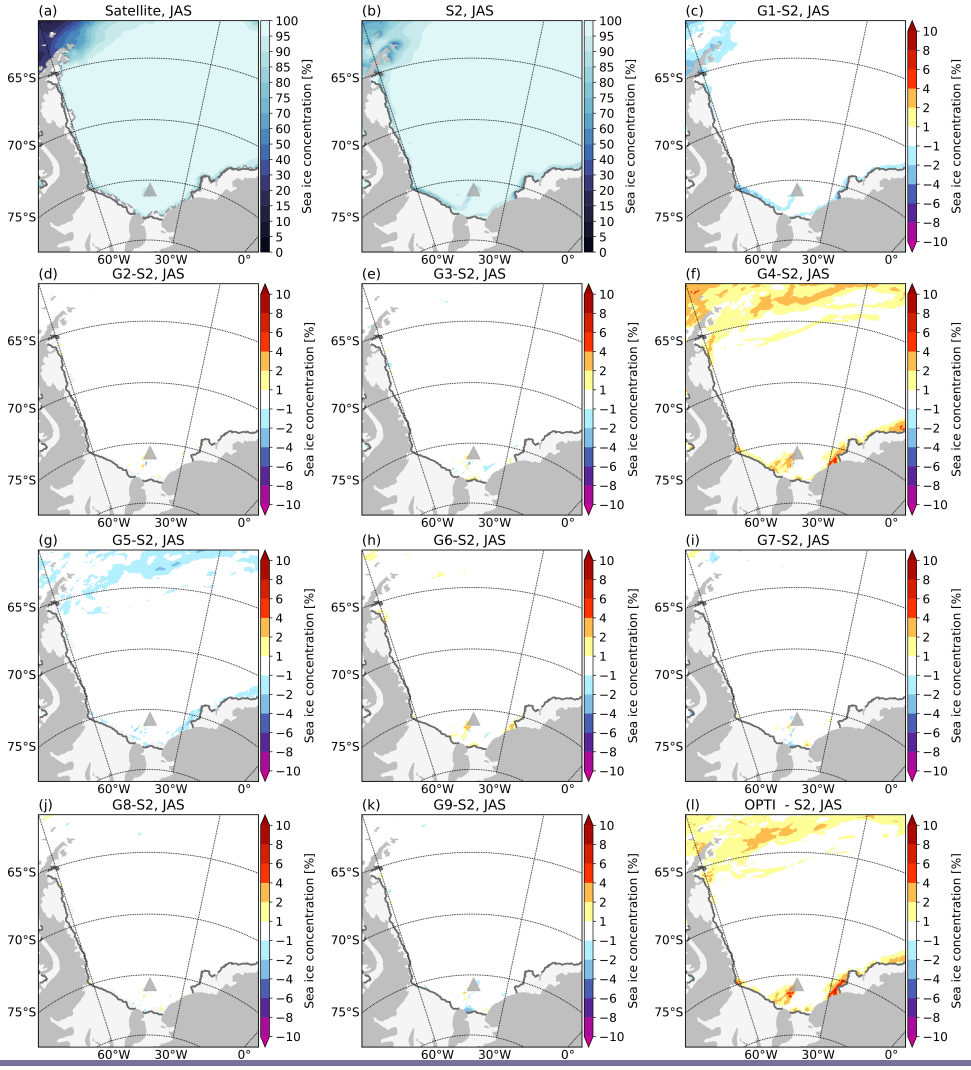

Figure A.3: (a) Winter mean (JAS, 2002–2011) sea ice concentration over the Weddell Sea from the satellite data (a), the experiment S2 (b), difference in sea ice concentration between G1–G9 and S2 (c–k), and difference between OPTI and S2(l). The solid gray line in all panels and the dashed gray line in panel (a) contour the ice shelf edge from the model and the data, respectively. The location of the grounded iceberg A23-A (2002–2011) is marked by a triangle.

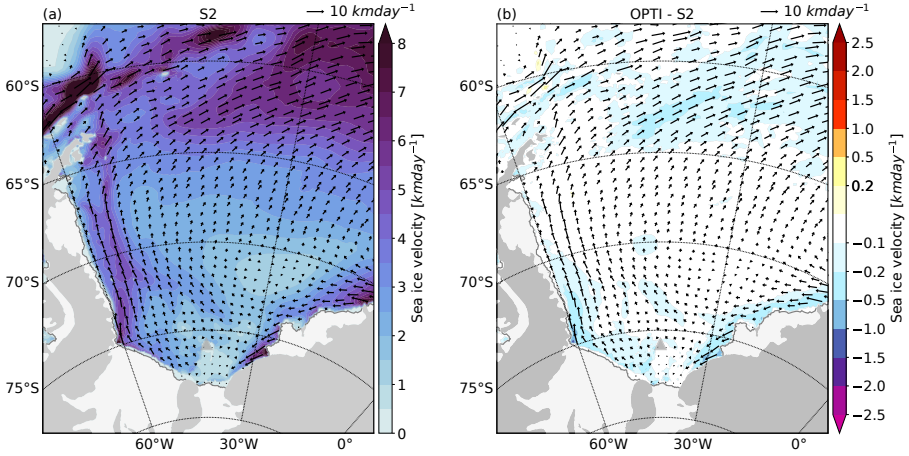

Figure A.4: (a) Mean (2002–2011) sea ice velocity (arrows and color shading) for (a) S2 and (b) OPTI (arrows) and difference in sea ice speed between S2 and OPTI (color shading). The solid gray contours the ice shelf edge. The location of the grounded iceberg A23-A (2002–2011) is marked by a triangle.

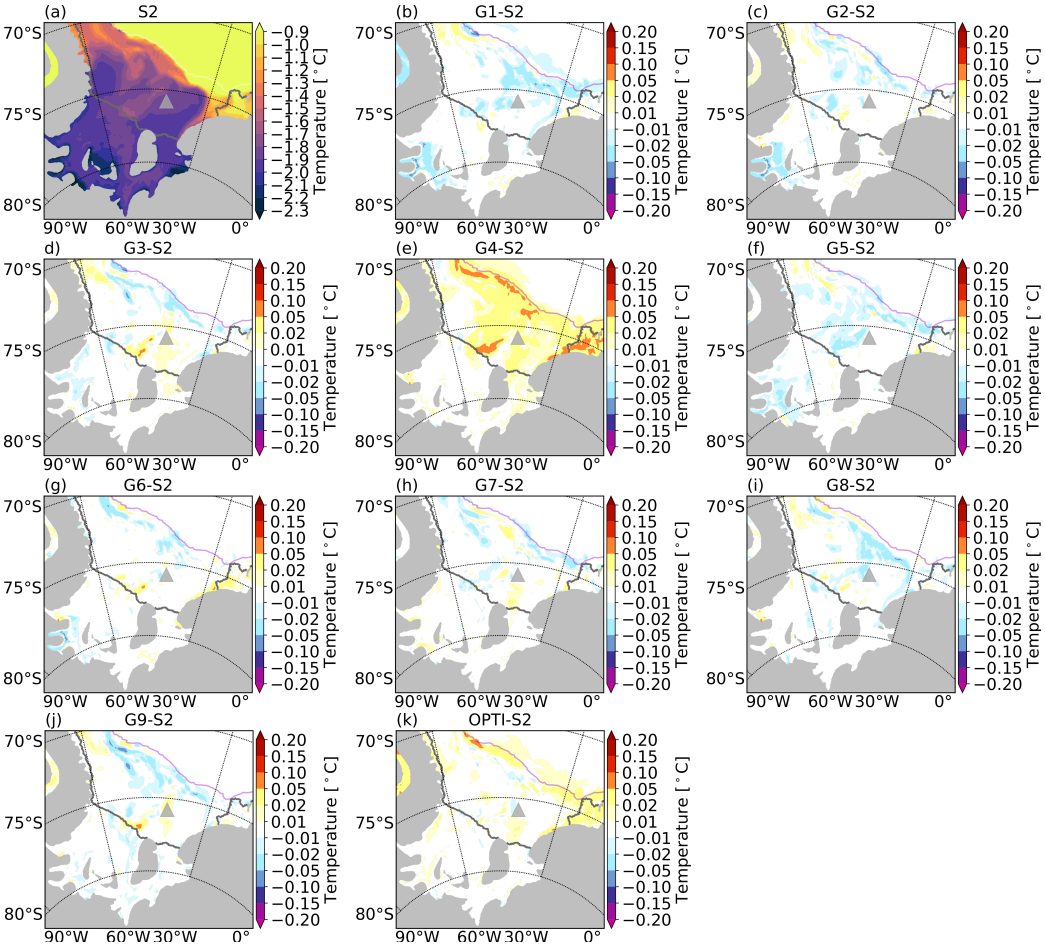

Figure A.5: (a) Mean (2002–2011) bottom temperature (θ) from S2 (a). The ice shelf edge is indicated by a gray contour, and the 2500 m isobath is marked by a white contour. Difference (2002–2011) in the mean bottom temperature (θ) between G1–9 and S2 (b–j) and difference between OPTI and S2 (k). The ice shelf edge is indicated by a gray contour, and the 2500 m isobath is marked by a violet contour. The location of the grounded iceberg A23-A (2002–2011) is marked by a triangle in all panels.

Acknowledgments

A.1 AI transparency statement

The text in this thesis has not been generated, improved or suggested by AI. The grammar and spelling have been corrected with the help of AI, but with manual decisions about which corrections will be accepted or rejected.

A.2 Resources and funding

The research for this thesis has been done at the Alfred Wegener Institute in the Physical oceanography section. HLRN supercomputing center provided the computational time for FESOM simulations under project ID hbk00034. This research was supported by the SPP 1158 "Antarctic research" of the DFG (Deutsche Forschungsgemeinschaft) under grants HE 2740/19, JU 2972/1 and TI 296/6. Research stay abroad at NASA/JPL through the JPL Visiting Student Research Program was supported by the POLMAR outgoing scholarship.

A.3 Acknowledgments

I owe a debt of gratitude to Torsten Kanzow for supporting me as a PhD candidate. This thesis would not have been finished without your guidance, support and encouragement, especially towards the end of my PhD. A special thanks to my supervisor Ralph Timmermann for all the help and support. Thank you for helping me to learn "speaking FESOM" and teaching me that good modeling benefits from an observational eye. Thank you Torsten and Ralph for suffering through all the missing, wrong, and unnecessary articles in my writing. More importantly, I am thankful for your feedback and comments which have helped me to think and write better.

I am grateful to Yoshihiro Nakayama for his help and enthusiasm, especially during my research stay at JPL. Thank you for your motivation, comments, and teaching me the importance of model-data synergy. I am thankful to Günther Heinemann, Rolf Zentek and Stephan Paul for the great collaboration on the project. For interesting discussions and valuable insights, I am grateful to: Sergey Danilov for helping me to understand the inner workings of the model, Hartmut Hellmer for sharing his vast knowledge on the Weddell Sea, and Dimitris Menemenlis for teaching me the great value of wrong models. Thanks to Dmitry Sidorenko and Claudia Wekerle for the support with FESOM. I am grateful as well to Christian Haas for agreeing to be the reviewer.

Thank you Thomas Rackow for many discussions and useful Python hacks. Many thanks to Svenja Ryan, Mathias Van Caspel and Nicolas le Peih for providing the oceanographic perspective, you were great colleagues to me.

To my family and friends, thank you for always being there for me.

List of Figures

List of Tables

B. Abbreviations

Table B.1: Abbreviations

AABW	Antarctic Bottom Water
ASF	Antarctic Slope Front
AWI	Alfred Wegener Institut
BRIDGE	FESOM simulation (2002–2017) forced with COSMO-CLM forcing, and including effects of the ice bridge
cATMO	FESOM simulation (2002–2017) forced with ERA-Interim forcing
CCLM	COSMO-CLM
CTD	Conductivity Temperature Depth Profiles measurements
ERA	ERA-Interim reanalysis
EVP	elastic–viscous–plastic (model for sea ice dynamics)
FAST	FESOM simulation (1979–2001) forced with ERA-Interim forcing, and including effects of fast ice
FEM	finite element method
FESOM	Finite Element Sea ice-Ocean Model
FIS	The Filchner Ice Shelf
FRIS	The Filchner-Ronne Ice Shelf
G1–9	FESOM experiments used for the Green's functions optimization
GCM	General Circulation Model
GF	Green's functions
GM	mesoscale ´eddie parameterization (Gent & Mcwilliams 1990, Gent et al. 1995)
HSSW	High Salinity Shelf Water
ISW	Ice Shelf Water

Continued on next page

Table B.1 – *Continued from previous page*

KPP	K-Profile Parameterization
lERA	FESOM simulation (1979–2001) forced with ERA-Interim forcing
MGT	Mertz Glacier Tongue
MODIS	Moderate Resolution Imaging Spectroradiometer
mWDW	modified Warm Deep Water
noBRIDGE	FESOM simulation (2002–2017) forced with COSMO-CLM forcing
OPTI	optimized FESOM simulation (2002–2017)
P-E	difference between precipitation and evaporation
S1,2	FESOM simulations used in the optimization approach
statBRIDGE	the FESOM experiment (2015–2017) with the static ice bridge
WS	Weddell Sea

Bibliography

Abernathey, R. P., Cerovecki, I., Holland, P. R., Newsom, E., Mazloff, M. & Talley, L. D. (2016), 'Water-mass transformation by sea ice in the upper branch of the southern ocean overturning', *Nature Geoscience* **9**(8), 596.

Adusumilli, S., Fricker, H. A., Medley, B., Padman, L. & Siegfried, M. R. (2020), 'Interannual variations in meltwater input to the southern ocean from antarctic ice shelves', *Nature geoscience* **13**(9), 616–620.

Akhoudas, C. H., Sallée, J.-B., Haumann, F. A., Meredith, M. P., Garabato, A. N., Reverdin, G., Jullion, L., Aloisi, G., Benetti, M., Leng, M. J. et al. (2021), 'Ventilation of the abyss in the atlantic sector of the southern ocean', *Scientific Reports* **11**(1), 6760.

Batrak, Y. & Müller, M. (2019), 'On the warm bias in atmospheric reanalyses induced by the missing snow over arctic sea-ice', *Nature Communications* **10**(1), 1–8.

Budge, J. S. & Long, D. G. (2018), 'A comprehensive database for antarctic iceberg tracking using scatterometer data', *IEEE Journal of Selected Topics in Applied Earth Observations and Remote Sensing* **11**(2), 434–442.

Cavalieri, D. J., Gloersen, P. & Campbell, W. J. (1984), 'Determination of sea ice parameters with the nimbus 7 smmr', *Journal of Geophysical Research: Atmospheres* **89**(D4), 5355–5369.

Christie, F. D., Benham, T. J., Batchelor, C. L., Rack, W., Montelli, A. & Dowdeswell, J. A. (2022), 'Antarctic ice-shelf advance driven by anomalous atmospheric and sea-ice circulation', *Nature Geoscience* **15**(5), 356–362.

Comiso, J. (1986), 'Characteristics of arctic winter sea ice from satellite multispectral microwave observations', *Journal of Geophysical Research: Oceans* **91**(C1), 975–994.

Cougnon, E., Galton-Fenzi, B., Rintoul, S., Legrésy, B., Williams, G., Fraser, A. & Hunter, J. (2017), 'Regional changes in icescape impact shelf circulation and basal melting', *Geophysical Research Letters* **44**(22), 11–519.

Daae, K., Hattermann, T., Darelius, E., Mueller, R. D., Naughten, K. A., Timmermann, R. & Hellmer, H. H. (2020), 'Necessary conditions for warm inflow toward the filchner ice shelf, weddell sea', *Geophysical Research Letters* **47**(22), e2020GL089237.

Danilov, S., Kivman, G. & Schröter, J. (2004), 'A finite-element ocean model: principles and evaluation', *Ocean Modelling* **6**(2), 125–150.

Danilov, S., Wang, Q., Timmermann, R., Iakovlev, N., Sidorenko, D., Kimmritz, M., Jung, T. & Schröter, J. (2015), 'Finite-element sea ice model (fesim), version 2', *Geoscientific Model Development* **8**(6), 1747–1761.

Darelius, E., Fer, I. & Nicholls, K. (2016), 'Observed vulnerability of filchner-ronne ice shelf to wind-driven inflow of warm deep water, nat. commun., 7, 12300'.

Dee, D. P., Uppala, S., Simmons, A., Berrisford, P., Poli, P., Kobayashi, S., Andrae, U., Balmaseda, M., Balsamo, G., Bauer, d. P. et al. (2011), 'The era-interim reanalysis: Configuration and performance of the data assimilation system', *Quarterly Journal of the royal meteorological society* **137**(656), 553–597.

Dettling, N., Losch, M., Pollmann, F. & Kanzow, T. (2023), 'Towards parameterizing eddy-mediated transport of warm deep water across the weddell sea continental slope'.

Diamond, R., Sime, L. C., Holmes, C. R. & Schroeder, D. (2024), 'Cmip6 models rarely simulate antarctic winter sea-ice anomalies as large as observed in 2023', *Geophysical Research Letters* **51**(10), e2024GL109265.

Dieckmann, G. S. & Hellmer, H. H. (2003), 'The importance of sea ice: an overview', *Sea ice: An introduction to its physics, chemistry, biology and geology* pp. 1–21.

Dinniman, M. S., Klinck, J. M., Bai, L.-S., Bromwich, D. H., Hines, K. M. & Holland, D. M. (2015), 'The effect of atmospheric forcing resolution

on delivery of ocean heat to the antarctic floating ice shelves', *Journal of Climate* **28**(15), 6067–6085.

Drucker, R., Martin, S. & Kwok, R. (2011), 'Sea ice production and export from coastal polynyas in the weddell and ross seas', *Geophysical Research Letters* **38**(17).

Ebner, L., Heinemann, G., Haid, V. & Timmermann, R. (2014), 'Katabatic winds and polynya dynamics at coats land, antarctica', *Antarctic Science* **26**(3), 309–326.

Foldvik, A., Gammelsrød, T. & Tørresen, T. (1985), 'Circulation and water masses on the southern weddell sea shelf', *Oceanology of the Antarctic continental shelf* **43**, 5–20.

Foster, T. D. & Carmack, E. C. (1976), Frontal zone mixing and antarctic bottom water formation in the southern weddell sea, *in* 'Deep Sea Research and Oceanographic Abstracts', Vol. 23, Elsevier, pp. 301–317.

Gent, P. R. & Mcwilliams, J. C. (1990), 'Isopycnal mixing in ocean circulation models', *Journal of Physical Oceanography* **20**(1), 150–155.

Gent, P. R., Willebrand, J., McDougall, T. J. & McWilliams, J. C. (1995), 'Parameterizing eddy-induced tracer transports in ocean circulation models', *Journal of Physical Oceanography* **25**(4), 463–474.

Gilbert, E. & Holmes, C. (2024), '2023's antarctic sea ice extent is the lowest on record', *Weather* .

Grosfeld, K., Schröder, M., Fahrbach, E., Gerdes, R. & Mackensen, A. (2001), 'How iceberg calving and grounding change the circulation and hydrography in the filchner ice shelf-ocean system', *Journal of Geophysical Research: Oceans* **106**(C5), 9039–9055.

Gutjahr, O., Heinemann, G., Preußer, A., Willmes, S. & Drüe, C. (2016), 'Quantification of ice production in laptev sea polynyas and its sensitivity to thin-ice parameterizations in a regional climate model', *The Cryosphere* **10**(6), 2999–3019.

Haid, V. & Timmermann, R. (2013), 'Simulated heat flux and sea ice production at coastal polynyas in the southwestern weddell sea', *Journal of Geophysical Research: Oceans* **118**(5), 2640–2652.

Haid, V., Timmermann, R., Ebner, L. & Heinemann, G. (2015), 'Atmospheric forcing of coastal polynyas in the south-western weddell sea', *Antarctic Science* **27**(4), 388–402.

Hall, D. & Riggs, G. (2015), 'Modis/aqua sea ice extent 5-min l2 swath 1km, version 6', *Boulder, Colorado USA. NASA National Snow and Ice Data Center Distributed Active Archive Center. doi: http://dx. doi. org/10.5067/MODIS/MYD29* **6**.

Hattermann, T., Nicholls, K. W., Hellmer, H. H., Davis, P. E., Janout, M. A., Østerhus, S., Schlosser, E., Rohardt, G. & Kanzow, T. (2021), 'Observed interannual changes beneath filchner-ronne ice shelf linked to large-scale atmospheric circulation', *Nature communications* **12**(1), 1–11.

Haumann, F. A., Gruber, N., Münnich, M., Frenger, I. & Kern, S. (2016), 'Sea-ice transport driving southern ocean salinity and its recent trends', *Nature* **537**(7618), 89.

Hausmann, U., Sallée, J.-B., Jourdain, N., Mathiot, P., Rousset, C., Madec, G., Deshayes, J. & Hattermann, T. (2020), 'The role of tides in ocean-ice shelf interactions in the southwestern weddell sea', *Journal of Geophysical Research: Oceans* **125**(6), e2019JC015847.

Hazel, J. E. & Stewart, A. L. (2020), 'Bistability of the filchner-ronne ice shelf cavity circulation and basal melt', *Journal of Geophysical Research: Oceans* **125**(4), e2019JC015848.

Heinemann, G., Schefczyk, L., Willmes, S. & Shupe, M. D. (2022), 'Evaluation of simulations of near-surface variables using the regional climate model cclm for the mosaic winter period', *Elementa* **10**(1).

Heinemann, G., Willmes, S., Schefczyk, L., Makshtas, A., Kustov, V. & Makhotina, I. (2021), 'Observations and simulations of meteorological conditions over arctic thick sea ice in late winter during the transarktika 2019 expedition', *Atmosphere* **12**(2), 174.

Heinemann, G. & Zentek, R. (2021), 'A model-based climatology of low-level jets in the weddell sea region of the antarctic', *Atmosphere* **12**(12), 1635.

Hellmer, H. H., Kauker, F., Timmermann, R. & Hattermann, T. (2017), 'The fate of the southern weddell sea continental shelf in a warming climate', *Journal of Climate* **30**(12), 4337–4350.

Hellmer, H. H. & Olbers, D. J. (1989), 'A two-dimensional model for the thermohaline circulation under an ice shelf', *Antarctic Science* **1**(4), 325–336.

Hibler, W. (1979), 'A dynamic thermodynamic sea ice model', *Journal of physical oceanography* **9**(4), 815–846.

Holland, D. M. & Jenkins, A. (1999), 'Modeling thermodynamic ice–ocean interactions at the base of an ice shelf', *Journal of Physical Oceanography* **29**(8), 1787–1800.

Hoppmann, M., Richter, M. E., Smith, I. J., Jendersie, S., Langhorne, P. J., Thomas, D. N. & Dieckmann, G. S. (2020), 'Platelet ice, the southern ocean's hidden ice: a review', *Annals of Glaciology* **61**(83), 341–368.

Hunke, E. C. & Dukowicz, J. K. (1997), 'An elastic–viscous–plastic model for sea ice dynamics', *Journal of Physical Oceanography* **27**(9), 1849–1867.

Janout, M. A., Hellmer, H. H., Hattermann, T., Huhn, O., Sültenfuss, J., Østerhus, S., Stulic, L., Ryan, S., Schröder, M. & Kanzow, T. (2021), 'Fris revisited in 2018: On the circulation and water masses at the filchner and ronne ice shelves in the southern weddell sea', *Journal of Geophysical Research: Oceans* **126**(6), e2021JC017269.

Jenkins, A. (1991), 'A one-dimensional model of ice shelf-ocean interaction', *Journal of Geophysical Research: Oceans* **96**(C11), 20671–20677.

Kusahara, K., Hasumi, H., Fraser, A. D., Aoki, S., Shimada, K., Williams, G. D., Massom, R. & Tamura, T. (2017), 'Modeling ocean–cryosphere interactions off adélie and george v land, east antarctica', *Journal of Climate* **30**(1), 163–188.

Kusahara, K., Hasumi, H. & Tamura, T. (2010), 'Modeling sea ice production and dense shelf water formation in coastal polynyas around east antarctica', *Journal of Geophysical Research: Oceans* **115**(C10).

Kusahara, K., Hasumi, H. & Williams, G. (2011), 'Impact of the mertz glacier tongue calving on dense water formation and export, nat. commun., 2, 159'.

Kwok, R., Pang, S. S. & Kacimi, S. (2017), 'Sea ice drift in the southern ocean: Regional patterns, variability, and trends', *Elem Sci Anth* **5**.

Large, W. G., McWilliams, J. C. & Doney, S. C. (1994), 'Oceanic vertical mixing: A review and a model with a nonlocal boundary layer parameterization', *Reviews of Geophysics* **32**(4), 363–403.

Lemarié, F., Kurian, J., Shchepetkin, A. F., Molemaker, M. J., Colas, F. & McWilliams, J. C. (2012), 'Are there inescapable issues prohibiting the use of terrain-following coordinates in climate models?', *Ocean Modelling* **42**, 57–79.

Levitus, S., Locarnini, R. A., Boyer, T. P., Mishonov, A. V., Antonov, J. I., Garcia, H. E., Baranova, O. K., Zweng, M. M., Johnson, D. R. & Seidov, D. (2010), 'World ocean atlas 2009'.

Losch, M., Menemenlis, D., Campin, J.-M., Heimbach, P. & Hill, C. (2010), 'On the formulation of sea-ice models. part 1: Effects of different solver implementations and parameterizations', *Ocean Modelling* **33**(1-2), 129–144.

Luckman, A., Padman, L. & Jansen, D. (2010), 'Persistent iceberg groundings in the western weddell sea, antarctica', *Remote Sensing of Environment* **114**(2), 385–391.

Maqueda, M. M., Willmott, A. & Biggs, N. (2004), 'Polynya dynamics: A review of observations and modeling', *Reviews of Geophysics* **42**(1).

Markus, T. (1996), The effect of the grounded tabular icebergs in front of berkner island on the weddell sea ice drift as seen from satellite passive microwave sensors, *in* 'IGARSS'96. 1996 International Geoscience and Remote Sensing Symposium', Vol. 3, IEEE, pp. 1791–1793.

Massom, R. A., Eicken, H., Hass, C., Jeffries, M. O., Drinkwater, M. R., Sturm, M., Worby, A. P., Wu, X., Lytle, V. I., Ushio, S. et al. (2001), 'Snow on antarctic sea ice', *Reviews of Geophysics* **39**(3), 413–445.

Massom, R., Harris, P., Michael, K. J. & Potter, M. (1998), 'The distribution and formative processes of latent-heat polynyas in east antarctica', *Annals of Glaciology* **27**, 420–426.

Mathiot, P., Barnier, B., Gallée, H., Molines, J. M., Le Sommer, J., Juza, M. & Penduff, T. (2010), 'Introducing katabatic winds in global era40 fields to

simulate their impacts on the southern ocean and sea-ice', *Ocean Modelling* **35**(3), 146–160.

Meier, W. N., Fetterer, F., Savoie, M., Mallory, S., Duerr, R. & Stroeve, J. (2017), 'Noaa/nsidc climate data record of passive microwave sea ice concentration, version 3. southern hemisphere. boulder, colorado usa. nsidc: National snow and ice data center. [july 8, 2019]'. data available at: `https://nsidc.org/data/g02202/versions/3`.

Mellor, G. L., Ezer, T. & Oey, L.-Y. (1994), 'The pressure gradient conundrum of sigma coordinate ocean models', *Journal of atmospheric and oceanic technology* **11**(4), 1126–1134.

Menemenlis, D., Fukumori, I. & Lee, T. (2005), 'Using green's functions to calibrate an ocean general circulation model', *Monthly weather review* **133**(5), 1224–1240.

Miller, P. A., Laxon, S. W., Feltham, D. L. & Cresswell, D. J. (2006), 'Optimization of a sea ice model using basinwide observations of arctic sea ice thickness, extent, and velocity', *Journal of Climate* **19**(7), 1089–1108.

Moholdt, G., Padman, L. & Fricker, H. A. (2014), 'Basal mass budget of ross and filchner-ronne ice shelves, antarctica, derived from lagrangian analysis of icesat altimetry', *Journal of Geophysical Research: Earth Surface* **119**(11), 2361–2380.

Nakayama, Y., Menemenlis, D., Schodlok, M. & Rignot, E. (2017), 'Amundsen and b ellingshausen s eas simulation with optimized ocean, sea ice, and thermodynamic ice shelf model parameters', *Journal of Geophysical Research: Oceans* **122**(8), 6180–6195.

Nakayama, Y., Timmermann, R., Schröder, M. & Hellmer, H. H. (2014), 'On the difficulty of modeling circumpolar deep water intrusions onto the amundsen sea continental shelf', *Ocean Modelling* **84**, 26–34.

Naughten, K. A., De Rydt, J., Rosier, S. H., Jenkins, A., Holland, P. R. & Ridley, J. K. (2021), 'Two-timescale response of a large antarctic ice shelf to climate change', *Nature communications* **12**(1), 1–10.

Naughten, K. A., Meissner, K. J., Galton-Fenzi, B. K., England, M. H., Timmermann, R., Hellmer, H. H., Hattermann, T. & Debernard, J. B.

(2018), 'Intercomparison of antarctic ice-shelf, ocean, and sea-ice interactions simulated by metroms-iceshelf and fesom 1.4', *Geoscientific Model Development* **11**(4), 1257–1292.

Nguyen, A., Menemenlis, D. & Kwok, R. (2009), 'Improved modeling of the arctic halocline with a subgrid-scale brine rejection parameterization', *Journal of Geophysical Research: Oceans* **114**(C11).

Nguyen, A. T., Menemenlis, D. & Kwok, R. (2011), 'Arctic ice-ocean simulation with optimized model parameters: Approach and assessment', *Journal of Geophysical Research: Oceans* **116**(C4).

Nicholls, K. W. & Østerhus, S. (2004), 'Interannual variability and ventilation timescales in the ocean cavity beneath filchner-ronne ice shelf, antarctica', *Journal of Geophysical Research: Oceans* **109**(C4).

Nicholls, K. W., Østerhus, S., Makinson, K., Gammelsrød, T. & Fahrbach, E. (2009), 'Ice-ocean processes over the continental shelf of the southern weddell sea, antarctica: A review', *Reviews of Geophysics* **47**(3).

Nihashi, S. & Ohshima, K. I. (2015*a*), 'Circumpolar mapping of antarctic coastal polynyas and landfast sea ice: Relationship and variability', *Journal of climate* **28**(9), 3650–3670.

Nihashi, S. & Ohshima, K. I. (2015*b*), 'Circumpolar mapping of antarctic coastal polynyas and landfast sea ice: Relationship and variability', *Journal of climate* **28**(9), 3650–3670.

Nøst, O. A. & Østerhus, S. (1985), 'Impact of grounded icebergs on the hydrographic conditions near the filchner ice shelf', *Ocean, Ice, and atmosphere: Interactions at the Antarctic continental margin* **75**, 267–284.

Orsi, A. H., Johnson, G. C. & Bullister, J. L. (1999), 'Circulation, mixing, and production of antarctic bottom water', *Progress in Oceanography* **43**(1), 55–109.

Owens, W. B. & Lemke, P. (1990), 'Sensitivity studies with a sea ice-mixed layer-pycnocline model in the weddell sea', *Journal of Geophysical Research: Oceans* **95**(C6), 9527–9538.

Paolo, F. S., Fricker, H. A. & Padman, L. (2015), 'Volume loss from antarctic ice shelves is accelerating', *Science* **348**(6232), 327–331.

Parkinson, C. L. (2019), 'A 40-y record reveals gradual antarctic sea ice increases followed by decreases at rates far exceeding the rates seen in the arctic', *Proceedings of the National Academy of Sciences* **116**(29), 14414–14423.

Parkinson, C. L. & Washington, W. M. (1979), 'A large-scale numerical model of sea ice', *Journal of Geophysical Research: Oceans* **84**(C1), 311–337.

Paul, S., Willmes, S. & Heinemann, G. (2015), 'Long-term coastal-polynya dynamics in the southern weddell sea from modis thermal-infrared imagery', *The Cryosphere* **9**(6), 2027–2041.

Pellichero, V., Sallée, J.-B., Chapman, C. C. & Downes, S. M. (2018), 'The southern ocean meridional overturning in the sea-ice sector is driven by freshwater fluxes', *Nature communications* **9**(1), 1789.

Peng, G., Meier, W., Scott, D. & Savoie, M. (2013), 'A long-term and reproducible passive microwave sea ice concentration data record for climate studies and monitoring', *Earth System Science Data* **5**(2), 311–318.

Purich, A. & Doddridge, E. (2023), 'Record low antarctic sea ice coverage indicates a new sea ice state. communications earth and environment, 4 (1), 314'.

Rackow, T., Wesche, C., Timmermann, R., Hellmer, H. H., Juricke, S. & Jung, T. (2017), 'A simulation of small to giant antarctic iceberg evolution: Differential impact on climatology estimates', *Journal of Geophysical Research: Oceans* **122**(4), 3170–3190.

Redi, M. H. (1982), 'Oceanic isopycnal mixing by coordinate rotation', *Journal of Physical Oceanography* **12**(10), 1154–1158.

Reiser, F., Willmes, S., Hausmann, U. & Heinemann, G. (2019), 'Predominant sea ice fracture zones around antarctica and their relation to bathymetric features', *Geophysical Research Letters* **46**(21), 12117–12124.

Rignot, E., Jacobs, S., Mouginot, J. & Scheuchl, B. (2013), 'Ice-shelf melting around antarctica', *Science* **341**(6143), 266–270.

Rignot, E., Mouginot, J., Scheuchl, B., Van Den Broeke, M., Van Wessem, M. J. & Morlighem, M. (2019), 'Four decades of antarctic ice sheet mass balance from 1979–2017', *Proceedings of the National Academy of Sciences* **116**(4), 1095–1103.

Rockel, B., Will, A. & Hense, A. (2008), 'The regional climate model cosmo-clm (cclm)', *Meteorologische Zeitschrift* **17**(4), 347–348.

Ryan, S. (2018), On the Flow of Modified Warm Deep Water toward the Filchner Ronne Ice Shelf, Weddell Sea, Antarctica, PhD thesis, Universität Bremen.

Ryan, S., Hellmer, H. H., Janout, M., Darelius, E., Vignes, L. & Schröder, M. (2020), 'Exceptionally warm and prolonged flow of warm deep water toward the filchner-ronne ice shelf in 2017', *Geophysical Research Letters* **47**(13), e2020GL088119.

Schaffer, J., Timmermann, R., Arndt, J. E., Kristensen, S. S., Mayer, C., Morlighem, M. & Steinhage, D. (2016), 'A global, high-resolution data set of ice sheet topography, cavity geometry, and ocean bathymetry'.

Scholz, P., Sidorenko, D., Gurses, O., Danilov, S., Koldunov, N., Wang, Q., Sein, D., Smolentseva, M., Rakowsky, N. & Jung, T. (2019), 'Assessment of the finite-volume sea ice-ocean model (fesom2. 0)–part 1: Description of selected key model elements and comparison to its predecessor version', *Geoscientific Model Development* **12**(11), 4875–4899.

Schröder, D., Heinemann, G. & Willmes, S. (2011), 'The impact of a thermodynamic sea-ice module in the cosmo numerical weather prediction model on simulations for the laptev sea, siberian arctic', *Polar Research* **30**(1), 6334.

Spreen, G., Kaleschke, L. & Heygster, G. (2008), 'Sea ice remote sensing using amsr-e 89-ghz channels', *Journal of Geophysical Research: Oceans* **113**(C2).

Steger, C. & Bucchignani, E. (2020), 'Regional climate modelling with cosmo-clm: History and perspectives'.

Stulic, L., Timmermann, R., Paul, S., Zentek, R., Heinemann, G. & Kanzow, T. (2023), 'Southern weddell sea surface freshwater flux modulated by icescape and atmospheric forcing', *Ocean Science* **19**(6), 1791–1808.

Su, Z. (2017), 'Preconditioning of antarctic maximum sea ice extent by upper ocean stratification on a seasonal timescale', *Geophysical Research Letters* **44**(12), 6307–6315.

Tamura, T. & Ohshima, K. I. (2011), 'Mapping of sea ice production in the arctic coastal polynyas', *Journal of Geophysical Research: Oceans* **116**(C7).

Tamura, T., Ohshima, K. I. & Nihashi, S. (2008), 'Mapping of sea ice production for antarctic coastal polynyas', *Geophysical Research Letters* **35**(7).

Thompson, A. F., Stewart, A. L., Spence, P. & Heywood, K. J. (2018), 'The antarctic slope current in a changing climate', *Reviews of Geophysics* **56**(4), 741–770.

Timmermann, R. (2000), Wechselwirkungen zwischen Eis und Ozean im Weddellmeer-Studien mit einem gekoppelten Eis-Ozean-Modell des Südpolarmeeres, PhD thesis, Uni Bremen.

Timmermann, R., Beckmann, A. & Hellmer, H. (2001), 'The role of sea ice in the fresh-water budget of the weddell sea, antarctica', *Annals of Glaciology* **33**, 419–424.

Timmermann, R., Danilov, S., Schröter, J., Böning, C., Sidorenko, D. & Rollenhagen, K. (2009), 'Ocean circulation and sea ice distribution in a finite element global sea ice–ocean model', *Ocean Modelling* **27**(3-4), 114–129.

Timmermann, R. & Hellmer, H. H. (2013), 'Southern ocean warming and increased ice shelf basal melting in the twenty-first and twenty-second centuries based on coupled ice-ocean finite-element modelling', *Ocean Dynamics* **63**(9-10), 1011–1026.

Timmermann, R., Wang, Q. & Hellmer, H. (2012), 'Ice-shelf basal melting in a global finite-element sea-ice/ice-shelf/ocean model', *Annals of Glaciology* **53**(60), 303–314.

Turner, J., Guarino, M. V., Arnatt, J., Jena, B., Marshall, G. J., Phillips, T., Bajish, C., Clem, K., Wang, Z., Andersson, T. et al. (2020), 'Recent decrease of summer sea ice in the weddell sea, antarctica', *Geophysical Research Letters* **47**(11), e2020GL087127.

Uotila, P., Holland, P. R., Vihma, T., Marsland, S. J. & Kimura, N. (2014), 'Is realistic antarctic sea-ice extent in climate models the result of excessive ice drift?', *Ocean Modelling* **79**, 33–42.

Wang, Q., Danilov, S., Sidorenko, D., Timmermann, R., Wekerle, C., Wang, X., Jung, T. & Schröter, J. (2014), 'The finite element sea ice-ocean model (fesom) v. 1.4: formulation of an ocean general circulation model', *Geoscientific Model Development* **7**(2), 663–693.

Wang, Q., Wekerle, C., Danilov, S., Wang, X. & Jung, T. (2018), 'A 4.5 km resolution arctic ocean simulation with the global multi-resolution model fesom1. 4', *Geosci. Model Dev.* **11**, 1229–1255.

Wang, Z. & Meredith, M. (2008), 'Density-driven southern hemisphere subpolar gyres in coupled climate models', *Geophysical Research Letters* **35**(14).

Wekerle, C., McPherson, R., von Appen, W.-J., Wang, Q., Timmermann, R., Scholz, P., Danilov, S., Shu, Q. & Kanzow, T. (2024), 'Atlantic water warming increases melt below northeast greenland's last floating ice tongue', *Nature Communications* **15**(1), 1336.

Wekerle, C., Wang, Q., Danilov, S., Jung, T. & Schröter, J. (2013), 'Freshwater transport through the canadian arctic archipelago in a multi-resolution global model: model assessment and the driving mechanism of interannual variability', *J. Geophys. Res.-Oceans* **118**, 4525–4541.

Wunsch, C. (2006), *Discrete inverse and state estimation problems: with geophysical fluid applications*, Cambridge University Press.

Zampieri, L., Kauker, F., Fröhle, J., Sumata, H., Hunke, E. C. & Goessling, H. F. (2021), 'Impact of sea-ice model complexity on the performance of an unstructured-mesh sea-ice/ocean model under different atmospheric forcings', *Journal of Advances in Modeling Earth Systems* **13**(5), e2020MS002438.

Zeising, O., Steinhage, D., Nicholls, K. W., Corr, H. F., Stewart, C. L. & Humbert, A. (2021), 'Basal melt of the southern filchner ice shelf, antarctica', *The Cryosphere Discussions* pp. 1–19.

Zentek, R. & Heinemann, G. (2020), 'Verification of the regional atmospheric model cclm v5. 0 with conventional data and lidar measurements in antarctica', *Geoscientific Model Development* **13**(4), 1809–1825.

Zhou, S., Meijers, A. J., Meredith, M. P., Abrahamsen, E. P., Holland, P. R., Silvano, A., Sallée, J.-B. & Østerhus, S. (2023), 'Slowdown of antarctic bottom water export driven by climatic wind and sea-ice changes', *Nature Climate Change* pp. 1–9.